UNIVERSITY OF CALIFORNIA

Santa Barbara

Integrated Optical Delay Line Circuits

on a Ultra-low Loss Planar Waveguide Platform

A dissertation submitted in partial satisfaction

of the requirements for the degree

Doctor of Philosophy

in

Electrical and Computer Engineering

by

Renan L. Moreira

Committee in charge:

Professor Daniel J. Blumenthal, Chair
Professor John E. Bowers
Professor Nadir Dagli
Dr. Jonathon S. Barton

December 2016

The dissertation of Renan L. Moreira is approved.

_____

Professor John E. Bowers

_____

Professor Nadir Dagli

_____

Dr. Jonathon S. Barton

_____

Professor Daniel J. Blumenthal, Committee Chair

September 2016

Integrated Optical Delay Line Circuits on a Ultra-low Loss Planar Waveguide Platform

To Julie, Isla & Isaac Moreira

VITA OF RENAN L. MOREIRA
September 2016

PERSONAL

Full Name: Renan Lemos Moreira
Date of Birth: March 15, 1984
Place of Birth: Belem, Para, Brazil
Email: renan.moreira@gmail.com

EDUCATION

Doctor of Philosophy in Electrical and Computer Engineering, University of California, Santa Barbara, December 2016 (expected)

Master of Science in Electrical and Computer Engineering, University of California, Santa Barbara, June 2011

Bachelor of Science in Electrical and Computer Engineering, University of Texas, San Antonio, December 2008

PROFESSIONAL ACTIVITIES

Vice-president IEEE Photonics Society UCSB Student Branch Chapter,
June 2013 – June 2014

Founding Secretary, IEEE Photonics Society UCSB Student Branch Chapter,
August 2012 – June 2013

Teaching Assistant, Department of Electrical and Computer Engineering, University of California, Santa Barbara – 2009-2010

PUBLICATIONS

D. John, J. Bauters, J. Nedy, W. Li, R. Moreira, J. Bowers, D. J. Blumenthal, and J. Barton, "Fabrication and Demonstration of a Pure Silica-Core Waveguide Utilizing a Density-Based Index Contrast," in Optical Fiber Communication Conference/National Fiber Optic Engineers Conference 2011, OSA Technical Digest (CD) (Optical Society of America, 2011), paper OWS3.

D. D. John, R. Moreira, J. S. Barton, J. F. Bauters, M. J. R. Heck, J. E. Bowers, and D. J. Blumenthal, "Demonstration of Etch-less Core Definition Process for Low-Loss Glass Waveguide Fabrication," European Conference on Integrated Optics, April 2012

D. D. John, Martijn JR Heck, Jared F Bauters, Renan Moreira, Jonathon S Barton, John E Bowers, Daniel J Blumenthal, "Multilayer Platform for Ultra-Low-Loss Waveguide Applications," in *IEEE Photonics Technology Letters*, vol. 24, no. 11, pp. 876-878, June1, 2012.

R. L. Moreira *et al*., "Integrated Ultra-Low-Loss 4-Bit Tunable Delay for Broadband Phased Array Antenna Applications," in *IEEE Photonics Technology Letters*, vol. 25, no. 12, pp. 1165-1168, June15, 2013.

Michael Belt, Jock Bovington, Renan Moreira, Jared F. Bauters, Martijn J. R. Heck, Jonathon S. Barton, John E. Bowers, and Daniel J. Blumenthal, "Sidewall gratings in ultra-low-loss Si3N4 planar waveguides," Opt. Express 21, 1181-1188 (2013)

R. Moreira, J. Barton, M. Belt, T. Huffman, and D. Blumenthal, "Optical Interconnect for 3D Integration of Ultra-Low Loss Planar Lightwave Circuits," in Advanced Photonics 2013, H. Chang, V. Tolstikhin, T. Krauss, and M. Watts, eds., OSA Technical Digest (online) (Optical Society of America, 2013), paper IT2A.4.

D. T. Spencer, M. Heck, R. Moreira, J. T. Bovington, J. E. Bowers, A. Leinse, H. H. v. d. Vlekkert, R. G. Heideman, M. Hoekman, and T. T. Veenstra, "Integrated single and multi-layer Si3N4 platform for ultra-low loss propagation and small bending radii," in Optical Fiber Communication Conference, OSA Technical Digest (online) (Optical Society of America, 2014), paper Th1A.2.

Sudharsanan Srinivasan, Renan Moreira, Daniel Blumenthal, and John E. Bowers, "Design of integrated hybrid silicon waveguide optical gyroscope," Opt. Express 22, 24988-24993 (2014)

R. Moreira, S. Gundavarapu, and D. J. Blumenthal, "Compact Programmable Monolithically Integrated 10-Stage Multi-Channel WDM Dispersion Equalizer on Low-Loss Silicon Nitride Planar Waveguide Platform," in Optical Fiber Communication Conference, OSA Technical Digest (online) (Optical Society of America, 2015), paper Th1F.4.

S. Gundavarapu, T. Huffman, M. Belt, R. Moreira, J. Bowers, and D. Blumenthal, "Integrated Ultra-Low-Loss Silicon Nitride Waveguide Coil for Optical Gyroscopes," in Optical Fiber Communication Conference, OSA Technical Digest (online) (Optical Society of America, 2016), paper W4E.5.

Renan Moreira, Sarat Gundavarapu, and Daniel J. Blumenthal, "Programmable eye-opener lattice filter for multi-channel dispersion compensation using an integrated compact low-loss silicon nitride platform," Opt. Express 24, 16732-16742 (2016)

ABSTRACT

Integrated Optical Delay Line Circuits
on a Ultra-low Loss Planar Waveguide Platform

by

Renan L. Moreira

Photonic integrated circuits (PICs) play a major role in the advancement of optical networks. One of the constraints of PICs is the high propagation loss of optical waveguides. As the complexity in PICs increases, so does the power usage and heat generation; therefore, bringing "fiber-like" losses on-chip would not only allow for the improvement of chip performance, but it would also revolutionize delay line technologies allowing longer delay lines to be integrated on chip, otherwise not practically feasible. The design of such waveguides and optical circuits requires a balance of numerous tradeoffs between mode-size, bending radius, and footprint, to name a few. Herein, we present the design and fabrication of optical delay line circuits using an ultra-low loss waveguide platform, which utilizes a high aspect ratio buried Si_3N_4 core planar waveguide.

Optical delay line circuits are defined here as any optical circuit that requires the optical signal to be delay by a certain amount of time for its proper functionality. Such devices are used in many applications ranging from medical to sensing and national defense. In this dissertation we present the integration of three optical delay line circuits: Tunable true time delay for broadband phased array antennas application, a programmable dispersion compensation filter, and an optical gyroscope waveguide coil. The design tradeoff, fabrication, and results for each circuit are present and highlighted in detail.

TABLE OF CONTENTS

LIST OF FIGURES

xii

Chapter 1

Introduction

1.1 Photonic Integration

The history of photonic integration can be traced back to the first paper on integrated optics written by Stewart Miller in 1969 [1]. Since then, multiple photonic devices and circuits have been integrated, from the first continuous wave (CW) semiconductor laser in 1970 [2] to optical routers containing over 200 functional elements in 2009 [3]. Photonic integrated circuits (PICs) address important issues in the area of data communications by leveraging integration scale for reduced cost, footprint, power, and increased performance [4]. Although optical communications is one of the primary applications and the main drive of photonic integration, PICs can also be found in other applications such as sensing [5], medicine [6], and national defense [7].

The most widely used integration platforms are shown in Figure 1. Each platform has its own unique strength and weaknesses and as a result can provide various benefits and tradeoffs based on the requirement of the end application. The table in Figure 1 also shows the most common application for each platform. Comparing each platform one-to-one becomes challenging, as many of the platform's properties are dependent on the type of device and optical circuit used independent of the material system. For example, numerous InP-based integration platform with different characteristics have been developed, such as offset quantum well, butt-joint growth, selective area growth, quantum well intermixing.

Therefore, here we make general observations regarding each of the platforms advantages and disadvantages. From the list provided, the lowest integrated waveguide losses were demonstrated on two different types of waveguides, which are the silicon nitride core waveguide and the doped silica core waveguide. The silicon nitride core waveguide is the platform used in this dissertation and is discussed in more depth in the next chapter. The doped silica core waveguides have demonstrated losses of 3 dB/m and 7 dB/m for index contrasts of 0.75% and 2%, respectively. The low index contrast, low phase errors, low polarization dependent loss, and low propagation loss make this platform a good candidate for filtering applications [10, 11], where the low contrast limits this platform to large footprint applications. The next platform is polymer planar lightwave circuits, which have the advantage of low cost fabrication with spin coating techniques and a photosensitive polymer for patterning which requires no etching process. Because polymers have a thermo-optic coefficient an order of magnitude higher than silica, they are often used on VOAs and Modulators [12, 13]. The major disadvantage of such platform is the polymer requirement for low temperature processes making it incompatible with many other fabrication techniques.

Following polymer waveguides are lithium niobate (LiNbO$_3$) waveguides, which have a large linear electro-optic coefficient and therefore are used primarily for high-speed modulators and switches [14]. Unfortunately, since LiNbO$_3$ is a uniaxial crystal it has a very large birefringence and high propagation loss.

Between the last two platforms InP and SOI, InP is the most mature system for integrated photonics device and has the advantage of having a direct bandgap, which allows for efficient emission and absorption of light. For that reason, InP is most often used in the integration of lasers, detectors, and electro absorption modulators [15, 16], but the platform is

high in cost and limited to smaller wafers when compared to Silicon. Lastly, waveguides have also been realized on silicon on insulator (SOI). Unlike InP, silicon is an indirect bandgap semiconductor and therefore has no efficient light emission. Silicon waveguides have the advantage of being low cost material and can potentially be CMOS compatible. Since Si has a large index contrast with respect to a silica cladding, very compact devices can be manufactured.
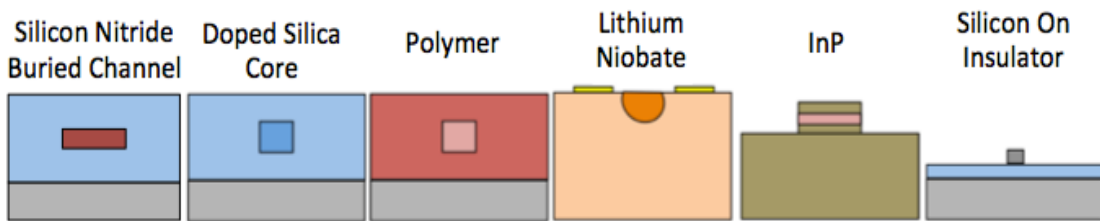
Platform	Advantages	Disadvantages	Application
Silicon Nitride core	• Low propagation loss (1-7 dB/m, <1 dB/m for high aspect ratio) • Low coupling loss (< 1dB with spot size converter	• Bend radius between 1 to 10 mm depending on geometry • No detectors • No electrically pumped gain • Highly birefringent	• Mux/Demux [8] • Filters [9]
Doped Silica core	• Low propagation loss (3-7 dB/m) • Low coupling loss (< 1dB with spot size converter • Low polarization dependence (square core)	• Large footprint (Min. bend radius > 5 mm) • No detectors • No gain • Weak thermo-optic effect	• Mux/Demux [10] • Filters [11]
Polymer	• Low birefringence • Strong thermo-optic • Strong electro-optic effect	• Reliability issues due to polymer • Low index contrast (< 1.5 %) • Not suitable for high temperature process	• Modulators [12] • VOAs [13]
Lithium Niobate	• Strong electro-optic, acousto-optic, and piezo-electric effects	• Birefringent	• Modulators [14]
InP	• Small footprint (high index contrast in 1D) • Efficient laser • Strong electro-optic effect (high-speed)	• Expensive (Scarce material) • Loss > 0.5 dB/cm	• Transmitters [15] • Receivers [16]

| SOI | • Cheap cost (widely available material)
 • Small footprint (high index contrast in 2D)
 • High yield (CMOS compatible) | • No laser (indirect bandgap material)
 • Losses ~ 2dB/cm | • Modulator [17] |

Figure 1. Widely used platforms for photonic integrated circuits (PICs).

This dissertation explores the integration of optical delay line circuits (ODLC) on a high aspect ratio Si_3N_4 waveguide core listed as the first item in Table 2. Although such platform lack integrated active capabilities it has demonstrated world record propagation losses of 0.1 dB/m [24]. This platform is therefore suitable for integrating delay line circuits where low attenuation is required in cascading long delay lines essential in realizing many of the complex processing functions of ODLC. Figure 2 shows an example of such circuit where 4 unique optical delays lines are cascaded to a total of more than 2 meters in propagation length; such circuit is used as true a time delay in optical beamforming and will be studied in detail in Chapter 4.
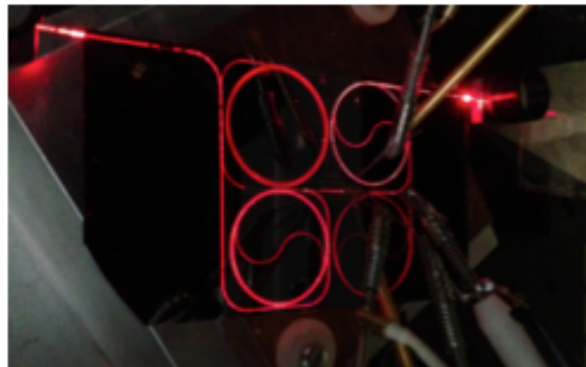
Figure 2: Optical delay line circuit example. True time delay for optical beamforming with total propagation length greater than 2 meters.

Low attenuation alone it is not sufficient when considering an integration platform for optical delay line circuits. If a planar lightwave circuit (PLC) is to be used as part of an overall optical system then the PLC interfacing with fiber and/or other devices must be taken

into account if the processed signal is to be extracted. Optical mode-field mismatch between the fundamental mode of the integrated waveguide and that of the optical fiber can cause a large amount of loss. Device coupling loss becomes of great importance as the refractive-index contrast (Δ) of the integration platform increases. Index contrast can be calculated based on the refractive index of the core (n_{core}) and the refractive index of the cladding (n_{clad}) as following:

$$\Delta = \frac{n_{core}{}^2 - n_{clad}{}^2}{2n_{core}{}^2}$$

Waveguide optical confinement is therefore is directly related to the index contrast. The lower the index contrast, the easier it is to match the optical mode between the waveguide and the optical fiber due to the weakly confinement. However, decreasing index contrast increases the minimum bend radius and thus the overall device footprint. As a result, three parameters must be investigated before selecting the proper platform: coupling loss, bend radius, and attenuation. Table 1 summarizes all 6 major integration platforms with respect to three just mentioned parameters. Index contrast is also included as a comparison metric. It is important to note that the table is not meant to compare state-of-the-art devices but instead the list attempts to provide overall average values for all the platforms. The coupling losses for platforms such as InP and silicon have been demonstrated to reach values around 2 dB/facet through the use of various spot size converters (SSC). It is crucial to mention that such losses come at the cost of complex fabrication and such approach must be evaluated when selecting the proper platform. Overall, the silicon nitride planar lightwave circuit platform provides an ultra-low loss propagation loss with coupling losses < 1 dB with bend losses around 1 mm; and therefore, outweighs all the other platforms when comparing in regards to the integration of optical delay line circuits.

Platform	Si$_3$N$_4$	Doped silica	Polymer	LiNbO$_3$	InP	Silicon
Index contrast (%)	23	0.7	0.7	1	10	40
Coupling Loss (dB)	<1	<1	<1	<1	2 (complex SSC)	2 (complex SSC)
Bend loss (mm)	1	7	7	0.2	0.1	0.02
Attenuation (dB/cm)	0.001	0.05	0.05	0.2	2.5	2

Table 1. Index contrast, coupling loss, bend loss, and attenuation for all 6 major integration platforms.

Analogous to electronic integration, photonic integration provides many advantages over bulk component based systems, by reducing size, cost, and power consumption, while increasing manufacturability and reliability. However, there are other areas where photonic integration has historically not been able to replace bulk optical component realizations, including optical isolation, polarization splitting, and low propagation losses.

Many photonic applications benefit greatly from the ability to achieve fiber-like losses on an integrated platform, in particular, systems that require optical delay lines. Delaying an optical signal is a valuable function for many applications including optical buffering [18], packet synchronization [19], optical beamforming [20], microwave signal processing [21], optical coherence tomography [22], and optical gyroscopes [23]. One of the simplest ways to realize a time delay on a non-integrated system is to propagate light through a physical distance, typically done via a fiber coil. To achieve such functionality (optical delays) on an integrated device becomes challenging, because propagation losses and bend losses on most platforms limit the total length and footprint of integrated "fiber" coils. Low propagation loss is required to achieve long delay lengths without significant signal attenuation, while a small bend radius allows for small overall footprints. Without proper

optimization of the integration platform for waveguide loss and bend radius, the integration of optical delay line circuits becomes impractical. A sacrifice of propagation loss or footprint can degrade the system performance in such a way that most benefits from photonics integration (stability, power consumption, and cost) become outweighed.

The primary focus of this dissertation is on the integration of state-of-the-art optical delay line circuits on a novel ultra low-loss waveguide (ULLW) platform developed at UCSB, capable of achieving record low propagation loss at a variety of bend radii [24]. Figure 3 below shows a plot of waveguide propagation loss versus bend radius for several integration platforms. The red filled diamonds represent all of the designs established at UCSB; these designs push the state-of-the-art boundary as shown in the figure. This ultra low-loss waveguide (ULLW) platform allows for long delay lines to be integrated with low insertion loss at smaller footprint when compared to other integration platforms. The required amount of propagation loss and minimum bend radius for optical delay line circuits are application dependent and will be discussed in the next section.
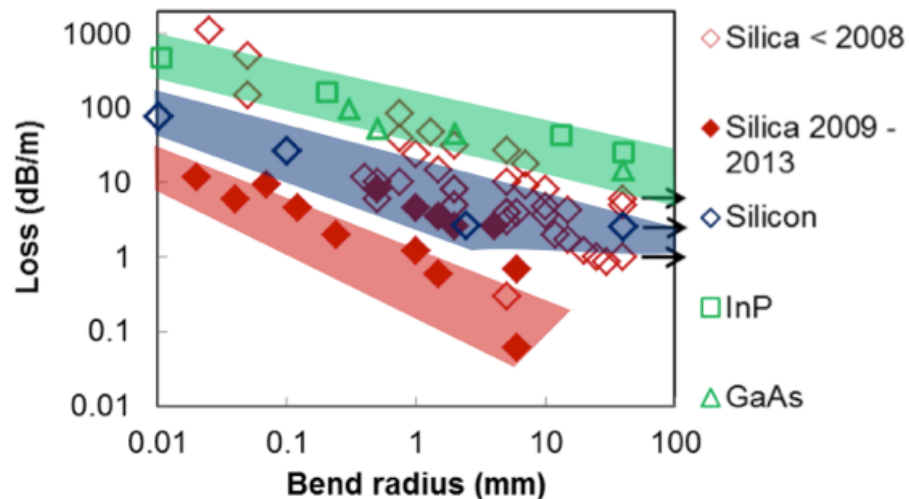
Figure 3. Planar waveguide propagation losses from literature as a function of bend radius. Filled red diamonds represent the waveguide losses from UCSB designs. This figure is taken from [25].

1.2 Optical Delay Line Circuits

Many implementations of tunable optical delay lines exist for various applications regardless of the integration platform. Some of the most common delay methods are often based on ring resonators [26], Bragg grating [27], and photonic crystals [28], but all of these schemes have their own disadvantages. A high finesse ring resonator cavity can achieve high amounts of group delay at its resonance at the cost of narrower bandwidth [29] and also pulse distortion when operating on the edge of the filter function due to the high group velocity dispersion (GVD). Grating based tunable delay lines use a chirped grating to create a time delay and a tunable laser source to tune the delay length [30]. The laser requirement for this approach makes this scheme costly if a large number of delay elements are required. Lastly, photonic crystals use the slow light effect to create an optical delay [31] but have high propagation loss as a major drawback. The loss in photonic crystal waveguides has shown to be proportional to the square of the group index [32]. Thus the simplest method of creating an optical delay line, as previously stated, is through the propagation of the signal via a waveguide of finite length to generate the required time delay. The amount of delay of this approach is only limited by the platform's propagation loss and bend radius, and as a result the ULLW platform plays a major role on the integration of such devices. Therefore, optical delay line circuits (ODLCs) defined in this dissertation use finite waveguide propagation to create delay lines, in contrast to the previously mentioned approaches.

This work builds upon previously established building blocks on the ULLW platform by demonstrating the integration of complex planar lightwave circuits not practically achievable on any other platform, in particular the integration of optical delay line circuits.

Three optical delay line circuits with very different design constraints were chosen to show the proper platform design while achieving record device performance for each application as a direct consequence of the ULLW platform. These three applications are summarized below with each constraint described in Table 2.

Applications	I. Variable true time delay for phased array antennas	II. Programmable dispersion compensating filter	III. Optical gyroscope
Delay line length ranges	1-2 meters	10-30 cm	3-5 meters
Waveguide loss	~ 1 dB/m	5-10 dB/m	< 1 dB/m
Footprint	Not critical (10-50 cm^2)	< 5 cm^2	~ 5 cm^2

Table 2. Optical delay line circuits presented in this dissertation with each constraint for length and footprint listed

The first application of a true time delay, for broadband phased array antennas, was chosen to highlight the platform's ultra-low loss by demonstrating a tunable delay length greater than 2 meters, see Figure 2 above for reference. The second application is a dispersion-compensating filter, which was chosen to demonstrate the platform's ability to provide low loss at small footprints over prior state of the art devices. Table 4 compares current state-of-the-art dispersion compensating filter with the device presented in this dissertation highlighted in green. As can be seen from the table the UCSB device outperforms state of the art with respect to footprint with no major degradation to device performance.

Stage #	type	dispersion	bandwidth	size	FSR	loss	total loss	
25	lattice	300 ps/nm	60 GHz	17.5 cm²	200 GHz	4.8 dB	7 dB	Furukawa 2009
16	parallel	97 ps/nm	0.6 nm	16.32 cm²	100 GHz	x	17 dB	Furukawa 2009
8	lattice	500 ps/nm	40 GHz	8.06 cm²	100 GHz		6.6 dB	NTT 2008
10	lattice: dispersion optimized	-570 to 520 ps/nm	15 GHz	2.25 cm²	100 GHz	0.7 dB	15 dB	UCSB 2015

Table 3. State-of-the-art integrated dispersion compensating filters.

The third application utilizes a new low loss 3D architecture to address both, ultra low loss and compact footprint to an integrated fiber coil for optical gyro applications, which is a major contribution of this thesis. Figure 4 shows an example of a fabricated 3-meter coil with losses of 3 dB/m with a footprint smaller than a quarter.
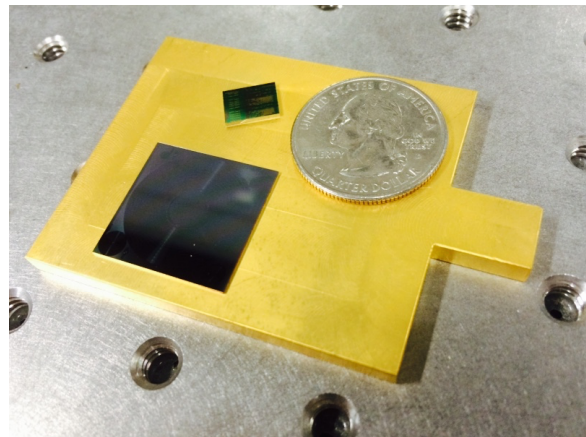
Figure 4. Fabricated 3-meter waveguide coal together with a silicon photonics optical gyro frontend.

The subsequent chapters introduce each application in more detail, provide the appropriate design, describe the fabrication procedures, and present the measured performance of each fabricated device.

1.3 Thesis Outline

In chapter 1, the advantages of photonic integration are presented together with multiple integration platforms. The ultra low loss waveguide (ULLW) platform is briefly mentioned and three different optical delay line applications are identified for the purpose of integration.

Chapter 2 describes the ULLW platform and its fabrication procedures together with the process optimization required to achieve the ultra low loss characteristics. Chapter 3 describes all of the fundamental building blocks required to fabricate and design the planar lightwave circuits described herein. In Chapter 4, the optical true time delay circuit for application on broadband phased array antennas is introduced together with some design requirements to highlight the waveguide's ultra low propagation loss. Two generations of device design and fabrication will be presented with test results shown for both. Chapter 5 proceeds to apply the platform for the integration of an all-optical dispersion compensation filter that was chosen in order to highlight the platform's ability to provide low loss with a compact footprint when compared to other platforms. Chapter 6 introduces the third and final application of this thesis, which is an integrated optical gyroscope. The optical gyroscope model is first presented and the gyroscope coil designed accordingly. The chapter shows results of a potential integrated optical gyroscope coil and uses simulations to estimate its gyro performance. Chapter 7 continues with the same application of integrated optical gyroscope but introduces a low loss vertical coupler. The vertical coupler allows for multi-layer integration as a way of mitigating the platforms loss vs. footprint tradeoff. Finally, a summary and conclusion are provided in Chapter 8 together with the future direction of this research.

1.4 References

[1]   S. E. Miller, " Integrated Optics: An Introduction," The Bell systems technical journal, vol. 48, No. 7. September 1969.

[2]   Hayashi, I. and Panish, M. B. and Foy, P. W. and Sumski, S., "Junction lasers which operate continuously at room temperature," Applied Physics Letters, 17, 109-111 (1970).

[3]   S. C. Nicholes, M. L. Mašanović, B. Jevremović, E. Lively, L. A. Coldren, and D. J. Blumenthal, "The World's First InP 8x8 Monolithic Tunable Optical Router (MOTOR) Operating at 40 Gbps Line Rate per Port," in Optical Fiber Communication Conference and National Fiber Optic Engineers Conference, OSA Technical Digest (CD) (Optical Society of America, 2009), paper PDPB1.

[4]   Heck, M.J.R.; Bauters, J.F.; Davenport, M.L.; Doylend, J.K.; Jain, S.; Kurczveil, G.; Srinivasan, S.; Yongbo Tang; Bowers, J.E., "Hybrid Silicon Photonic Integrated Circuit Technology," in Selected Topics in Quantum Electronics, IEEE Journal of , vol.19, no.4, pp.6100117-6100117, July-Aug. 2013

[5]   Pozo, J.; Harmsma, P.; Lo Cascio, D.M.R., "Application specific photonic integrated circuits and the sensing industry," in Transparent Optical Networks (ICTON), 2013 15th International Conference on , vol., no., pp.1-1, 23-27 June 2013

[6]   Günay Yurtsever, Boris Považay, Aneesh Alex, Behrooz Zabihian, Wolfgang Drexler, and Roel Baets, "Photonic integrated Mach-Zehnder interferometer with an on-chip reference arm for optical coherence tomography," Biomed. Opt. Express 5, 1050-1061 (2014)

[7]   C. Roeloffzen, R. Oldenbeuving, R. B. Timens, P. van Dijk, C. Taddei, A. Leinse, M. Hoekman, R. G. Heideman, L. Zhuang, D. Marpaung, and M. Burla, "Integrated Optical Beamformers," in Optical Fiber Communication Conference, OSA Technical Digest (online) (Optical Society of America, 2015), paper Tu3F.4.

[8]   Daoxin Dai, Zhi Wang, Jared F. Bauters, M.-C. Tien, Martijn J. R. Heck, Daniel J. Blumenthal, and John E Bowers, "Low-loss Si3N4 arrayed-waveguide grating (de)multiplexer using nano-core optical waveguides," Opt. Express 19, 14130-14136 (2011)

[9]   Ming-Chun Tien, Jared F. Bauters, Martijn J. R. Heck, Daryl T. Spencer, Daniel J. Blumenthal, and John E. Bowers, "Ultra-high quality factor planar Si3N4 ring resonators on Si substrates," Opt. Express 19, 13551-13556 (2011)

[10]   Tomohiro Shibata, Shin Kamei, Tsutomu Kitoh, Takuya Tanaka, and Masaki Kohtoku, "Compact and low insertion loss (~1.0 dB) Mach-Zehnder interferometer-

synchronized arrayed-waveguide grating multiplexer with flat-top frequency response," Opt. Express 16, 16546-16551 (2008)

[11] Takafumi Chiba, Hideaki Arai, Hideki Nounen, Katsumi Ohira, "Waveguide interleaving filters," Proc. SPIE 5246, Active and Passive Optical Components for WDM Communications III, 532 (August 19, 2003).

[12] Datong Chen, Harold Fetterman, Antao Chen, William Steier, Larry Dalton, Wenshen Wang, and Yonggiang Shi, "Demonstration of 110 GHz electro-optic polymer modulators," Applied Physics Letters, 70, 3335-3337 (1997).

[13] Y. T. Han et al., "10 channel polymer variable optical attenuator array for power monitoring and equalization in integrated PLC ROADM module," 2008 International Conference on Photonics in Switching, Sapporo, 2008, pp. 1-2.

[14] E. L. Wooten et al., "A review of lithium niobate modulators for fiber-optic communications systems," in IEEE Journal of Selected Topics in Quantum Electronics, vol. 6, no. 1, pp. 69-82, Jan.-Feb. 2000.

[15] Y. A. Akulova, G. A. Fish, P. C. Koh, C. Schow, P. Kozodoy, A. Dahl, S. Nakagawa, M. Larson, M. Mack, T. Strand, C. Coldren, E. Hegblom, S. Penniman, T. Wipiejewski, and L. A. Coldren, "Widely-Tunable Electroabsorption-Modulated Sampled Grating DBR Laser Transmitter", IEEE Journal on Selected Topics in Quantum Electronics.8, pp. 1349-1357, 2002.

[16] K. N. Nguyen, J. M. Garcia, E. Lively, H. N. Poulsen, D. M. Baney and D. J. Blumenthal, "Monolithically integrated dual-quadrature coherent receiver on InP with 30 nm tunable SG-DBR local oscillator," 2011 37th European Conference and Exhibition on Optical Communication, Geneva, 2011, pp. 1-3.

[17] G. T. Reed, G. Mashanovich, F. Y. Gardes, and D. J. Thomson, "Silicon optical modulators," Nature Photonics 4, 518-526 (2010).

[18] E. F. Burmeister, D. J. Blumenthal, J. E. Bowers, "A comparison of optical buffering technologies," Optical Switching and Networking, Vol. 5, Issue 1, pp 10-18. March 2008.

[19] J. P. Mack, K. N. Nguyen, J. M. Garcia, E. F. Burmeister, M. M. Dummer, H. N. Poulsen, B. Stamenic, G. Kurczveil, K. Hollar, L. A. Coldren, J. E. Bowers, and D. J. Blumenthal, "Asynchronous 2x2 Optical Packet Synchronization, Buffering, and Forwarding," in Optical Fiber Communication Conference, OSA Technical Digest (CD) (Optical Society of America, 2010), paper OThN1.

[20] J. L. Corral, J. Marti, J. M. Fuster and R. I. Laming, "True time-delay scheme for feeding optically controlled phased-array antennas using chirped-fiber gratings," in IEEE Photonics Technology Letters, vol. 9, no. 11, pp. 1529-1531, Nov. 1997.

[21] José Capmany, Beatriz Ortega, and Daniel Pastor, "A Tutorial on Microwave Photonic Filters," J. Lightwave Technol. 24, 201- (2006).

[22] EunSeo Choi, Jihoon Na, Seon Young Ryu, Gopinath Mudhana, and Byeong Ha Lee, "All-fiber variable optical delay line for applications in optical coherence tomography: feasibility study for a novel delay line," Opt. Express 13, 1334-1345 (2005).

[23] Ciminelli, C., Dell'Olio, F., Campanella, C. & Armenise, M. Photonic technologies for angular velocity sensing. Adv. Opt. Photon. 2, 370–404 (2010).

[24] Jared F. Bauters, Martijn J. R. Heck, Demis John, Daoxin Dai, Ming-Chun Tien, Jonathon S. Barton, Arne Leinse, René G. Heideman, Daniel J. Blumenthal, and John E. Bowers, "Ultra-low-loss high-aspect-ratio Si3N4 waveguides," Opt. Express 19, 3163-3174 (2011).

[25] Heck, M, Bauters, J, Davenport, M, Spencer, D and Bowers, J, "Ultra- low loss waveguide platform and its integration with silicon photonics." Laser & Photonics Reviews (2013).

[26] Fengnian Xia, Lidija Sekaric, and Yurii Vlasov, "Ultracompact optical butters on a silicon chip," Nature Photonics 1, 65-71 (2007)

[27] B. Ortega, J. L. Cruz, J. Capmany, M. V. Andres and D. Pastor, "Variable delay line for phased-array antenna based on a chirped fiber grating," in IEEE Transactions on Microwave Theory and Techniques, vol. 48, no. 8, pp. 1352-1360, Aug 2000.

[28] Y. Jiang, W. Jiang, X. Chen, L. Gu, B. Howley, and R. T. Chen, "Nanophotonic crystal waveguides for ultra-compact tunable time delay lines," Proc. of SPIE, vol. 5733, pp. 166-175, 2005.

[29] G. Lenz, B. J. Eggleton, C. K. Madsen and R. E. Slusher, "Optical delay lines based on optical filters," in IEEE Journal of Quantum Electronics, vol. 37, no. 4, pp. 525-532, Apr 2001.

[30] A. Molony, Lin Zhang, J. A. R. Williams, I. Bennion, C. Edge and Fells, "Fiber Bragg-grating true time-delay systems: discrete-grating array 3-b delay lines and chirped 6-b delay lines," in IEEE transactions on Microwave Theory and Techniques, vol. 45, no. 8, pp. 1527-1530, Aug 1997.

[31] S. Combrie, J. Bourderionnet, P. Colman, D. Dolfi and A. De Rossi, "90ps tunable true-time delay line based on photonic crystals," Lasers and Electro-Optics (CLEO) and Quantum Electronics and Laser Science Conference (QELS), 2010 conference on, San Jose, CA, USA 2010, pp. 1-2.

[32]   S. Hughes, L. Ramunno, J. F. Young, and J. E. Sipe, "Extrinsic optical scattering loss in photonics crystal waveguides: role of fabrication disorder and photon group velocity," Phys. Rev. Lett., vol. 94, no. 3, pp.033903-1 – 033903-4, Jan. 2005.

Chapter 2

Ultra-Low Loss Waveguide (ULLW)

Platform

2.1 Introduction

Successful planar lightwave circuit design and fabrication depend largely on the materials and fabrication processes used. For example, for proper device functionality the material's index of refraction and thicknesses must be accurately controlled. Processes such as etching and deposition must be optimized to minimize roughness and material absorption. Therefore, careful material and fabrication method selection is mandatory. This chapter will focus solely on the design, fabrication, and procedure optimization of the ultra-low loss waveguide (ULLW) platform.

The ULLW platform used in this work was first demonstrated by Jared Bauters and et al. [1] and showed world record waveguide losses of < 0.1 dB/m with coupling losses of 0.91 dB/facet [2]. The main contribution of the new platform was the achievement of waveguide propagation losses closer to fiber-like losses on chip. This novel design makes the integration of delay line circuits now feasible at a low insertion loss cost. The ultra low loss was achieved through intensive material and waveguide geometry optimization studies. This chapter presents the ULLW platform explaining the design tradeoffs and the fabrication procedure.

2.2 Waveguide structure overview

A schematic of the cross-sectional structure of the standard ultra-low loss waveguide is shown in Figure 5. The waveguide consists of a buried silicon nitride core (n = 1.99) and a silicon dioxide cladding (n = 1.45). The index contrast between the waveguide core and the waveguide cladding is one of the fundamental parameters of an integrated optical waveguide. To achieve a high-density of photonic integration, a high-index contrast is mandatory for the tight confinement required for the small bend radii. On the other hand, high-index contrast usually means high propagation loss due to roughness at the waveguide boundaries between the core and the cladding. One of the main sources of losses in an optical waveguide is fabrication-induced roughness at the waveguide sidewalls followed by material absorption [3]. Therefore, in order to achieve a low propagation loss at a tight bend radius, a high index contrast core is required without compromising the loss.
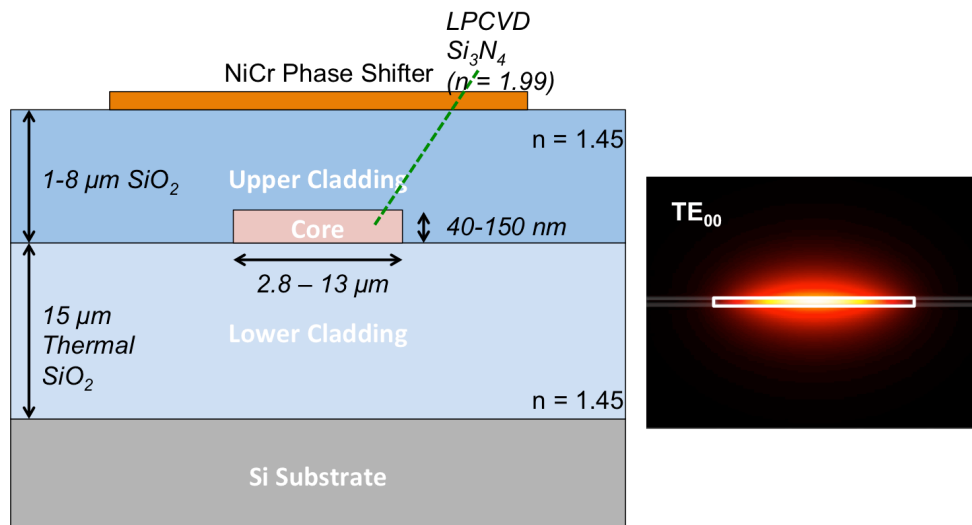
Figure 5. (Left) Schematic of ULLW platform structure. (Right) Electrical field intensity for the fundamental mode for a 2.8 μm x 90 nm waveguide. The waveguide structure is outlined in white showing an optical confinement < 10%.

The ULLW platform achieves record low losses through a geometry driven approach. By incorporating a high-aspect-ratio core geometry, where the waveguide core is much wider

than it is thick, the overlap between the optical mode and the sidewall roughness can be minimized thus improving waveguide loss. Because decreasing the core thickness also decreases the optical confinement, the waveguide core width is increased to increase confinement and allow for a tighter bend radius. Figure 5 (Right) shows the fundamental optical mode for a waveguide geometry of 2.8 μm by 90 nm, where the mode confinement in the core is approximately 10%. This waveguide geometry has a propagation loss of 3 dB/m at a minimum bend radius of 1mm, as it will later be shown.

Through careful optimization of core geometry, an ultra-low loss waveguide can be achieved at a small bend radius. Material selection also plays a major role in the platform performance especially when considering material absorption. Stoichiometric silicon nitride as a waveguide core provides material stability and a high index contrast with SiO_2 cladding required for the tight bend radius. With the proper deposition method of silicon nitride, nanometer thickness accuracy and low surface roughness can be attained. A full description of the platform is found in [4].

Figure 13 shows the effect of the waveguide geometry on the effective indices for a waveguide core thickness of 90nm. The effective indices of TE and TM fundamental modes show a large difference indicating a high birefringence that gives the waveguide polarization maintaining properties. Because of this property of the platform, the ULLWs are meant to operate in TE polarization only. The single-mode condition is also highlighted on the plot, which corresponds to a 3 μm wide waveguide for a 90 nm thick waveguide core. The following sections describe the fabrication procedures and the major contributing loss components of the platform.
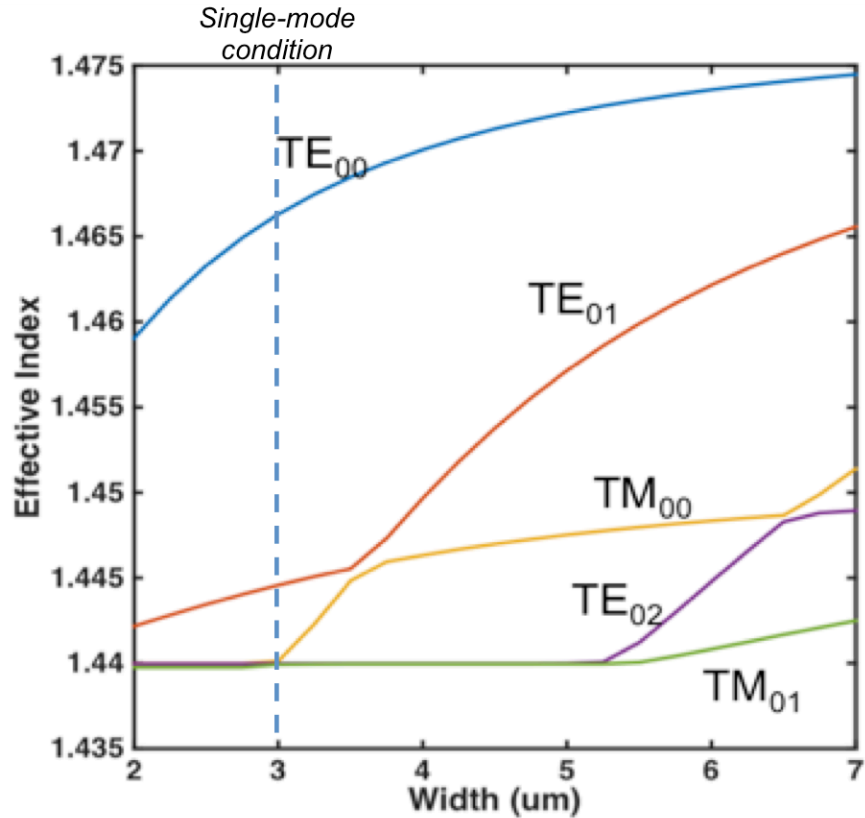
Figure 6. Core width dependence of the effective indices of ULLW for core thickness of 90nm.

2.3 Fabrication

The general steps in fabricating buried channel waveguides on the ULLW platform are described in this section. The fabrication steps are outlined in Figure 7 below. The waveguide fabrication is done on a prime grade <100> P-doped 100 mm Si substrate. The substrate thickness varies between 500 μm and 1 mm depending on the amount of wafer bow acquired due to material stress. A complete discussion of stress during fabrication can be found in the Appendices.

19
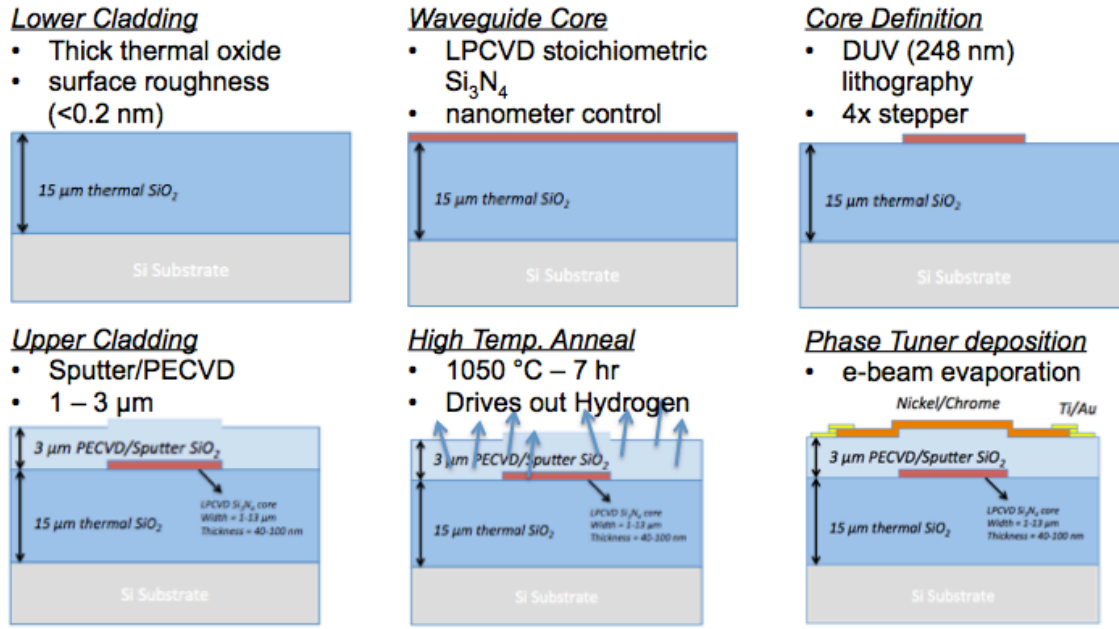
Figure 7. ULLW fabrication summary

The first step in the process is the deposition of the lower cladding. Due to the high aspect ratio of the waveguide design, the optical mode is mostly in the waveguide cladding, where in certain designs less than 10% is confined in the waveguide core. Therefore, the choice of cladding material is of crucial importance. Among all of the various SiO_2 deposition methods, thermal oxidation provides the highest-quality film with the lowest amount of impurities, especially when compared to methods such as PECVD [5]. The silicon dioxide (n = 1.45) lower cladding is then grown via wet thermal oxidation to a thickness of 15 μm. The oxide thickness is chosen to decrease the substrate leakage to a negligible amount, and because of the large weakly confined mode used in this work, lower cladding thicknesses greater than 15 μm are required to reduce the losses to less than 0.01 dB/m [6].

The next step is to deposit and define the silicon nitride waveguide core. The Si_3N_4 (n = 1.99) waveguide core is deposited through low-pressure chemical vapor deposition (LPCVD) with thicknesses varying between 40-150 nm, where the application determines the core thickness based on the loss and bending characteristics required. The main reaction of

20

the deposition method is thermal decomposition at the substrate, and since the deposition is done at a high temperature (800-850 °C) any hydrogen contamination that would be incorporated in the film diffuses out of the waveguide core. The high temperature LPCVD process is able to provide stoichiometric films with nanometer control and high uniformity, all of which are crucial in designing and fabricating low loss waveguides. After deposition, the waveguide core is patterned through 4x deep UV (248 nm) lithography and then defined by a CF_4/O_2 etch on an ICP-RIE etcher.

After etching the wafer is cleaned thoroughly to remove any residual photoresist, and then the upper cladding is deposited. The silicon dioxide upper cladding is deposited via plasma enhanced chemical vapor deposition (PECVD) at a temperature of 300 °C. Unlike the work in [2] where a bonded upper cladding is used to achieve record low loss, the work presented here uses a deposited upper cladding to allow for the deposition of heaters (resistive metals) which will act as phase tuners in most applications. Upper cladding thicknesses vary between 1-6 μm depending on the waveguide geometry/confinement. After the upper cladding deposition, the entire waveguide structure is annealed under a N_2 environment at 1050 °C for 7 hours in order to drive out any hydrogen impurities that act as absorption sites degrading the overall waveguide propagation loss.

The last step of the process is the deposition of a resistive material (NiCr) for heaters, which will function as a tuning mechanism via the thermo-optic effect. The heater deposition step requires two steps: one for the heater itself and the other for the Ti/Au low-resistance electrical contact. In order to control the NiCr composition 8 alternating layers of alternating nickel and chrome were deposited, corresponding to 4 layer of 12.5 nm thick nickel and 6.0 nm of chrome. After the heater is deposited a 950 C anneal is required for alloying. The

heaters is deposited directly above the waveguide and is typically a few microns wider than the waveguide, depending on the waveguide geometry. All the metals were deposited via e-beam evaporation and patterned through liftoff. The wafer is then diced and facets are polished for testing.

2.4 Waveguide loss

This section discusses the primary sources of optical loss on the ULLW platform. When the electric field propagates down the waveguide, photons can be absorbed, scattered, or radiated forming the three fundamental types of losses on an optical waveguide. The following subsections will discuss each source of loss and discuss how each can be mitigated.

2.4.1 Scattering loss

The major contributor of loss to the ULLW platform comes from scattering loss due to surface/sidewall roughness of the waveguide core arising from the deposition and etching. Scattering loss occurs when electromagnetic waves interact with roughness "centers" of a size smaller than the wavelength [7]. Waveguide root-mean square (rms) roughness, also referred to as line edge roughness (LER), is defined as the deviation from the ideal edge as seen from the top-down, as shown in Figure 8. LER describes the sidewall striations of photoresist and the subsequently etched feature.
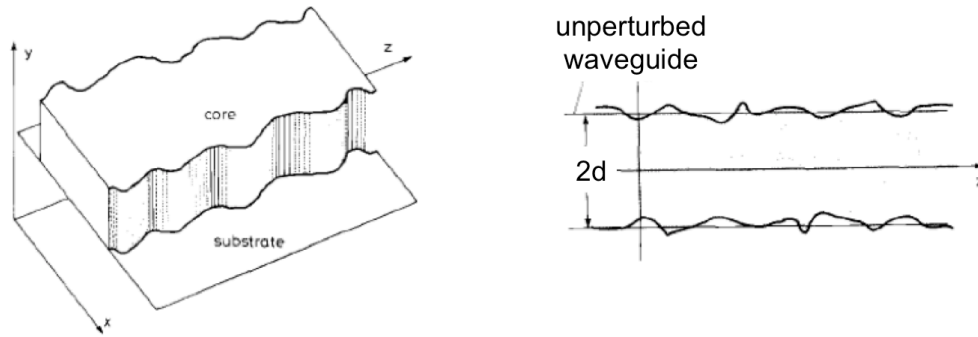
Figure 8. (Left) Demonstration of waveguide sidewall roughness. (Right) Line edge roughness - the standard deviation from the unperturbed waveguide.

Payne and Lacey developed a theoretical upper bound expression on the scattering loss for planar waveguides based on the values of the line edge roughness [8]. The scattering loss (α) for a waveguide with rms roughness (σ), will have an upper bound given by:

$$\alpha \leq \frac{\sigma^2}{k_0 d^4 n_1} \kappa$$

where k_0 is the free-space wave number ($2\pi/\lambda$), n1 is the core effective index, d is the core half-width, and κ is a parameter that depends on the waveguide geometry and roughness statistical distribution (Gaussian, exponential, etc.). For most practical waveguide geometries κ is typically on the order of unity [9]. The equation above then predicts that the best method of reducing waveguide scattering loss is by reducing the waveguide roughness (σ).
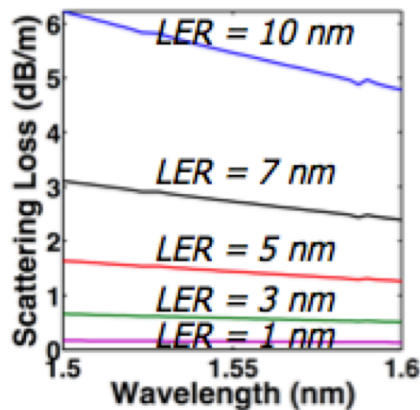
Figure 9. Simulated scattering loss for different waveguide rms roughness for a 2.8 um x 90 nm waveguide geometry.

23

Figure 9 above shows the simulated scattering loss per unit length as function of rms roughness for the waveguide geometry of 2.8 μm x 90 nm. The simulation shows the quadratic dependence of the loss on roughness and predicts that in order to achieve losses below 1 dB/m, a roughness of less than 3 nm is required.

The atomic force microscope (AFM) is used to quantify LER for fabricated waveguides. A top down scan is done over the desired edge of the waveguide as shown in Figure 10 (Left). The LER alone is then extracted from the 2D scan so that the standard deviation from the perfect edge can be found by applying a linear fit through all the measured points of the edge. A typical extraction of rms roughness (σ) from a fabricated waveguide is shown in Figure 10 (Right) corresponding to a measured roughness of 8.3 nm.
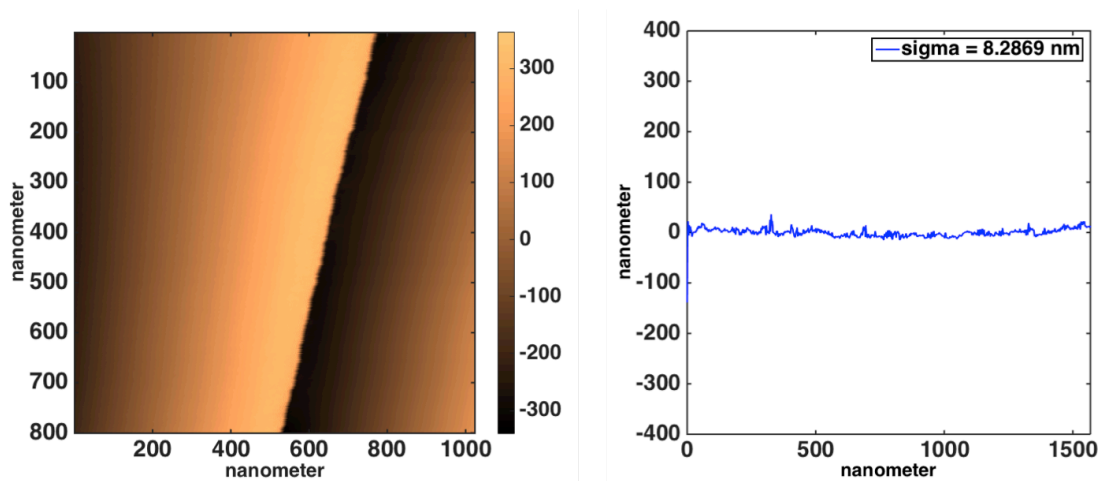
Figure 10. AFM scan of waveguide edge with the LER extracted

Because the scattering loss has a quadratic dependence on roughness, reducing the sidewall roughness becomes the major challenge in reducing scattering loss.

Although plasma etching plays a role in LER, most of the roughness translated to the core originates from the quality of the photoresist mask. Therefore, optimizing lithography and reducing the etch mask roughness becomes the primary method in reducing LER. The

photoresist roughness can be reduced through a resist reflow process (RRP) where the resist is baked above its glass transition temperature causing the resist to flow and smooth the sidewall roughness [10]. Special care must be taken when choosing the appropriate temperature and time for a resist reflow process. If the reflow temperature is too low then no observable improvement will be seen, but if the temperature and time is too high then waveguide deformation can occur which can affect the final shape and performance of the end waveguide. It is important to note that the RRP is photoresist dependent. Figure 11 shows the thermal flow characteristics of several bake temperatures for the UV210 photoresist used in the ULLW process.
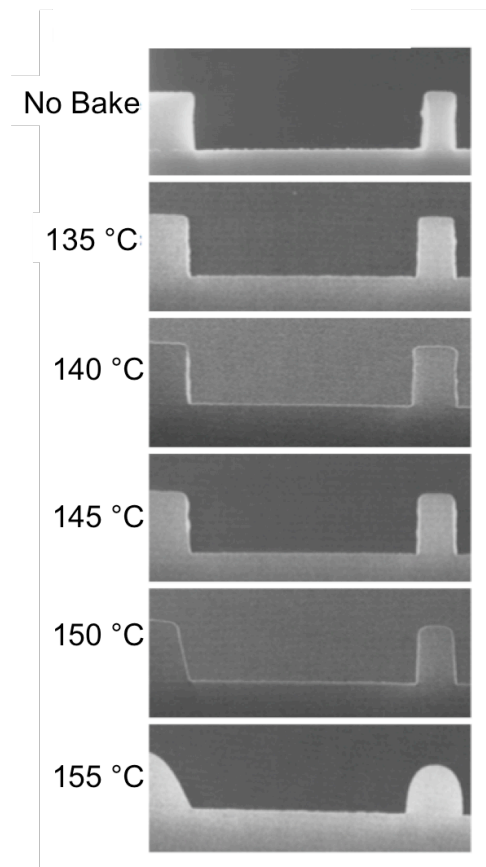
Figure 11. : Thermal flow characteristics of UV210 photoresist used in the ULLW fabrication. Figure extracted from photoresist datasheet [11].

Based on the figure above, four different bake temperatures were chosen to analyze the effects of resist reflow on LER:

- 135 °C

- 145 °C

- 150 °C

- 155 °C

All wafers were baked for 3 minutes on a contact hotplate, and the LER was quantified through the AFM scan approach described above. The effect of the RRP on LER is summarized by the plot in Figure 12. A clear trend in LER reduction can be seen as the temperature is increased. The LER reaches a minimum of approximately 3 nm for a temperature of 150 °C, which then becomes the operating point of the ULLW platform fabrication.
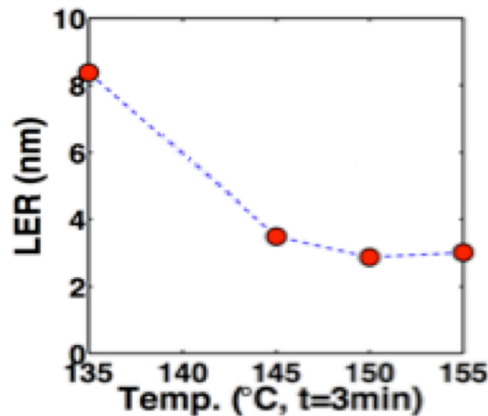
Figure 12. Measured LER reduction due to resist reflow

Apart from reducing the waveguide roughness, the other method of decreasing scattering loss, according to Payne and Lacey's analytical expression, is to increase the waveguide width. The typical measured propagation losses of the waveguides fabricated at the UCSB cleanroom with resist reflow are shown in Figure 13. The figure displays the

measured losses for core thicknesses of 100nm (Left) and 120nm (Right) as a function of waveguide width. As expected from the geometry optimization of the ULLW platform and predicted by Payne and Lacey, as the waveguide becomes wider the waveguide scattering loss decreases substantially. The measurements were done on a 70 nm wavelength range from 1330-1600nm, where the plot only shows the lowest loss wavelength point. The measurements were done via optical frequency domain reflectometry (OFDR) described in Appendix B. Propagation losses < 1dB/m can be achieved for the 100 nm thick core with waveguide width of 5.0 μm. Although such core geometry is multimode and can excite the first higher order TE mode (refer to Figure 6), an adiabatic taper can be used for the excitation of the fundamental mode alone [12].
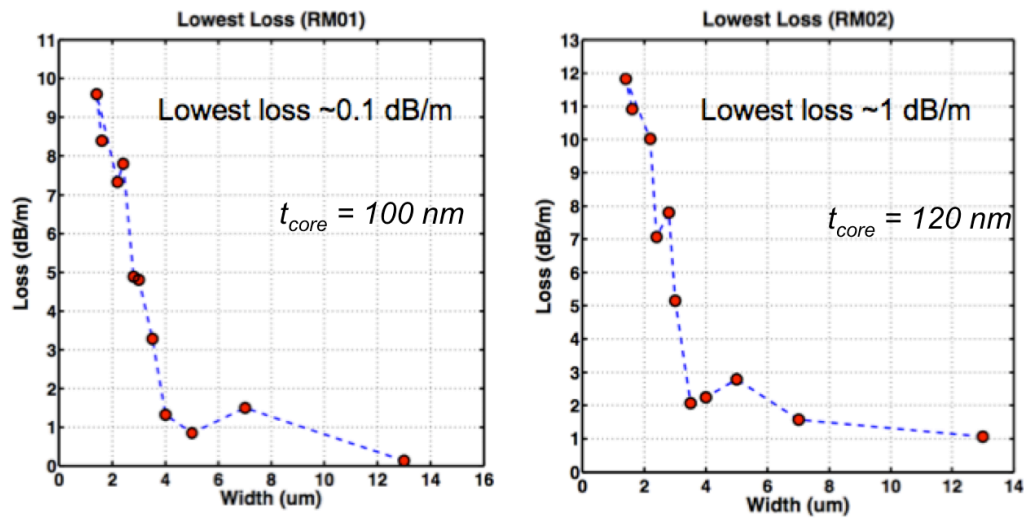
Figure 13. Measured propagation loss as a function of waveguide width for (Left) 100 nm and (Right) 120 nm thick core.

2.4.2 Absorption loss

According to [3] after scattering loss is considered, the second limiting factor of waveguide loss is the material absorption. This type of loss is due primarily to the molecular vibration caused from impurities incorporated into the waveguide material. Of particular

27

interest are the overtone absorptions caused by hydrogen impurities, which have strong absorption lines around 1550 nm. Si-H and N-H for example have absorption lines centered at 1480nm and 1510nm, respectively. Although the peaks are not centered at the operating wavelength of 1550nm, the tail of the absorption leads to losses in the region of interest. Figure 14 shows the measured waveguide losses for two identical waveguide cores with different upper cladding. The tail from the N-H absorption is visible in both cases corresponding to higher losses closer to 1510 nm.
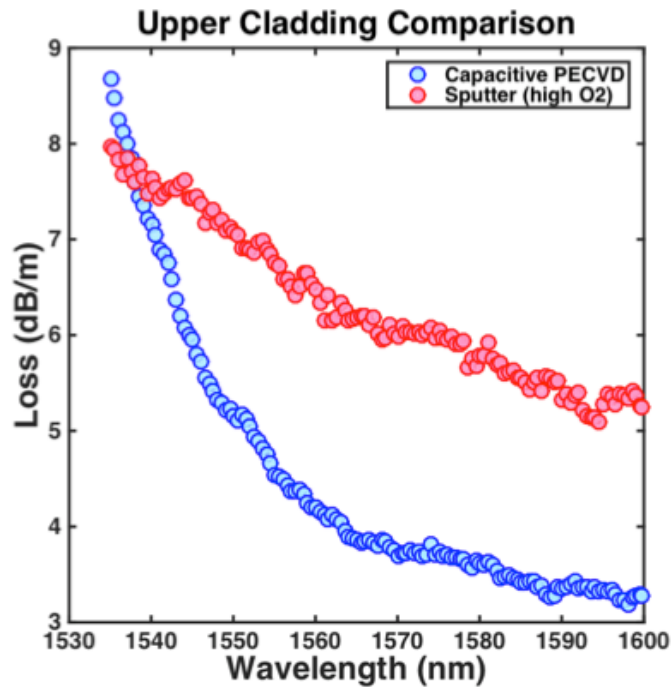
Figure 14. Measured wavelength dependent loss for PECVD and Sputter upper cladding.

Because hydrogen is incorporated into the waveguide material through the precursors used during the deposition, the absorption loss is deposition method dependent. The figure above compares two identical waveguides where only the upper cladding deposition varies. The red curve corresponds to a sputtering deposition method, while the blue curve was deposited via PECVD. Since sputtering is a physical vapor deposition (PVD), no precursor containing

hydrogen is used and therefore shows a lower wavelength dependent loss than PECVD. Unlike sputtering, PECVD utilizes Silane (SiH_4) as a precursor, which incorporates hydrogen into the film and therefore shows a higher loss variance across the measured wavelengths [13, 14].

Hydrogen bonds can be eliminated and the hydrogen diffused out of the material by annealing the films at a high temperature typically around 1100 °C [15,16]. Figure 15 shows the measured waveguide loss before and after anneal (1050 °C for 7 hours) for both types of waveguide cladding, sputter and PECVD. For both cases, the high temperature anneal reduced the propagation loss. The PECVD upper cladding had greater loss reduction with a high temperature anneal due to its higher hydrogen content before anneal.
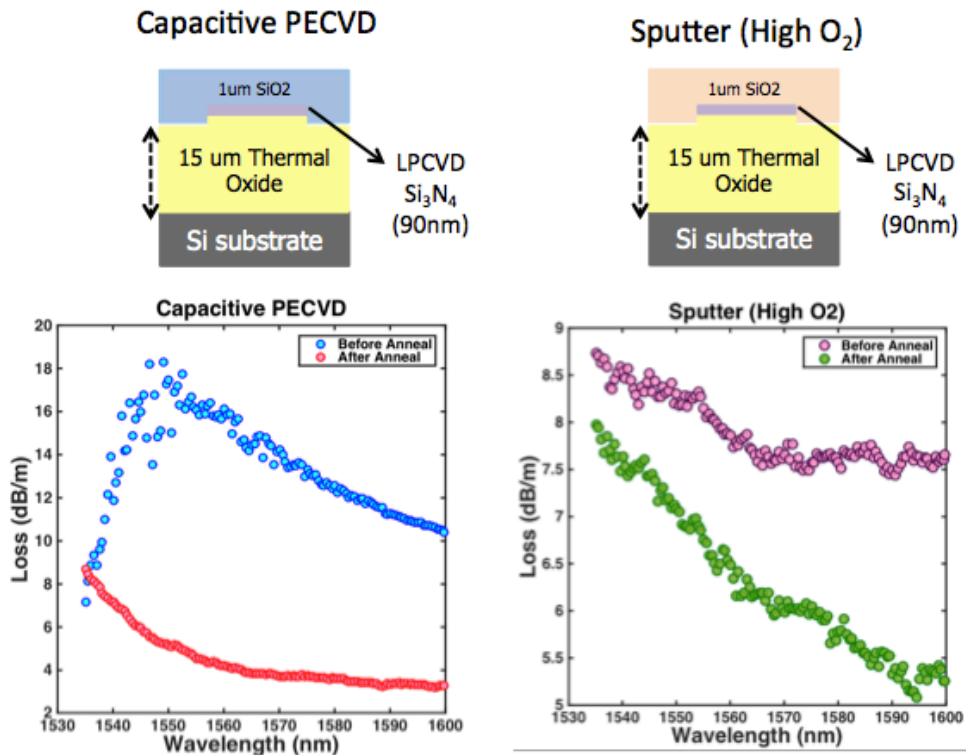
Figure 15. The effect of high temperature anneal (1050 C, 7 hrs) on waveguide propagation loss.

2.4.3 Bend Loss

The bending capabilities of a waveguide platform are of crucial importance for integrated optical circuits. A key metric for photonic integration of planar lightwave circuits, apart from propagation loss, is the footprint. Therefore the bend radius and bend loss associated with it are the limiting factor in footprint performance. Figure 16 (Left) shows the schematic of a fundamental mode of a waveguide propagating in a circular bend of radius R. The dashed lines on the plot indicate the constant phase plane, and if the phase front is to remain linear, the tangential speed must increase as the radial distance is increased (indicated by the arrow sizes in the plot). Therefore, as R increases the tangential speed approaches the speed of light, and as a result the tail of the mode must "leak" away from the guided mode resulting in bend loss.
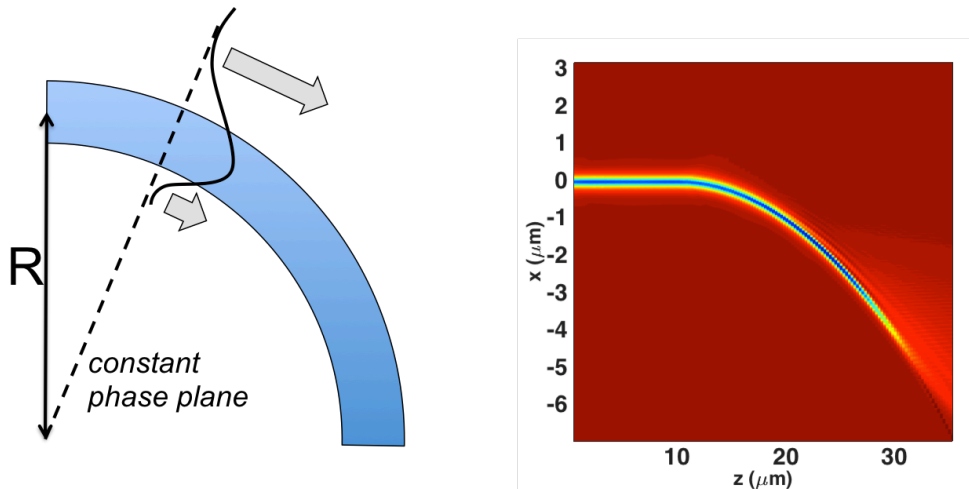
Figure 16. (Left) Schematic view of the fundamental mode propagating in a circular bend. Arrows indicate the tangential speed of the mode. (Right) Simulation of the fundamental mode using Beam Propagation Method showing mode leakage as it propagates through the bend.

Figure 16 (Right) shows this leaky phenomenon through a simulation of the optical mode propagation using a beam propagation method. The simulation displays the intensity of the electric field slowly radiating out as the mode propagates along the bend. This type of loss can be simulated using commercially available waveguide mode solving software

(FIMMWAVE). Figure 17 shows the result of the simulated bend loss as a function of bend radius for a 2.8 μm waveguide with a 70 nm thick core.
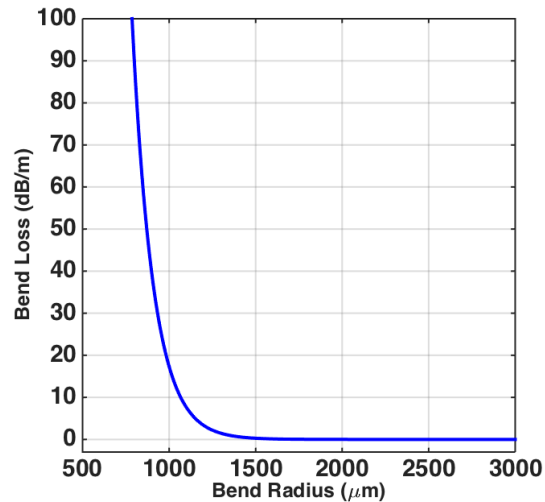
Figure 17. Simulated bend loss as a function of bend radius for a waveguide geometry of 2.8 μm x 70 nm.

The plot above shows that bend loss increases exponentially as the bend radius R decreases. It is important to note that the bend losses are negligible until a certain bend radius at which point the bend loss start to rise sharply. Therefore, any small change after that turning point can have a drastic effect on loss. Thus it becomes crucial to define a bend radius away from this turning point such that the bend losses are negligible with great margin of safety in case fabrication deviations are to occur. This chosen bend radius is often referred to as the minimum bend radius, and it will be defined here as the point where the bend losses reach 0.1 dB/m. By using this definition of minimum bend radius, an operating bend radius can be selected for several waveguide geometries. Figure 18 shows the simulated bend losses as a function of bend radius for multiple waveguide core thicknesses. Unlike the previous figure, the bend loss is plotted in dB such that it becomes clear where each curve crosses the minimum bend radius, shown as the black dashed line. As can be seen from the figure below, as the core thickness decreases the minimum bend radius becomes larger, which is a direct

31

result of "squeezing" out the mode so that it becomes weakly confined. Scattering loss on the contrary, as explained in the previous section, decreases as the core thickness becomes thinner. A trade-off between scattering loss and footprint arises, and the proper geometry must be selected according to the application requirements for footprint and insertion loss. This type of trade-off and geometry approach design will be highlighted in the subsequent chapters, and Figure 18 becomes an essential tool in analyzing the various geometries.
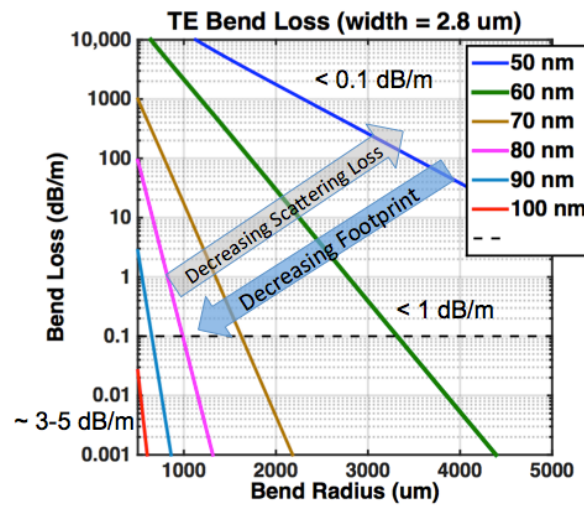
Figure 18. Series of design curves for proper design of PLCs. Each curve corresponds to waveguide geometry and the bend loss is plotted for each geometry as a function of bend radius. The minimum bend radius is defined as the point where the bend losses reach 0.1 dB/m and it is shown as the black dashed line.

2.5 Conclusion

In this chapter the ULLW platform was introduced and the fabrication process flow presented. The three major sources of waveguide loss were discussed separately and solutions for loss mitigation were provided for each. Measurements of scattering loss for fabricated waveguides were demonstrated with losses < 1dB/m, depending on the geometry selected. The absorption losses of the waveguides were then investigated and the material absorption was shown to decrease with a high temperature anneal due to the out diffusion of

hydrogen impurities. Lastly, the bend loss and the minimum bend radius definition were described. The minimum bend radius for several waveguide geometries was calculated and the trade-off between footprint and loss highlighted.

2.6 References

[1]   Bauters, J.F.; Heck, M.J.R.; John, D.; Ming-Chun Tien; Leinse, A.; Heideman, R.G.; Blumenthal, D.J.; Bowers, J.E., "Ultra-low loss silica-based waveguides with millimeter bend radius," in Optical Communication (ECOC), 2010 36th European Conference and Exhibition on , vol., no., pp.1-3, 19-23 Sept. 2010

[2]   Jared F. Bauters, Martijn J. R. Heck, Demis D. John, Jonathon S. Barton, Christiaan M. Bruinink, Arne Leinse, René G. Heideman, Daniel J. Blumenthal, and John E. Bowers, "Planar waveguides with less than 0.1 dB/m propagation loss fabricated with wafer bonding," Opt. Express 19, 24090-24101 (2011)

[3]   Demis John, "Etchless core-definition process for the realization of low loss glass waveguides,"Ph.D. dissertation, ECE Dept., UCSB, Santa Barbara, CA, 2012

[4]   Jared F. Bauters, Martijn J. R. Heck, Demis John, Daoxin Dai, Ming-Chun Tien, Jonathon S. Barton, Arne Leinse, René G. Heideman, Daniel J. Blumenthal, and John E. Bowers, "Ultra-low-loss high-aspect-ratio Si3N4 waveguides," Opt. Express 19, 3163-3174 (2011)

[5]   S. Franssila, Introduction to microfabrication. Chichester, West Sussex, England: J. Wiley, 2004.

[6]   Jared Bauters, "Ultra-Low Loss Waveguides with Application to Photonic Integrated Circuits," Ph.D. dissertation, ECE Dept., UCSB, Santa Barbara, CA, 2013.

[7]   Christi Madsen, Jian Zhao, "Optical Filter Design and Analysis: a Signal Processing Approach," (Wiley Series in Microwave and Optical Engineering) (15 June 1999)

[8]   F. Payne and J. Lacey, "A theoretical analysis of scattering loss from planar optical waveguides," Opt Quant Electron, vol. 26, no. 10, pp. 977986, 1994.

[9]   Siegfried Janz, "Silicon-Based Waveguide Technology for Wavelength Division Multiplexing," in Silicon Photonics, Springer, 2004, ch 10.

[10]   In Wook Cho ; Joon-Min Park ; Hyunsu Kim ; Joo-Yoo Hong ; Seong-Sue Kim ; Han-Ku Cho ; Hye-Keun Oh; Reduction of line width and edge roughness by resist reflow process for extreme ultra-violet lithography. Proc. SPIE 7273, Advances in Resist Materials and Processing Technology XXVI, 72732D (April 01, 2009);

[11]   Shipley, " DUV Photresist Advanced DUV Material," UV210 Datasheet, 2000

[12]   J. F. Bauters et al., "A comparison of approaches for ultra-low-loss waveguides," Optical Fiber Communication Conference and Exposition (OFC/NFOEC), 2012 and the National Fiber Optic Engineers Conference, Los Angeles, CA, 2012, pp. 1-3.

[13]   K. B. Koller, W. A. Schmidt, and J. E. Butler, "In situ infrared reflection absorption spectroscopic characterization of plasma enhanced chemical vapor deposited SiO_2 films," Journal of Applied Physics, vol. 64, no. 9, pp. 47044710, 1988.

[14]   W. Lanford and M. Rand, "The hydrogen content of plasma deposited silicon nitride," Journal of Applied Physics, vol. 49, no. 4, pp. 2473 2477, 2009.

[15]   R.Germann,H.W.M.Salemink,R.Beyeler,G.L.Bona,F.Horst,I.Massarek,andB.J.Offrein,Siliconoxynitride layers for optical waveguide applications, J. Electrochem. Soc. 147, 2237–2241 (2000).

[16]   G. L. Bora, R. Germann, and B. J. Offrein, SiON high refravtive-index waveguide and planar lightwave circuits, IBM J. Res. Dev. 47, 239–249 (2003).

Chapter 3

Design & Simulation

3.1 Introduction

Optical circuit simulations play a very important role in the development and design of planar lightwave circuit devices. By correctly predicting the optical circuit response through computer simulations, the number of fabrication cycles required to achieve desired circuit performance can be reduced saving time and cost.

In this chapter, a modeling tool is developed based on a transmission matrix (T-matrix) formalism, such that complex optical circuits can be rigorously analyzed before fabrication. The use of T-matrices allows complex planar lightwave circuits (PLCs) to be described by cascading individual building blocks reducing a complex circuit into simpler blocks [1]. The building blocks required for designing and fabricating each PLC presented in this dissertation are introduced with its respective transfer function and T-matrix. The physical layout and import design parameters are also evaluated and discussed.

3.2 T-Matrix formalism

All optical circuits and networks, independent of size, design and functionality, operate on an input signal in order to produce an output signal; all optical networks can be viewed as a system operating on a signal. A system can then be broken down into linear and

nonlinear, where a linear system is one which behaves linearly with respect to the input and typically exhibits features and properties that are much simpler than the nonlinear case [2].

Only linear optical circuits are considered in this dissertation and therefore, by definition, the optical circuit outputs can be linearly related to the inputs. Consider the four-port optical system (H) shown in Figure 19, where X_1 and X_2 are inputs and Y_1 and Y_2 are outputs of the system and negligible reflections are assumed.
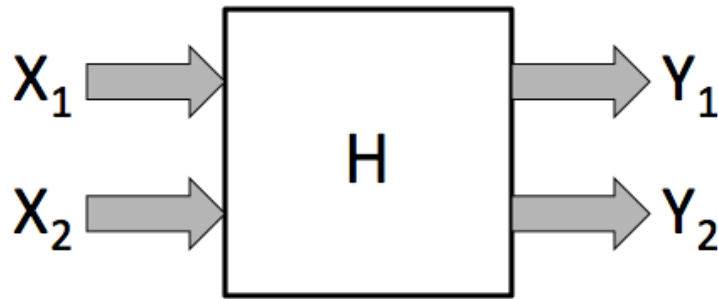
Figure 19. Schematic of a 4-port optical circuit.

A matrix formalism can be developed to represent the output as a weighted combination of the inputs. The output can be expressed by the set of linear equations below:

$$Y_1 = H_{11}X_1 + H_{12}X_2$$

$$Y_2 = H_{21}X_1 + H_{22}X_2$$

where H_{ij} are the weighting coefficients relating the output to the inputs. The system of equations can then be simplified by using the matrix formalism.

$$\begin{bmatrix} Y_1 \\ Y_2 \end{bmatrix} = \begin{bmatrix} H_{11} & H_{12} \\ H_{21} & H_{22} \end{bmatrix} \cdot \begin{bmatrix} X_1 \\ X_2 \end{bmatrix}$$

$$\boldsymbol{Y} = \boldsymbol{H} \cdot \boldsymbol{X}$$

where **Y** and **X** are column vectors and **H** is the T-matrix. The transmission matrix defined here can then be considered as a mathematical tool that provides a full description of how an

36

optical system will respond to a given signal. Now consider another optical system formed

by connecting two optical networks as shown in Figure 20.
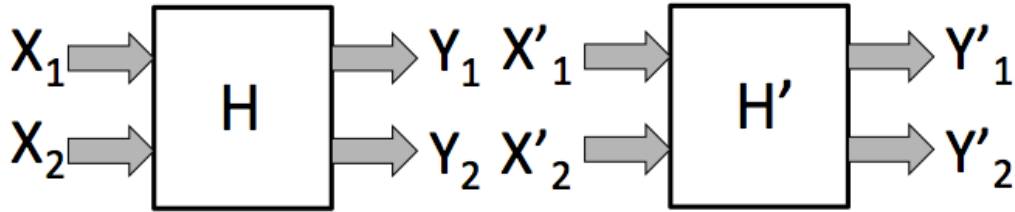
Figure 20. Schematic of two 4-port network cascaded together.

As before, both systems can be individually described as:

$$Y = H \cdot X$$

$$Y' = H' \cdot X'$$

When cascaded, the output of the first system becomes the input of the system making **X'** = **Y** and therefore the equation above can be rewritten as below:

$$Y' = H' \cdot X'$$

$$Y' = H' \cdot Y$$

$$Y' = H' \cdot H \cdot X$$

The equation shows that we can relate the output of the cascaded system to the input by a simple matrix multiplication of each individual system. This process can be continued to obtain the net transmission of arbitrarily complex planar lightwave circuits, provided each building block is known.

3.3 Building blocks

As described in section 3.2, complex optical networks can be described by cascading individual transfer matrices through matrix multiplication. Therefore, the building blocks in this section will form the basis for more complex planar lightwave circuits, particularly the optical circuits presented in chapter 1. A summary of the building blocks is shown in Table 4 together with important design parameters that will be discussed in the following subsections.

Block	Design Parameters
Waveguide delay	• Footprint • Crosstalk between adjacent waveguides • Waveguide loss
Differential delay	• Footprint/layout
Directional coupler	• Coupling ratio
Phase tuners	• Tuning efficiency • Tuning speed
Mach Zehnder interferometer	• Balanced vs. unbalanced • Coupler uniformity

Table 4.Summary of building blocks with important design parameters listed.

3.3.1 Waveguide delay

The most basic building block is the single-mode waveguide of length L. The transfer function of a simple waveguide is:

$$H = e^{-j\beta L}$$

where β is the waveguide propagation constant defined as $\beta = 2\pi n_{eff}/\lambda$ with n_{eff} as the effective index of refraction for the mode and λ as the wavelength. To include the waveguide propagation loss the effective index is treated as a complex number and the transfer function can be rewritten as:

$$H = e^{-j\frac{2\pi}{\lambda}(nr_{eff}-jni_{eff})L}$$

where nr_{eff} and ni_{eff} correspond to the real and imaginary part of the effective index, respectively. The equation above can then be reduced to:

$$H = e^{-ni_{eff}L} \cdot e^{-j\frac{2\pi}{\lambda}nr_{eff}L}$$

where the first multiplication term represents the waveguide attenuation. The waveguide's group delay can be calculated as:

$$\tau = \frac{L \cdot n_g}{c}$$

where n_g is the group index defined as:

$$n_g = n_{eff} + \lambda\frac{\partial n_{eff}}{\partial \lambda}$$

Footprint & Crosstalk

When dealing with long optical delays, as required for many delay line applications, waveguide losses and footprints play major roles in the design. Waveguide losses, which are typically quoted as loss per unit length, will set an upper limit on the waveguide length based upon the total desired insertion loss for the device. Similarly, the device's footprint requirement will limit the total length that can be integrated before compromising the desired footprint. To conserve footprint for delays with lengths of centimeters and greater, a spiral structure was used as shown in Figure 21.
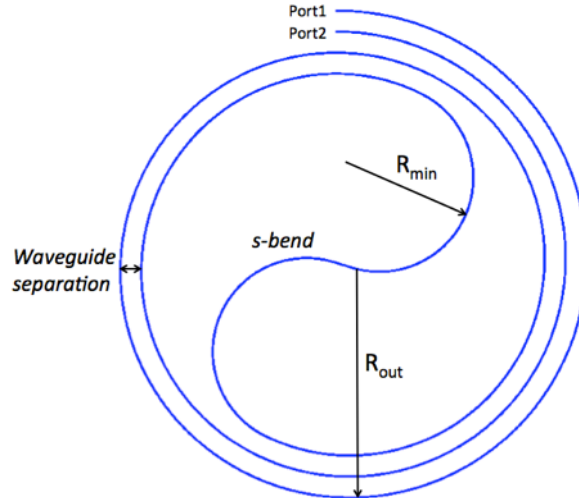
Figure 21. Schematic of a spiral delay with important parameters defined.

An Archimedean spiral is defined as a spiral that increases in distance from the point of origin at a constant rate, thus meaning each successive turn has a constant separation [3]. The configuration of an Archimedean spiral allows for an efficient way of integrating planar waveguide delays. Because an optical delay must have an input and output, the spiraling direction must be reversed to gain access to the other port, and that is achieved through the use of an s-bend as seen above.

The waveguide separation determines how "tightly" the spiral can be integrated and therefore must be minimized. The lower limit on the waveguide separation is determined by the amount of crosstalk tolerated by the system. As two waveguides are brought into close proximity, the existence of the index of one waveguide will perturb the optical mode of the other such that coherent coupling results [1]. Such waveguide coupling can be simulated through the use of commercial software (PhotonDesign FIMMWAVE) via an Eigen Mode Expansion (EME) algorithm, which is a rigorous solution of Maxwell's equations. Figure 22 shows the simulated crosstalk loss between two identical Si_3N_4 waveguides with a core

that is 80 nm in thickness and 2.8 μm wide, where crosstalk loss is defined as the amount of power coupled into the adjacent waveguide.
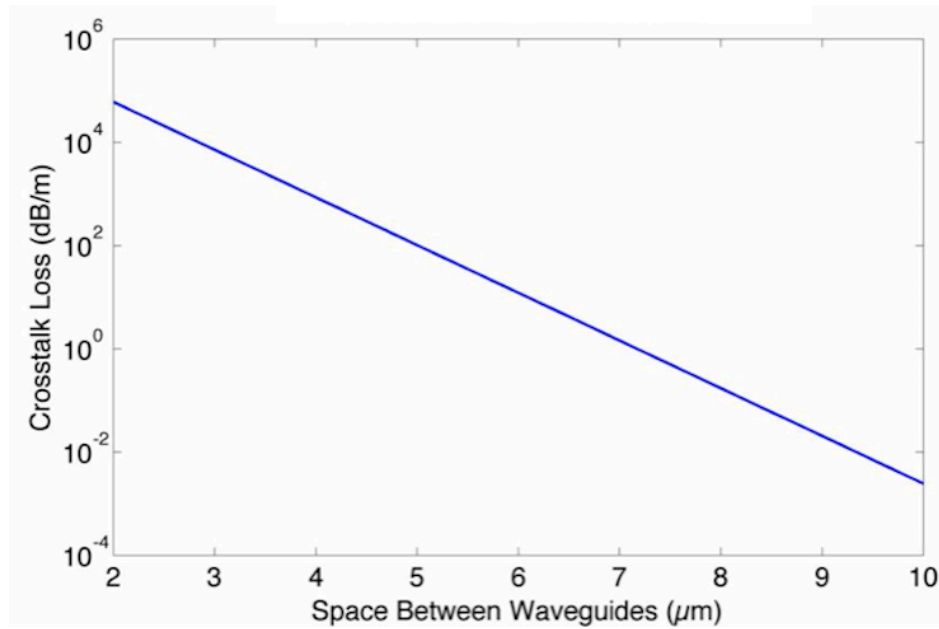
Figure 22. Simulated waveguide crosstalk as a function of waveguide separation. Waveguide geometry width = 2.8 μm, thickness = 80 nm.

The simulation was done for two straight waveguides, and therefore the bent mode profile was not considered in this case. Based on the simulation the waveguide separation can be chosen according the application's requirements. In order to maintain a negligible amount of crosstalk, a conservative waveguide separation of 50 μm was chosen for the waveguide delays in this dissertation.

Once the waveguide separation is selected the s-bend then becomes the limiting factor on the spiral's footprint, where the s-bend itself is limited by the smallest bend radius of curvature that can be used. As previously described, the minimum bend radius is a function of the chosen waveguide geometry where it is typically selected such that the bend losses are less than 0.1 dB/m (as defined by this work). The s-bend requires a total of four times the minimum bend radius (refer to Figure 21), and the smallest footprint possible for a spiral is

$F = \pi \cdot (2 \cdot R_{min})^2$. Figure 23 below displays the relationship of a spiral footprint as the minimum bend radius and waveguide separation varies while the waveguide length is held constant at 15 meters.
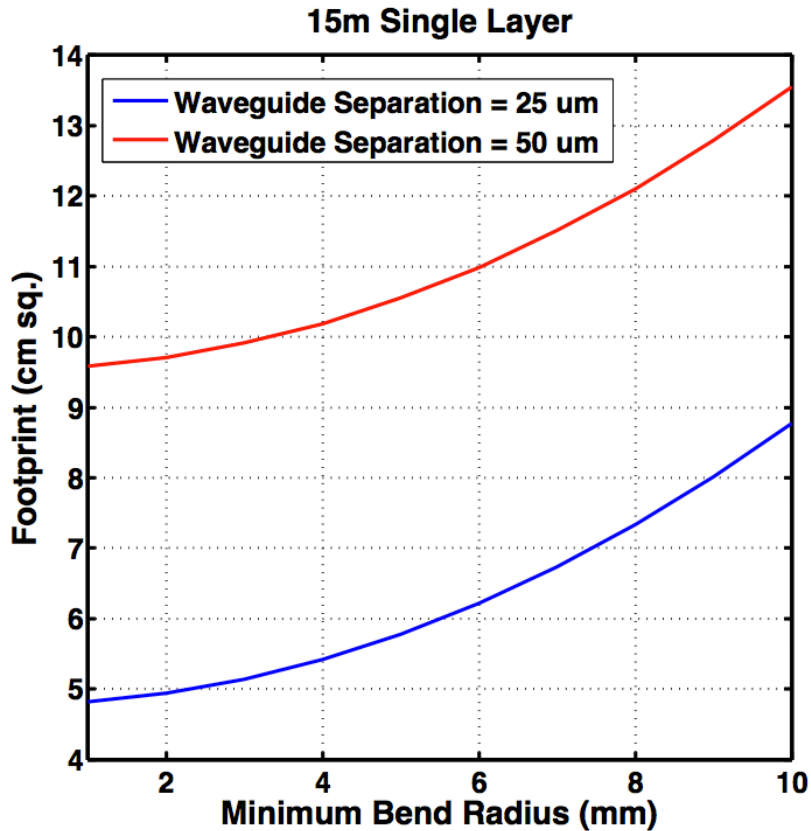
Figure 23. 15-meter spiral footprint as a function of minimum bend radius for two different waveguide spacing.

After the minimum bend radius and the waveguide separation is selected, the waveguide footprint increases linearly with length and is dependent on the number of turns (N) required to realize length (L). Figure 24 shows an example of a spiral footprint dependence on length for a minimum bend radius of 1 mm and a waveguide separation of 50μm.
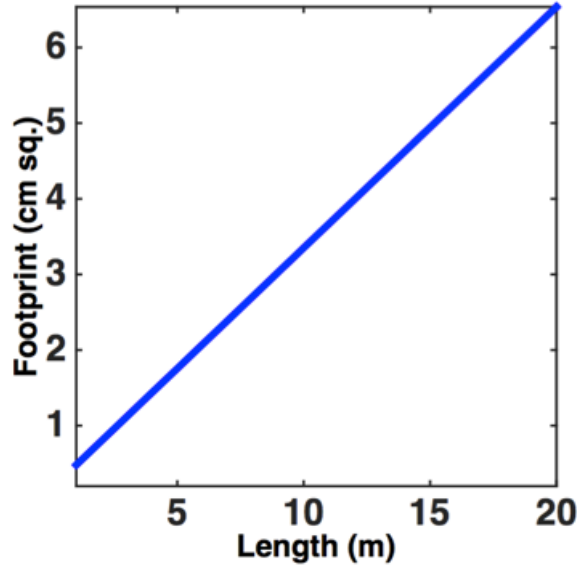
Figure 24. Spiral footprint as a function of waveguide length for a waveguide geometry with a minimum bend radius of 1mm and waveguide separation of 50μm.

3.3.2 Differential delay

While the simple waveguide from the previous section is a useful building block, most applications require the optical signal to always be delayed with respect to another waveguide thus forming a 4-port device as shown in Figure 25. By using the bottom waveguide as reference a differential delay can be defined as $\Delta L = L2 - L1$, where L2 and L1 are the propagation length of each waveguide. A differential loss can also be defined as $\gamma_{\Delta L} = e^{-\alpha\Delta L}$ where alpha is the absorption coefficient defined by the previous section as the complex component of the index of refraction. The four-port differential delay transfer function is:

$$H = \begin{bmatrix} \gamma_{\Delta L}e^{-jk_o n_{eff}\Delta L} & 0 \\ 0 & 1 \end{bmatrix}$$

where k_o is the vacuum wave number defined as $2\pi/\lambda$.
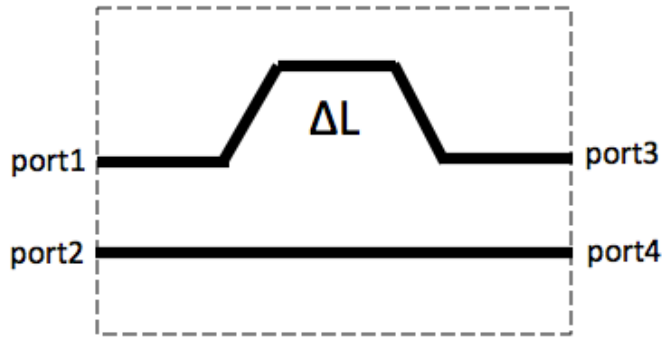
Figure 25. Four port differential delay schematic.

Layout

There are different ways to physically layout a differential delay and a description of the method of introducing a delay by using the radius of curvature as a design parameter is included herein. Figure 26 below shows the schematic of the physical layout of the differential delay. Everything from the left of the dashed line has a common length, and the differential delay is not introduced until the right of the dashed line. The minimum bend radius was used for the reference arm in order to conserve footprint, and therefore the required R for a given ΔL can be given as:

$$R = \frac{\Delta L}{\pi} + R_{min}$$

This type of delay layout provides a compact footprint for millimeter-differential delays only. For longer differential delays, the Archimedean spiral layout from section 3.3.1 can be utilized on the delay arm.
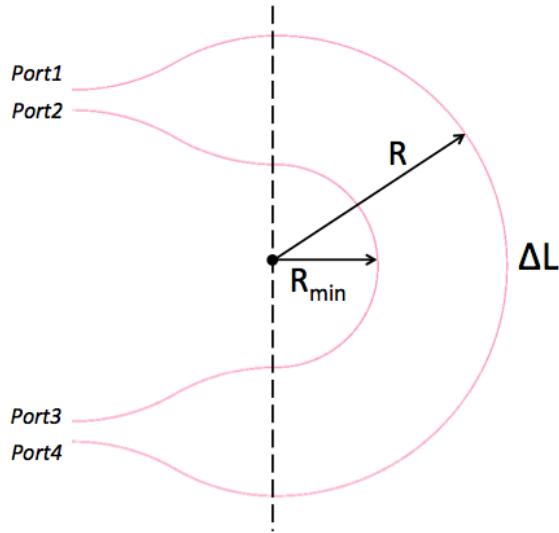
Figure 26. Physical layout of a differential delay by using different radius of curvature.

3.3.3 Directional coupler

The directional coupler is one of the most fundamental building blocks in almost any photonic integrated circuit. The directional coupler consists of two straight waveguides that are brought to close proximity of one another so that the fields can interact evanescently. Unlike section 3.3.1 where this power coupling between adjacent waveguides was considered as crosstalk loss, here if properly designed can be used to achieve power splitting. A schematic of the directional coupler is shown below (Figure 27).
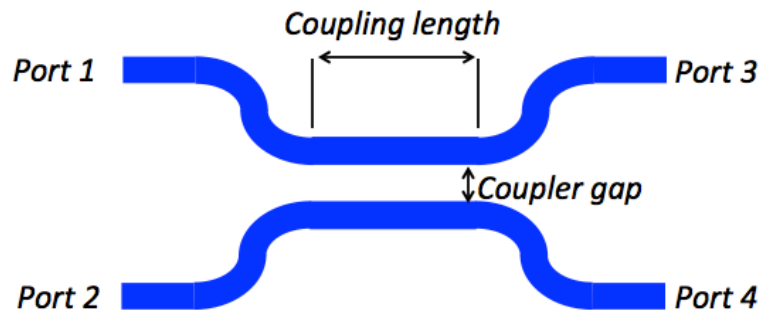
Figure 27. Schematic of a directional coupler.

For a symmetric coupler with identical waveguides, both even and odd modes of the system are excited on the coupling region where the coupler's mode can be written as the superposition of the even and odd modes. Because the even and odd modes have different propagation constants, their relative phase will change as they propagate down the coupler making the power cross from one waveguide to another as they propagate along the device. Figure 28 shows the electric field distribution on a symmetric directional coupler example with a splitting ration close to 50%.
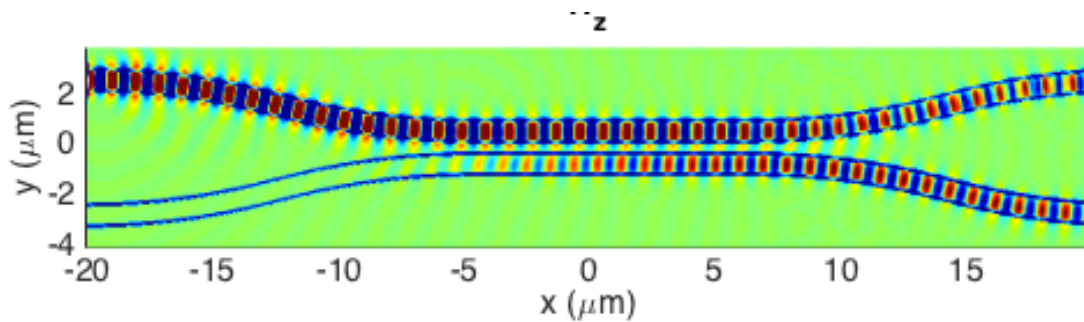
Figure 28. Direction coupler example showing the electric field propagation along the device.

The transfer function of such directional coupler is:

$$H = \begin{bmatrix} c & -js \\ -js & c \end{bmatrix}$$

Where c = √(1 − k) is the through transfer function and –js = -j√(k) is the cross transfer function, where k is the cross power coupling coefficient. The above transfer functions assume a lossless coupler and therefore $c^2 + s^2 = 1$.

The most critical factor that affects the magnitude of the coupling coefficient is the amount of overlap the evanescent tail of the optical mode has with the adjacent waveguide [2]. Thus, the waveguide separation has the largest physical effect on the coupling coefficient. It should also be noted that since the evanescent tail of the electric field decreases exponentially, the waveguide coupling also depends exponentially on the waveguide separation. Through

46

coupled-mode theory, as shown in Coldren & Corzine [1], the power for the through and cross ports for input in port 1 can be represented as:

$$P_{through} = cos^2(\kappa L + \phi)$$

$$P_{cross} = sin^2(\kappa L + \phi)$$

Where κ is the coupling coefficient and ϕ is the offset phase term introduced by the unwanted coupling in the curved waveguide section. Complete coupling from waveguide 1 to waveguide 2 then occurs when

$$\kappa L = (2n - 1)\frac{\pi}{2} \qquad n = 1,2,3,...$$

where the shortest length needed to complete crossing of the optical power between the waveguides is defined as the coupling length (L_c):

$$L_c = \frac{2\pi}{\kappa}$$

Therefore, to determine the coupling length for a directional coupler on the ULLW platform with a waveguide separation of 1μm, a test structure with 11 different coupling lengths was fabricated and tested on a waveguide geometry of 2.8 x 0.1 μm. The results allow for the directional coupler model to be calibrated and the 3dB coupler design to be determined. The results for the measured fabricated couplers and the model fit is shown in Figure 29, where the couplers were measured at a wavelength of 1550 nm at room temperature. From the measurements and fit shown, the optimal design for a 3dB coupler for this specific waveguide geometry is 255 μm for coupling length. As the geometry changes, the coupler design will need to be re-evaluated for that geometry.
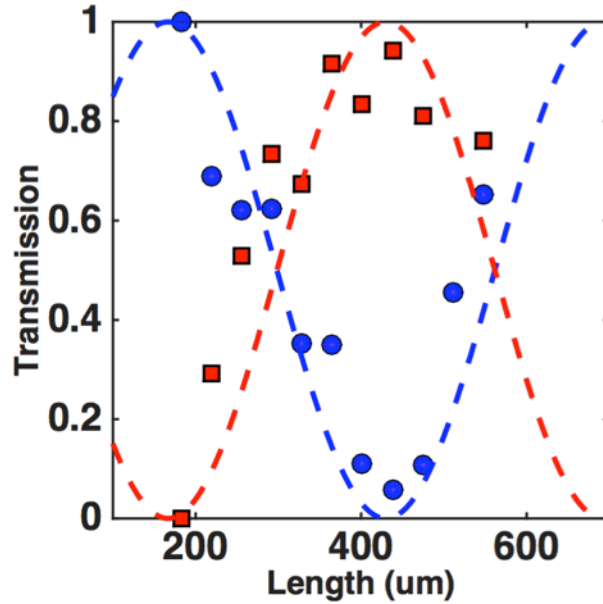
Figure 29. Measured coupler performance for a 2.8 x 0.1 µm waveguide with fit shown as the dashed lines for a 1 um coupling gap at 1550 nm wavelength measured at room temperature. (square points) measured cross data (circle points) measured through data.

3.3.4 Phase tuners

Introducing a small deviation from the average effective index of the waveguide can be used to perform a small tuning of the phase delay. The schematic of the phase tuning element is shown in Figure 30 and the corresponding transfer function is:

$$H = e^{-j\phi}$$

Figure 30. Schematic of phase tuning element.

Similar to the differential delay, a phase tuning can be relative to another waveguide forming a four-port device with an equivalent transfer matrix of:

$$H = \begin{bmatrix} e^{-j\phi} & 0 \\ 0 & 1 \end{bmatrix}$$

To demonstrate the utility of the t-matrix approach, the transmission matrix of a differential delay with a phase control as shown in Figure 31 can be calculated through a simple matrix multiplication:

$$H = H_{diff.delay} \cdot H_{phase\ tuner}$$

$$H = \begin{bmatrix} \gamma_{\Delta L} e^{-jk_o n_{eff} \Delta L} & 0 \\ 0 & 1 \end{bmatrix} \cdot \begin{bmatrix} e^{-j\phi} & 0 \\ 0 & 1 \end{bmatrix}$$

$$H = \begin{bmatrix} \gamma_{\Delta L} e^{-jk_o n_{eff} \Delta L} e^{-j\phi} & 0 \\ 0 & 1 \end{bmatrix}$$
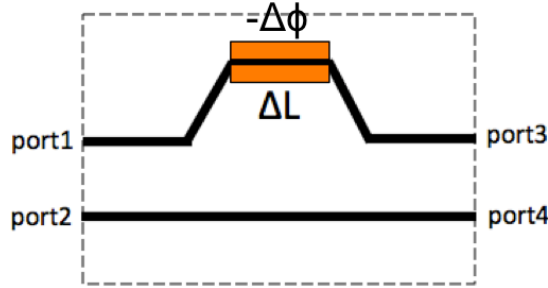
Figure 31. Schematic of differential delay with phase control.

Layout & Loss

One way to introduce a phase shift is through the use of the thermo-optic effect, which changes the index of refraction of a given material at different temperatures applied [4]. Therefore, the phase difference can be described by:

$$\Delta\phi = k \cdot \Delta n \cdot L = \frac{2\pi}{\lambda} \cdot \frac{dn}{dT} \cdot \Delta T \cdot L$$

Where dn/dT is defined as the thermo-optic coefficient and is essentially a material property. The thermo-optic coefficient for the silica upper cladding used on the ULLW is 1 x 10^{-5} °C^{-1},

which is an order of magnitude smaller than silicon [5]. Typical tuning speeds for silica are on the order of milliseconds.

A very crucial part of the phase tuner is the heater itself, which can be realized by driving a current through a resistive stripe deposited on top of the cladding. The heating element is most typically a metal and in this case we use NiCr deposited via e-beam assisted evaporation, where the element is patterned through a liftoff process. To allow for better control of the NiCr heater composition, a digital layer deposition technique was used, where alternating layers of Nickel and Chrome were separately deposited and then later alloyed through annealing [6].
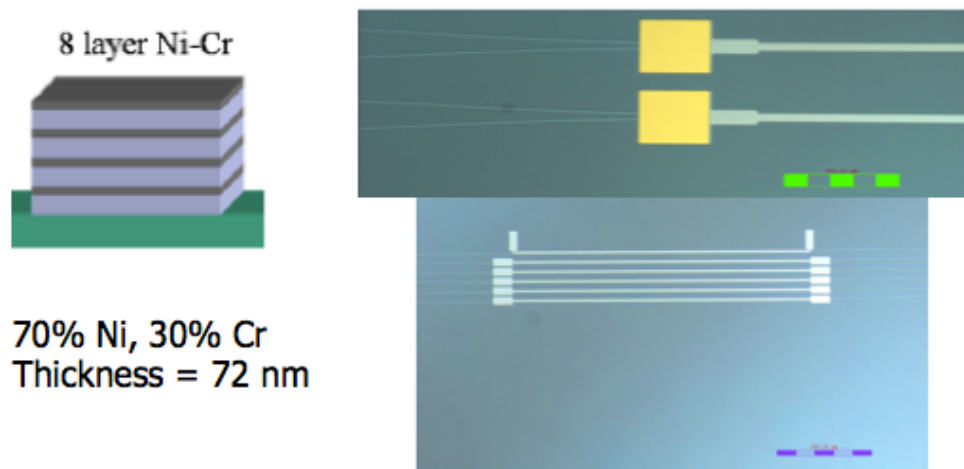
Figure 32. (Left) NiCr heater schematic. (Right) Optical microscope images of the fabricated heaters.

In this process, a total of 8 layers were used to form an alloy composition of 70% Nickel and 30% Cr which was achieved by tailoring the thickness of each individual layer, where at the end the total thickness of the heater was approximately 72 nm and 10 μm. Figure 32 above shows a schematic of the designed heaters together with microscope images of the fabricated devices, which were measured to have a sheet resistance of 5 Ω/square. Special care must be taken when designing such heater devices as to avoid any metal

interaction with the optical mode. This interaction can be avoided by placing the heater far away from the waveguide core through the addition of upper cladding. The amount of metal absorption loss as a function of the amount of upper cladding is shown in Figure 33, which was achieved through simulation via FIMMPROP. As seen from the plot, the further away the heater is placed from the waveguide core the lower the propagation loss, but that is only achieved through the trade-off of phase tuner optimized operation; for example, decreased heating speed and increased operation power [7]. The plot below was done for a core thickness of 100 nm in which case a 3 μm of upper cladding was chosen corresponding to a loss of <2 dB/m, which makes the metal absorption loss negligible since the length of each heater is typically in the order of a 100s of microns. The plot needs to be re-calculated different waveguide geometries since mode confinement and metal overlap can drastically change. As a proof of concept, tuning speed and tuning power were not optimized for any of the application presented in this dissertation.
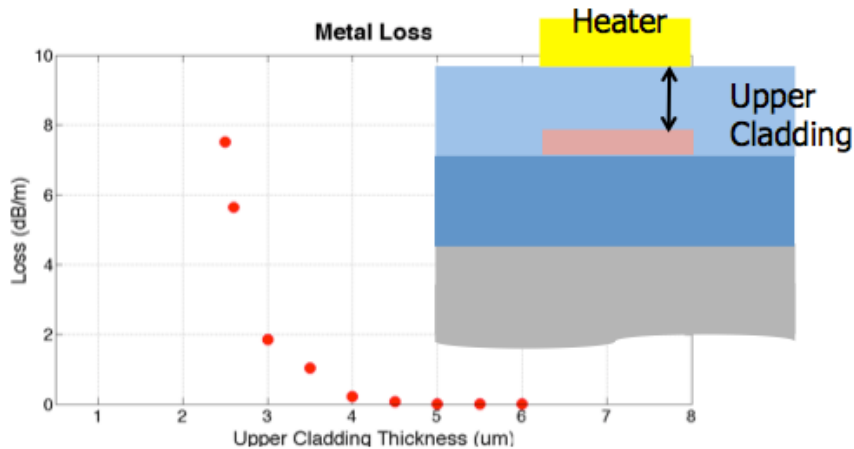
Figure 33.Simulated upper metal absorption loss as a function of upper cladding.

3.3.5 Mach-Zehnder Interferometer (MZI)

The MZI is a single stage optical filter where the output response arises from the interference of two waves that are delayed relative to each other. In order for interference to happen the two waves must be of the same polarization and temporally coherent over the longest wavelength [8]. Their relative phases will then determine if they interfere constructively or destructively. The symmetric MZI is composed of two equal directional couplers connected together by two waveguides of equal lengths as shown in Figure 34. By placing a phase tuner in one of the MZI arms and tuning the phase accordingly, the power coupling of the MZI can then be changed making it a suitable device for use as a tunable coupler or as an optical switch.
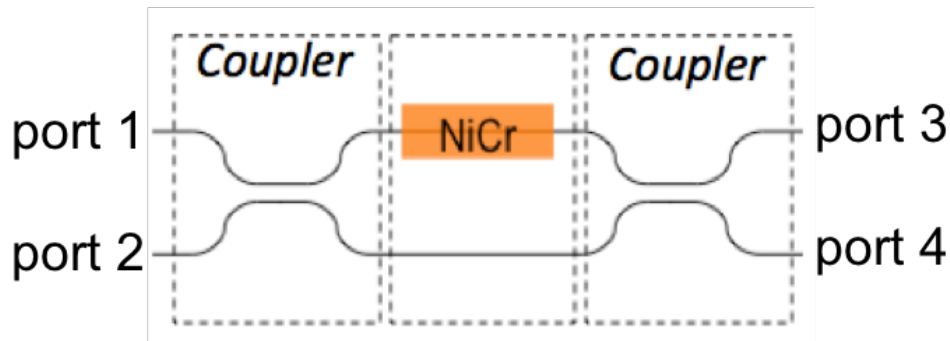
Figure 34. Schematic of the MZI.

Because the transfer function of each separate element of the MZI has already been defined, the MZI transfer function can then be simply described as the multiplication of each of its element transfer function:

$$H_{MZI} = H_{coupler1} \cdot H_{delay} \cdot H_{coupler2}$$

Thus making the overall MZI transfer function equal to:

$$H_{MZI} = \begin{bmatrix} -s^2 + c^2 e^{-j\varphi} & -jsc(1 + e^{-j\varphi}) \\ -jsc(1 + e^{-j\varphi}) & c^2 - s^2 e^{-j\varphi} \end{bmatrix}$$

where s and c, as described in section 3.3.3, are equal to:

$$c = \sqrt{1-k}$$

$$s = \sqrt{k}$$

with k being the cross power coupling coefficient. If we assume an input only in port 1, then the transmission at each output port is equivalent to $|H_{11}|^2$ and $|H_{21}|^2$, which can be written as:

$$|H_{11}|^2 = (1-k)^2 + k^2 - 2k(1-k)\cos(\phi) \qquad [Port\ 3]$$

$$|H_{21}|^2 = 4k(1-k)\cos^2\left(\frac{\phi}{2}\right) \qquad [Port\ 4]$$

As of a result of the equations above, the MZI can be used as a tunable coupler by controlling the phase ϕ, which can vary the overall coupling ratio between the values of 0 and 1. If we look at the output equation for port 4, we can see that the maximum output power of 1 can only be achieved if the phase is set to π and k is equal to 0.5. In reality, the coupling ratio will vary from their design values due to variations in the fabrication process and as a result so will the MZI response. Figure 35 shows the magnitude response of a symmetric MZI for multiple coupling coefficients. As the coupler deviates from the nominal 50% the extinction ratio of port 3 starts to suffer, therefore highlighting the importance of achieving the proper coupler design.
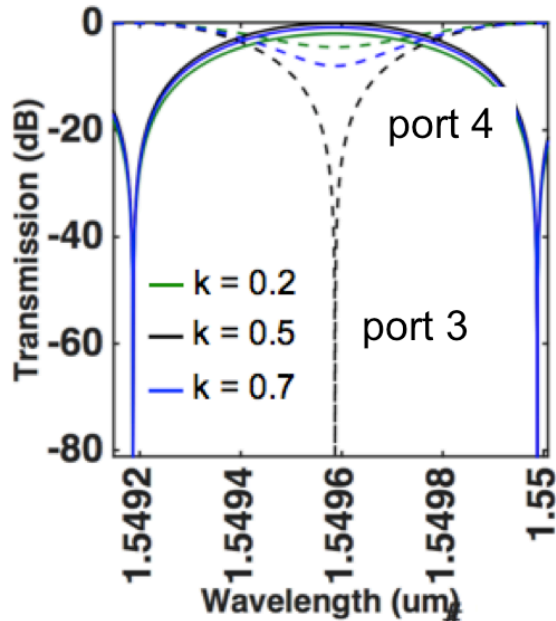
Figure 35. Theoretical transmission for the symmetric MZI filter for a coupling coefficient of 0.2, 0.5, and 0.7.

Also, when describing the MZI transfer function we assumed a constant coupling ratio for the wavelength region of interest, which is a good assumption for a small wavelength range. This assumption breaks down for hundreds of nanometers and a significant change in filter response can be experienced.

3.4 Conclusion

In this chapter, a modeling tool based on a transmission matrix formalism was introduced. The t-matrix approach demonstrated that the representation of a complex planar lightwave circuit could be achieved through simple matrix multiplication. This approach therefore reduces a large complex circuit into simpler and smaller building blocks. All the building blocks required for the analysis of the photonics circuits presented in this dissertation were then introduced with each respective t-matrix. A brief discussion for each

block with important design parameters was also presented. Table 1 below presents a summary of all the transfer functions introduced in this chapter.
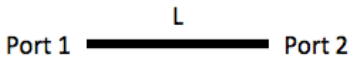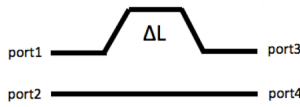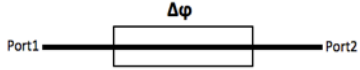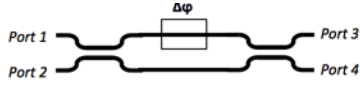
Device	Schematic	Transfer Function
Waveguide delay		$H = e^{-\alpha L} e^{-jk_o n_{eff} L}$
Differential delay		$H = \begin{bmatrix} \gamma_{\Delta L} e^{-jk_o n_{eff} \Delta L} & 0 \\ 0 & 1 \end{bmatrix}$
Directional coupler		$H = \begin{bmatrix} c & -js \\ -js & c \end{bmatrix}$
Phase tuner		$H = e^{-j\phi}$
MZI		$H = \begin{bmatrix} -s^2 + c^2 e^{-j\varphi} & -jsc(1 + e^{-j\varphi}) \\ -jsc(1 + e^{-j\varphi}) & c^2 - s^2 e^{-j\varphi} \end{bmatrix}$

Table 5. Summary of building blocks and their equivalent transfer function.

3.5 References

[1] Coldren, Larry A., Scott W. Corzine, and Milan L. Mashanovitch. Diode lasers and photonic integrated circuits. Vol. 218. Wiley. com, 2012.

[2] C. K. Madsen and J. H. Zhao, Optical Filter Design and Analysis: A Signal Processing Approach. (Wiley- Interscience, 1999).

[3] JIANG Xiao-Jun,LI Xiao-Lin,XU Xin-Ping. Archimedean-Spiral-Based Microchip Ring Waveguide for Cold Atoms [J]. Chin. Phys. Lett., 2015,

[4] Coppola G, Sirleto L, Rendina I, Iodice M, "Advance in thermo-optical switches: principles, materials, design, and device structure" Opt. Eng. 50(7):071112-071112-14.

[5] Kasahara, R.; Yanagisawa, Masahiro; Goh, T.; Sugita, A.; Himeno, A.; Yasu, M.; Matsui, S., "New structure of silica-based planar lightwave circuits for low-power thermooptic switch and its application to 8×8 optical matrix switch," in Lightwave Technology, Journal of , vol.20, no.6, pp.993-1000, Jun 2002

[6] Dummer, M.M.; Sysak, M.N.; Tauke-Pedretti, A.; Raring, J.W.; Klamkin, J.; Coldren, L.A., "Widely Tunable Separate Absorption and Modulation Wavelength Converter With Integrated Microwave Termination," in Lightwave Technology, Journal of , vol.26, no.8, pp.938-944, April15, 2008

[7] S. Sohma, T. Goh, H. Okazaki, M. Okuno and A. Sugita, "Low switching power silica-based super high delta thermo-optic switch with heat insulating grooves," Electronics Letters, vol.38, no.3, January 2002.

[8] Günay Yurtsever, Boris Považay, Aneesh Alex, Behrooz Zabihian, Wolfgang Drexler, and Roel Baets, "Photonic integrated Mach-Zehnder interferometer with an on-chip reference arm for optical coherence tomography," Biomed. Opt. Express 5, 1050-1061 (2014)

Chapter 4

Optical True Time Delay (OTTD)

4.1 Introduction

Optical true time delays (TTDs) are an effective solution for broadband phased array antenna applications in order to reduce beam-squint, or beam deformation due to frequency change, and electromagnetic interference [1]. Optical TTDs for large aperture antennas and arrays with a high number of elements require delay lengths on the tens of nanosecond scale. Several fiber based optical TTDs have been demonstrated at much longer range [2-3], which are attractive due to their low propagation loss but suffer from the fact that they are bulky and must have their length precisely cleaved in order to achieve accurate delays. As a result, integration of such devices would benefit the system by decreasing the footprint, increasing the delay accuracy, increasing stability, and reducing cost. Although many fully integrated optical TTDs have been demonstrated [4]-[7], the maximum amount of delay is usually limited by high propagation loss limiting the delay time to the picosecond to a few nanosecond range. We have recently demonstrated record low propagation losses in a Si_3N_4/SiO_2 planar waveguide technology, which allows for long delays to be implemented on chip scale devices.

This work presents the fabrication of the longest fully integrated 4-bit true time delay on the ultra-low-loss planar Si_3N_4/SiO_2 platform with delays up to 12.35 ns. The device

presented herein is also easily scalable for even longer delay lines and higher bit count delays

given the low propagation loss of the platform.

4.2 Theory

Phased array antennas (PAAs) are used in a variety of military and civil applications such as radar, weather radar, and wireless communication systems [8]. A PAA consists of multiple closed spaced antennas where the beam can be steered by controlling the relative phase between each antenna element. Figure 36 shows an example of a 4-antenna element linear array each separated by an equal distance d. Although an analytic antenna field pattern can be defined, more simply the beam direction θ can be related to the antenna phase delay $\Delta\phi$ by assuming that at the far field each individual element transmits a plane wave.
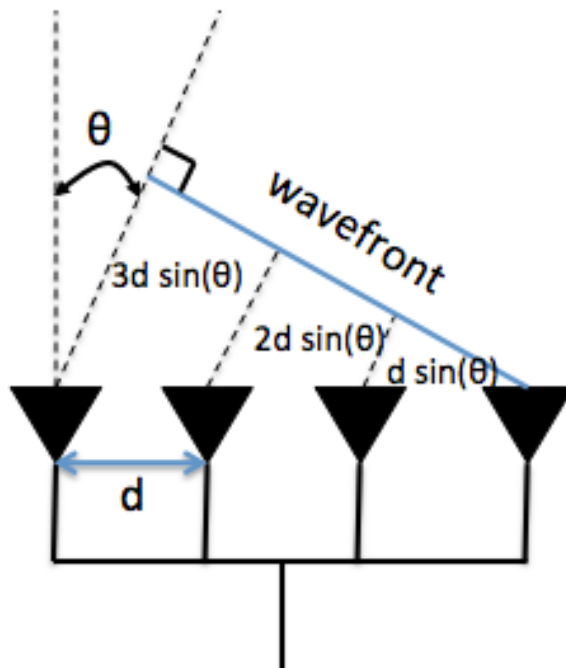
Figure 36: Illustration of a 4-element linear phased array antennas.

For the plane waves to interfere constructively at an angle θ then, as described in Figure 36, each adjacent antenna element must differ in path length by $d \cdot \sin(\theta)$, where d is the distance between elements. Therefore the time delay at each element, assuming free-space is:

$$\Delta t = \frac{d \cdot sin(\theta)}{c}$$

where c is the speed of light in free-space. Then the phase shift required at each antenna element is:

$$\Delta \phi = 2\pi f \Delta t = \frac{2\pi \cdot f \cdot sin(\theta)}{c}$$

where f is the operating RF frequency in Hz. An electronic phase tuner can be used to easily apply the phase shift required, however as the equation above suggests, the phase shift approach is always dependent on the RF operating frequency thus suffering from beam squinting. Because the phase shift is designed for a specific RF frequency, the beam will deform and point at a different undesired direction as the frequency changes; therefore, phase tuners cannot be optimally used in broadband operation of future PAA systems. Consequently, in order to fully avoid beam squinting the phase shift can be replaced by a true time delay (TTD), where each antenna excitation is delayed by appropriate amount of time:

$$\Delta t = \frac{d \cdot sin(\theta)}{c}$$

which as shown has no dependence on the RF operating frequency. Time delays have traditionally been impractical to implement in the electrical domain due to their loss, cost, weight and power limitation. On the other hand, the high cost and complexity of PAAs are mainly tied to the electronic phase shifters and thus restrict the technology mostly to military applications. Figure 37 shows a picture of SBX-1, which is the largest and most

sophisticated phased array electro-mechanically steered X-band radar in the world where approximately 45,000 transmit/receive modules are used to form the radar beam [9].

Figure 37: Sea-Based X-Band Radar-1 (SBX-1).

By implementing the time delays in the optical domain through the use of optical waveguides, they can replace bulky, heavy and lossy coaxial cables making PAA technology more accessible. However, integrated optical waveguide losses are usually the limiting factor in implementing the long time delays required for large beam tunability, therefore the ULLW platform presented here makes long optical true time delays feasible where they are otherwise not accessible on any other integration platform.
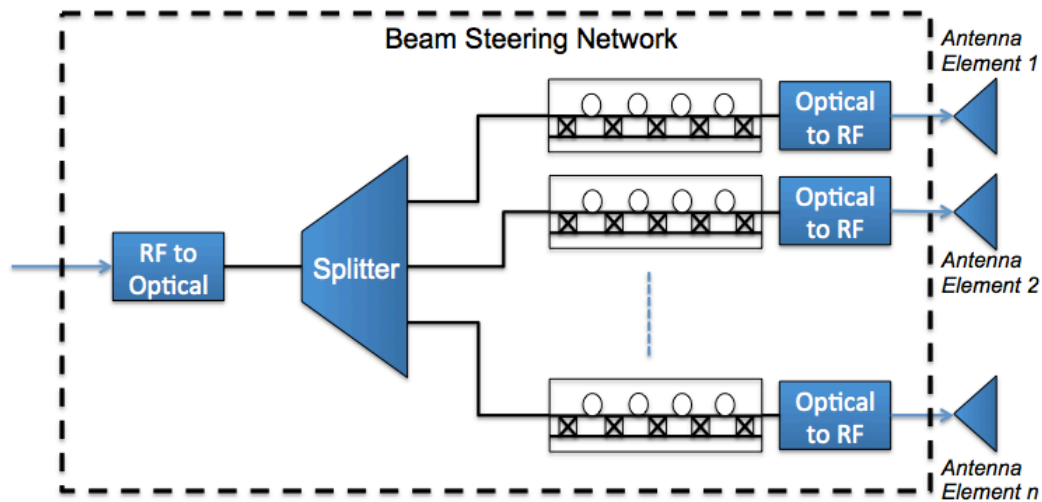
Figure 38: Schematic of a simple optical beam steering network.

Figure 38 above shows a simple illustration of an optical beam steering/forming network. At the input to the network on the left side of the diagram the RF signal to be transmitted is converted to an optical signal, which is usually directly modulated into an optical carrier. The optical carrier is then split into multiple signals which are delayed by an individual OTTD. The delayed signals are then detected by photodetector converting the optical signal back to RF, which is used to drive each antenna element after amplification. Although the entire beamforming network can be integrated into a photonics single chip, this chapter of the dissertation discusses the integration of the delay chips alone. The implementation of the active could be achieved through an active/passive approach first demonstrated at [10].

For phased array antenna systems, multiple antennas are combined to enhance radiation and shape pattern; therefore, the larger the number of antennas elements the more directional and efficient the radiating beam will be. Also, in order to reduce the grating lobes the antennas are generally placed $\lambda/2$ apart [11]. Therefore, if we assume an X-band radar operating at 8 GHz with antennas spaced by 18.75 mm, which corresponds to half of the operating wavelength, in order to steer the beam to a maximum angle of 90° a Δt of at least

62.5 ps is required. A typical phased array antenna for military applications includes on the order of hundreds of elements in a single system; taking the previous example into consideration, 10s of nanoseconds of optical delay would be required to implement an integrated TTD, which is equivalent to meters of waveguide propagation. Such integration is only achievable in a low loss waveguide platform such as the one presented here.

4.3 Design

One of the most common ways of implementing an optical true time delay is through a switched delay line, sometimes referred to as a binary optical delay line (BODL). A schematic of a 4-bit binary optical true time delay example is shown in Figure 4 below.
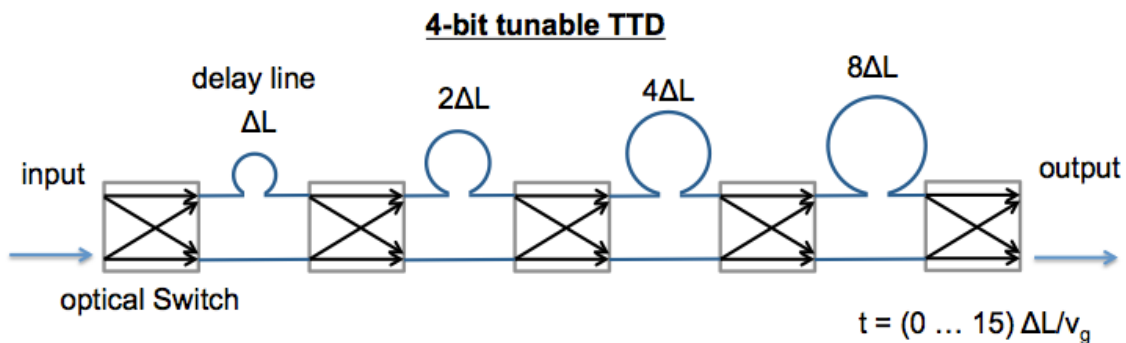
Figure 39: Example of a 4-bit switched delay line implementation of an optical true time delay.

The BODL is composed of N delay lines with lengths successively increasing by a factor of 2, where the optical signal can be routed via (N+1) optical switches cascaded between each delay. By turning all the switches off, the signal will bypass all of the optical delay lines for an equivalent of a zero delay, but if a single switch is turned on or a combination of switches then the optical signal can be routed through a single delay or a combination of delays which can take any value in increments of ΔT all the way to the maximum delay time of T_{max} by

turning on all of the delay lines. For a general BODL there are a total of 2N delays where the shortest delay line ΔL sets the device resolution and the maximum delay is represented by:

$$T_{max} = (2^0 + 2^1 + 2^2 + \cdots + 2^{N-1}) \cdot \Delta T = (2^N - 1) \cdot \Delta T$$

The desired delay time ΔT can then be set according to $\Delta L / v_{group}$, where v_{group} is the group velocity of the signal represented by c/n_{group}, and ΔL is the length difference between the bypass line and the delay line. In the example provided of the 4-bit true time delay, there are a total of 16 possible delays from (0 ΔT) all the way up to (15 ΔT) in increments of ΔT.

To integrate the delay lines if the required delay length is long enough, the Archimedean spiral architecture is used to conserve footprint; otherwise if the length necessary is short then the different path length will be implemented simply through curved waveguides. An example of both types of delays will be demonstrated in the next section. The optical switch architecture for this work was implemented with the symmetric Mach Zehnder interferometer where a π phase shift is required to change the switch state (ON-OFF) which can be introduced via the thermo-optic effect through NiCr heaters deposition on the MZI arms as previously described.

4.4 Results

The true time delays presented in this work were not designed for any specific phased array antenna system, but the choice of delay line lengths were strictly chosen to highlight the ultra-low loss characteristics of the platform by integrating the longest switched delay line. Because of the long delay lines on chip, such devices would be useful for the next generation broadband X-band radar, where the shorter wavelengths are useful for higher resolution but as the number of antenna elements increase longer delay lines will be required

to provide a wide scanning range. Two generations of devices were fabricated to demonstrate the feasibility of the new platform. This section is broken down into 3 subsections where the chosen waveguide geometry is first presented with waveguide loss measurements, and then the results of the true time delay for generation 1 and generation 2 are presented. The purpose of the first generation was solely to develop the building blocks required for implementing the complete OTTD.

4.4.1 Waveguide Geometry

As previously stated, waveguide propagation loss is the limiting factor in integrating very long delay lines. Therefore, with the new planar ULLW platform longer delay lines can be integrated at relatively low integration loss not otherwise feasible in any other platform. As a result, to demonstrate the flexibility of such platform the requirements for the true time delays designed here are listed below:

- Low propagation (< 1 dB/m) loss for long delay line integration (delay length > 1m)

- Relaxed footprint constraints (~5 mm bend radius still ok) – photonic integration even at large bend radii should still be an improvement over its electronic counterpart.

From the previous chapter, the ULLW platform has a trade-off between waveguide propagation loss and footprint (bend radius), where both cannot be simultaneously met such as ultra low propagation loss at a very small bend radius. The requirements for the true time delay listed above do not conflict with the trade-off described since the footprint condition is not very demanding. As a result, the waveguide propagation loss requirement is a deciding factor. Figure 40 shows the simulations of multiple waveguide core geometries where the bend loss is plotted as a function of bend radius for different core thicknesses and the scattering loss of some of the waveguides is also listed beside the curve. From the plot, the

only curves that meet the requirement of the propagation loss less than 1 dB/m are the 60 nm and 50 nm thick cores. Thus to determine the bending capability for each geometry the minimum bend radius is defined as the point where the bend loss is equal to 0.1 dB/m, which is marked as a dashed line on the plot. The intersection of each curve with the dashed line determines the minimum bend radius that can be used, which corresponds to 3.5 mm for the 60 nm thick core and > 5mm bend radius for the 50 nm thick core. Therefore, the geometry that meets the entirety of the requirements for the given application is the 60 nm thick core.
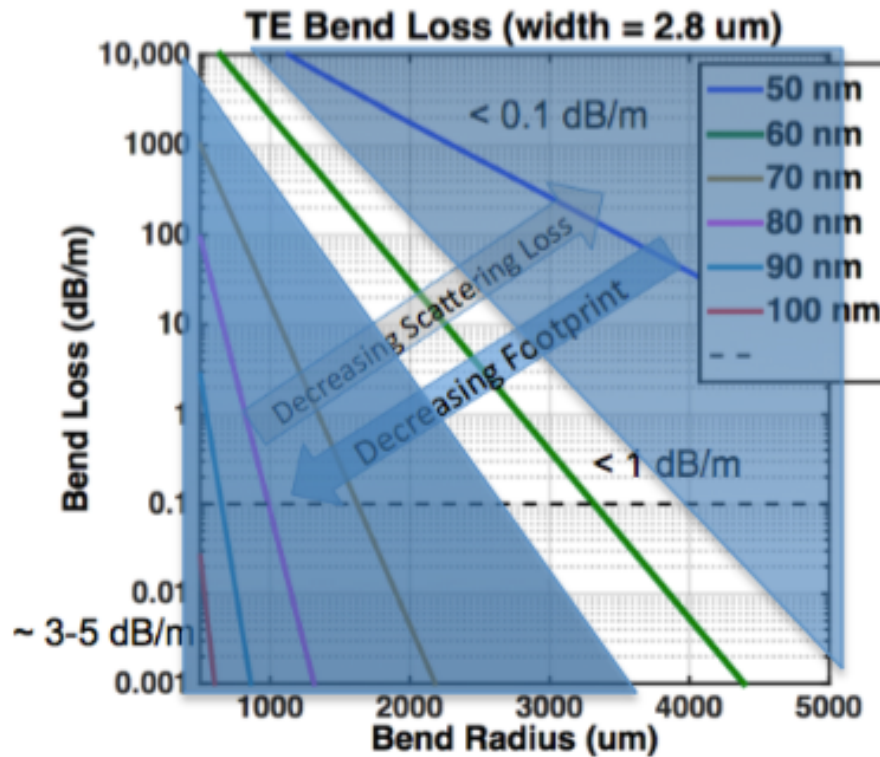
Figure 40: Waveguide core dimension design space for the integrated optical true time delay.

Although the simulations shown in Figure 40 were all based on a waveguide core width of 2.8 um, some of the waveguide geometries can be made wider and still satisfy the single-mode condition. In the case of the waveguide geometry chosen for the true time delay application (60 nm thick core), the single mode condition is a waveguide core width of < 5.5

um. By making the core wider the bending capabilities and waveguide propagation loss can be improved slightly. As a result the optical true time delay used a waveguide geometry of 7 x 0.06 um making the waveguide "quasi-single" mode where a long adiabatic taper is used in order to excite the fundamental mode alone. By narrowing the core width to much lower than the single mode condition, in this case 1 μm, the waveguide optical mode can reach a regime where the horizontal and vertical confinement are at its lowest making it best matched to a fiber mode resulting in low coupling loss. Therefore, simply tapering the waveguide from 7 μm to 1 μm can make low loss spot size converters.

The propagation loss of the waveguides was measured by optical frequency domain reflectometry (OFDR). Using a 1- meter spiraled waveguide test structure, the backscattered optical power was measured using a Luna OBR 4400 commercial reflectometer and the propagation loss extracted. Figure 41 displays the TE loss as a function of wavelength for the designed waveguide. The TE loss was measured to be (1.01 ± 0.06) dB/m at 1550 nm wavelength, reaching a low- loss point of (0.57 ± 0.08) dB/m at 1591 nm. The waveguide loss displays a wavelength dependent spectrum and structures, which are a direct result of the absorption loss due to molecular bond resonances due to hydrogen impurities as seen in [12].

The devices presented in this chapter were partially fabricated at Lionix BV in the Netherlands and partially at UCSB, where the inset in Figure 41 shows where each portion of the waveguide was fabricated. The phase tuners fabricated at UCSB were placed 6 um above the waveguide core as to avoid any interference with the optical mode.
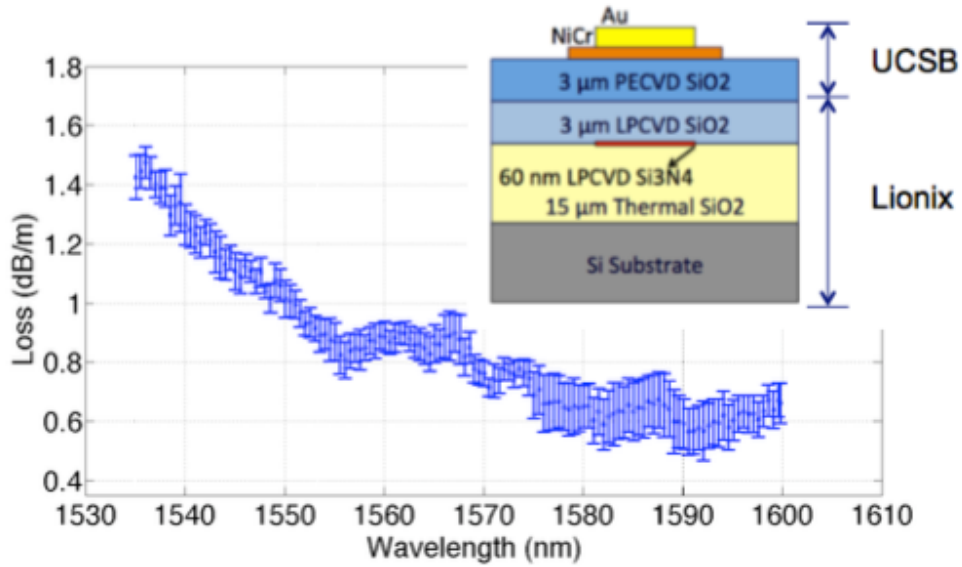
Figure 41: Measured waveguide loss for the 60 nm thick core. (Inset) Waveguide cross-section schematic with fabrication location breakdown.

As a conclusion, from the waveguide measurements presented here the waveguide geometry satisfied the required constraints for the fabrication of long programmable optical true time delay for phased array antennas applications. The waveguide platform can be summarized in Figure 42 where important measured values are listed.

Parameter	Value
Core size	7 um x 0.06 um
Propagation loss (@ 1550 nm)	1.01 ± 0.06 dB/m
Lowest propagation loss	0.57 ± 0.08 dB/m
Bend radius	3.5 mm

Figure 42: Summary of the waveguide platform for the optical true time delay.

4.4.2 TTD: Generation 1

The first generation of the true time delay was designed specifically to establish the building blocks required to layout a complete and optimized true time delay. Therefore, the switched delay had shorter propagation lengths in the order of centimeters as to reduce complexity, which corresponded to a few picoseconds delay. The process run mainly consisted of couplers and switches test structures, which were used to verify the overall performance of the device.

A 4-bit switched delay was implemented according to the schematic in Figure 43 left. As shown in the figure a folded approach was used to conserve footprint and the actual reticle layout is shown in the same figure (right).
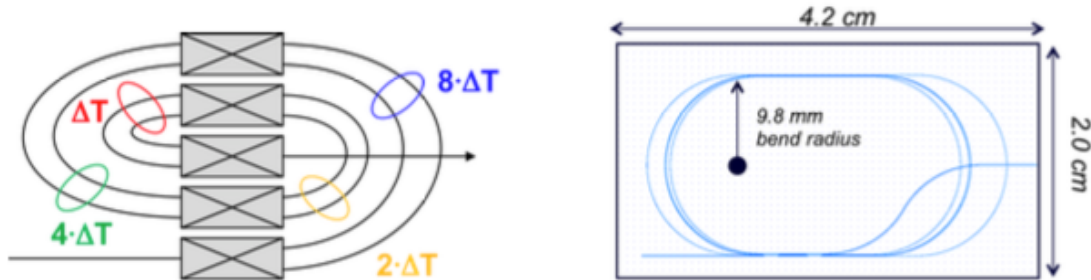
Figure 43: (Left) Schematic of the Gen. 1 true time delay with a folded architecture and waveguide crossings showing the location of each delay line. (Right) GDS layout of the fabricate device displaying the minimum bend radius used and the device footprint.

The waveguide crossings were done at 90 degrees and were simulated and measured with a cutback method to have 0.06 dB/crossing, a more in depth waveguide crossing investigation will be done in the optical gyroscope chapter. Although a smaller bend radius could be used as previously described, a more conservative minimum bend radius of 9.8 mm was used since the total delay for the first generation was < 5 cm and a feasible footprint could still be maintained.

The delay times chosen for the demonstration of the first generation true time delay was 5, 10, 20, and 40 ps; therefore, delays from 0 to 75 picoseconds could be realized with a 5 ps resolution. The waveguide delays then corresponded to 0 to 1.51 cm with the shortest delay being 0.1 cm. The fabricated final structure can be seen in Figure 44 where red laser light was used for fiber alignment during signal coupling into the device.
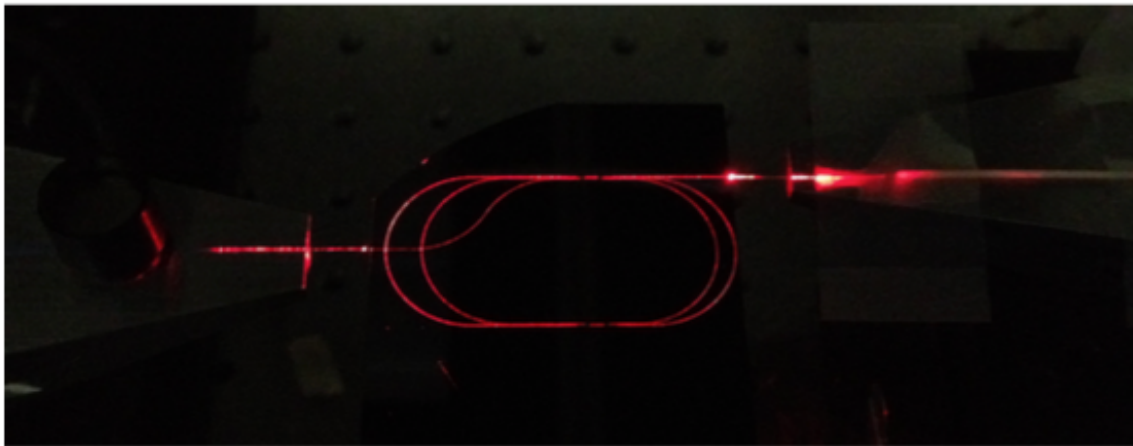
Figure 44: Fabricated true time delay with red laser coupled into the waveguide, which is used for a coarse fiber alignment during fiber coupling.

Optical Switches

The first measurement to be done was to determine the switch performance and bias point based on an identical 2×2 switch test structure. The switch is based on the thermo-optic effect via a Mach-Zehnder interferometer and the heaters were 1.55 mm long. A 1550 nm laser was coupled into the top input of the switch and a broadband InGaAs detector at each output measured the switch response as a function of switch bias. The input polarization was optimized for maximum output power via a polarization controller. A schematic of the thermo-optic switch can be seen in Figure 45 below where the coupling waveguide and the cross and through output defined here are labeled.
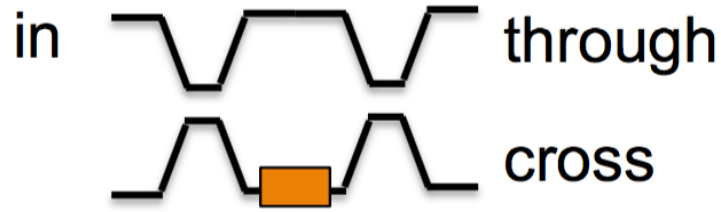
Figure 45: Thermo-optic switch (MZI).

Figure 46 (Left) shows the measured response for both outputs as a single MZI arm is biased. As can be seen from the plot, the unbiased output is which should be in the cross state, is actually in the through state. As current is applied to the NiCr heating element, the index of refraction is changed sufficiently to cause a π-phase shift allowing the output to cycle.
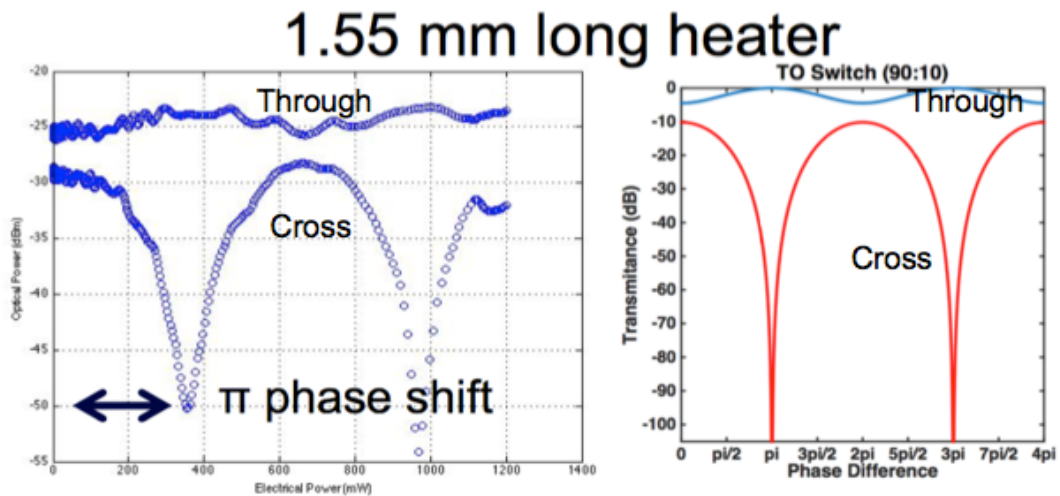
Figure 46: (Left) Measured switch performance on the first generation of OTTD. (Right) Simulated switch performance when the MZI coupler is 90:10 instead of 50:50.

The asymmetric isolation is a direct result of the unbalanced 3-dB couplers [13]. Because the coupler is not 50:50, the through state is never fully off and is thus explained below. For input into port 1, the power output can be described by the equations below which can be derived from the MZI T-matrix from the building block chapter:

70

$$T_{13} = 1 - 2\alpha(1 - \alpha)(1 + cos\theta) \; [through \; path]$$

$$T_{14} = 2\alpha(1 - \alpha)(1 + cos\theta)[cross \; path]$$

where T_{13} and T_{14} are the switch power outputs at ports 3 and 4 for input to port 1, α is the directional couplers power-coupling ratio, and θ is the induced phase shift. As can be seen from the equations, when the switch is in the cross state at $\theta = 0$ (no bias), the transmission for the through path can only reach 0 whenever the coupling ratio is exactly 50%. On the other hand, when the switch is in the through state at $\theta = \pi$, the transmittance of the cross path always reaches 0 no matter what the value of α is. As a conclusion, fabrication variations that cause the coupling ratio to be other than 3dB will always affect the extinction ratio of the through path alone. Figure 46 (Right) shows the transmission of a simulated switch where the MZI coupler is replaced with a 90:10 coupler. The simulated transmission closely matches the measured data and therefore suggests an unbalanced coupler close to 90:10 and thus, a coupling length and coupling gap adjustment for the second generation of OTTD will be required.

Given the thermo-optics properties of glass the switch speed was expected to be in the order of a few milliseconds [13]. The switch speed was then measured according to the measurement setup provide below (Figure 47).
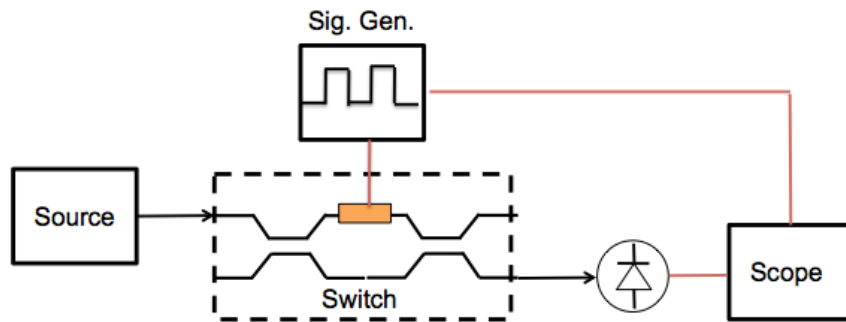
Figure 47: Switch speed measurement setup.

A CW laser source at 1550nm was coupled into the top arm of the switch and the output was measured at the cross port. The switch was driven with a 20 Vp-p (amplifier required) square wave and a photodetector was used to convert the optical into an electrical signal from the switch output so that an oscilloscope could be used to monitor the waveform. Figure 48 shows the results from the measurements at four different driving 'speeds': 100 Hz, 500 Hz, 1 kHz, and 2 kHz. The plot shows the original driving signal in a light blue trace while the switch output is shown as the purple trace. From the plots the switch speed was estimated at 1.5 kHz (<1 ms), thus being sufficient for most applications.
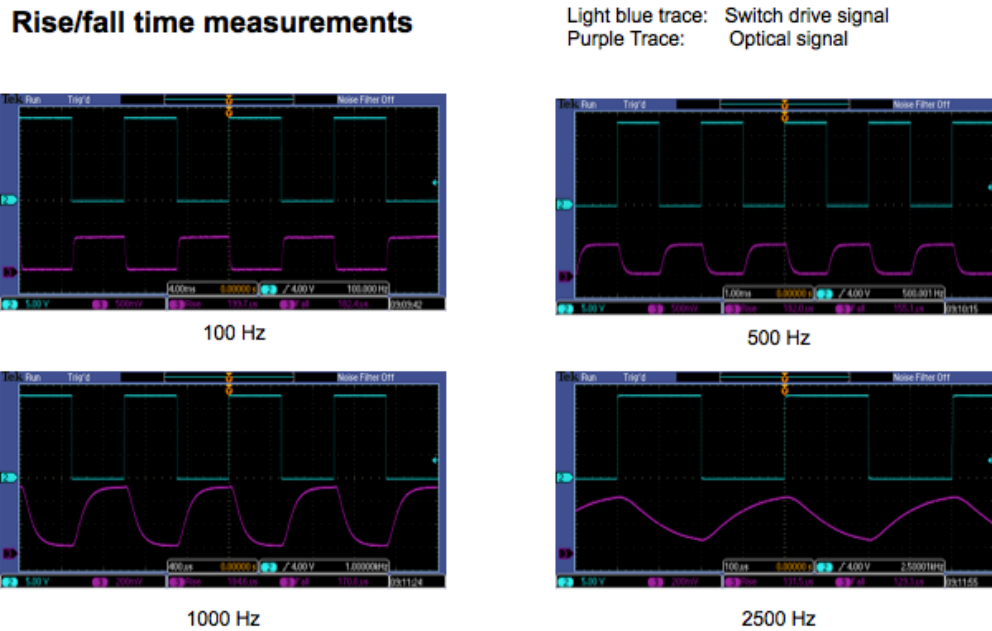
Figure 48: Rise/fall time measurements from the cross port of gen1 MZIs. From top left moving clockwise the time scales are as following: 4.0 ms, 1.0 ms, 400 μs, and 100 μs; where the blue signal are the switching electrical signal and the blue signal is the optical signal

Delay Measurements

To measure the ability of the device to select each individual delay states, a 10 GHz mode-locked laser (MLL) was used as the input source. Because each pulse is spaced by 100 picoseconds and the maximum device delay is 75 ps, all of the delay happens between two

pulses of the MLL making it easier to keep track of the delays on an oscilloscope. The schematic of the delay measurement setup is displayed below in Figure 49.
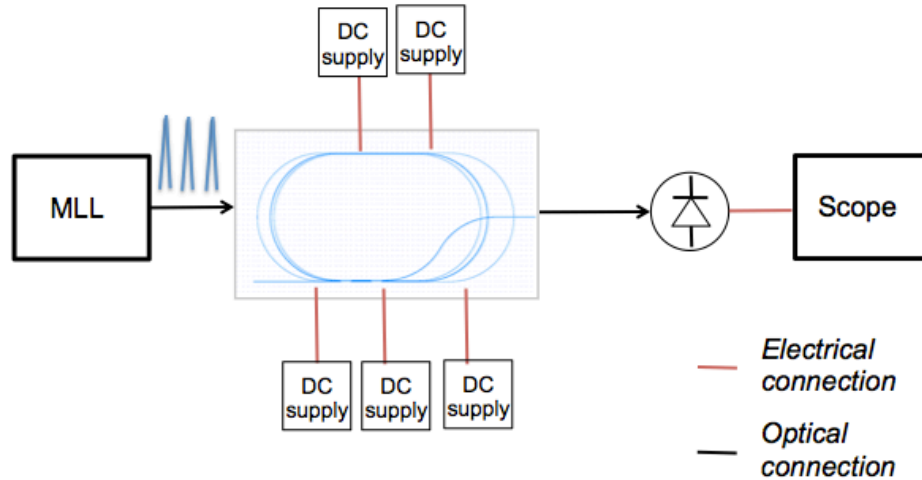
Figure 49: Delay measurement setup.

A total of 5 individual DC power supplies were used to control each individual switch on the OTTD. The first measurement was then the propagation of the MLL through the OTTD chip with all of the switches under zero bias ("OFF" – cross state), which would represent the reference line where the pulse would bypass all of the delays. Because the MZI couplers are not exactly 3dB as presented in the previous section, the through state can thus never be truly turned off. Therefore in this OFF state the pulse is split between the through and the cross path. As a conclusion, multiple pulses are created as the original pulse is split and delayed through both arms of each stage. Figure 50 displays the MLL pulse transmission through the PLC when all of the switches are off, thus showing the pulse splitting. Multiple pulses show the multiple paths, where in reality the detector should only see single pulses at 100 psec.
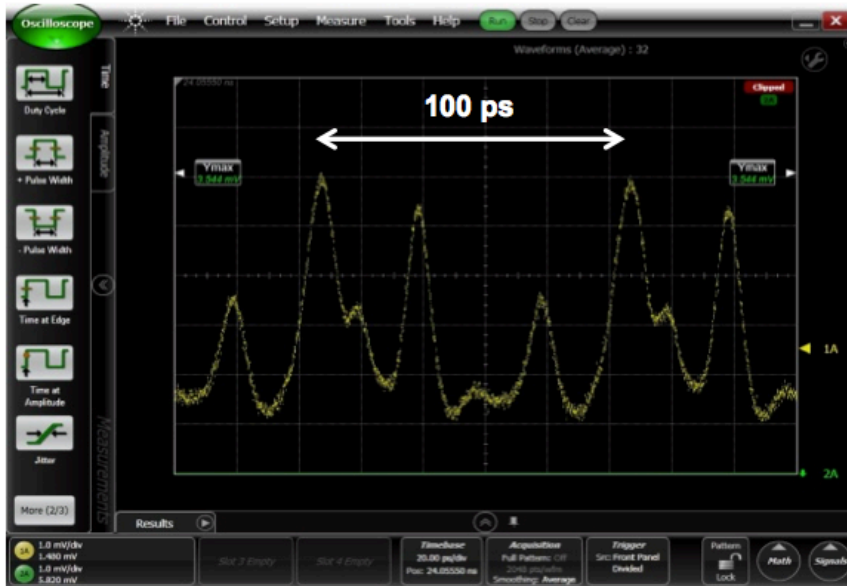
Figure 50: 100 ps MLL transmission through the OTTD where all of the switches are OFF displaying multiple pulses between 100 ps, which is a direct result of the unbalanced MZI switch.

As a result of the multiple pulses creation, the delay measurements of all the states cannot be properly evaluated. Since the switch can only provide a high extinction ratio for the through states only a few bit states can be measured, ideally the bits where the number of through transitions are minimized. The state where all of the switches are ON was then used as the reference pulse. The result of the measurement is then shown in Figure 51, with 5 different delay states clearly selected by the integrated device. The measured delays were then: 76, 38, 17, 5, and 0 ps. Although not all of the delay states were demonstrated, the first generation of OTTD established a proof of principle and provided information for the design of the second generation of OTTD.

Delay Pulses: Normalized Amplitudes

Switch OFF	Delay psec
1	76
5	38
2	17
4	5
3	0 (Ref)

Switch "OFF" means
no bias applied.

Legend: REF MLL Pulses, Switch 1 OFF, Switch 5 OFF, Switch 2 OFF, Switch 4 OFF, Switch 3 OFF
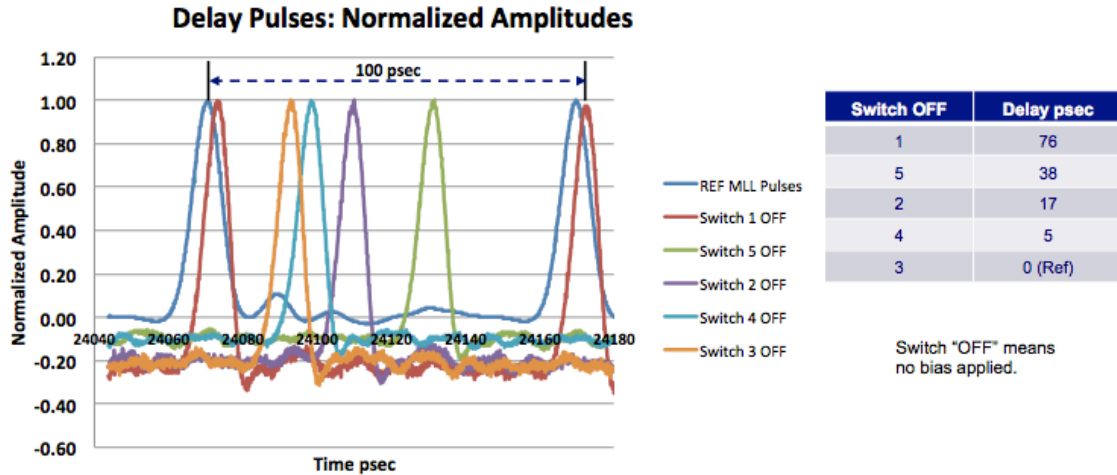
Figure 51: Measurement of 5 different (out of 16 states) delays states of the first generation of integrated optical true time delay (OTTD).

4.4.3 TTD: Generation 2

In the second generation of devices, we present the fabrication of the longest fully integrated 4-bit true time delay on the ultra-low-loss planar Si_3N_4/SiO_2 platform with delays up to 12.35 ns.

Upon completion of the full characterization of the first generation of integrated optical true time delay, a new generation could then be fully designed with improvements based upon the measured results. With the concept established, the two major improvements from gen1 to gen2 were then the proper design of the MZI switch so that all of the 16 delays could be measured individually as well as much longer integrated delays to highlight the ultra low loss of the waveguide platform. The waveguide geometry and platform remained the same with a waveguide core of 60 nm and waveguide width of 7 um on all of the delays and 5.5 um on all of the couplers. The wider core geometry allows for lower propagation loss and a tighter bend radius on the spiral delay and the 5.5 um core width on all the couplers guarantees a single mode operation. A long, approximately 1000um, adiabatic transition was

75

used to change between waveguide core so that only the fundamental mode is excited at a low loss cost per transition.

The 3 dB coupler designed on the first generation had a 3 um coupling gap and a coupling length of 1100 um, based on the switch performance and simulations the second generation of switches had a 3 dB coupler design of a 2 um coupling gap and 825 um coupling length.
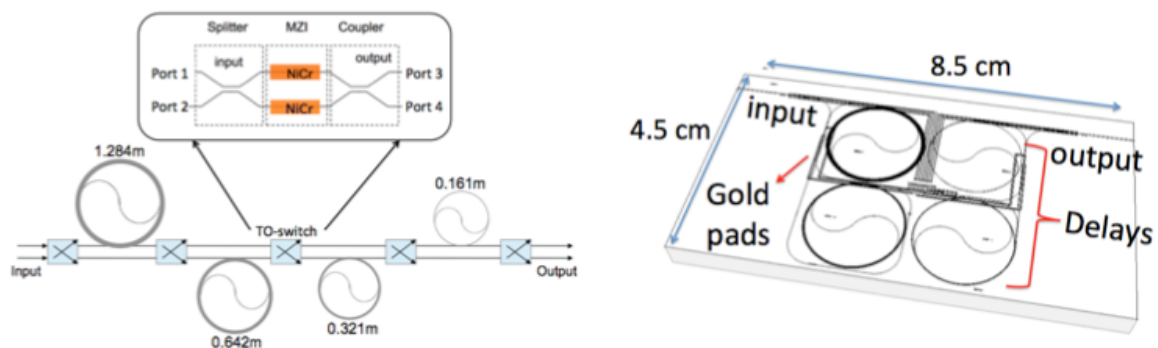
Figure 52: (Left) Schematic of the unpacked tunable delay with the respective delay length for each stage. Inset: Thermo-optic switch schematic. (Right) Actual mask layout of the device displaying the position of each packed delay elements. The diced out device has a dimension of 4.5 cm x 8.5 cm.

The second-generation 4-bit tunable delay consists of four delay elements and five thermo-optic switches (TO-switches) as before, and was designed according to the schematic shown in Figure 52(Left). The TO-switches were also based on Mach-Zehnder interferometers, as seen in the inset of Figure 52 (left). Nickel Chrome (NiCr) was used as the heating element due to its high resistance. The device was physically laid out according to the mask layout as shown in Figure 52 (right) where each delay is routed to its appropriate switch accordingly, and was designed to have lengths of 1.284 m, 0.642 m, 0.321 m, and 0.161 m, where each delay is half of the previous delay, i.e. τ, $\tau/2$, $\tau/4$, $\tau/8$. A total of 16 different delays may be selected by choosing from an individual delay or a combination of delay elements. The

device therefore provides nominal delays from 0 to 12.00 ns, with respect to the minimum path length, for a maximum total of 2.407 meters in propagation length and a simulated group index of 1.49. Because the delays implemented in this case are much longer, the Archimedean spiral provides the most efficient way to pack all the of the delays together; Figure 53 shows the image of the final device fabricate with red light coupled in, which is used for finding waveguide breaks and aid in fiber alignment.
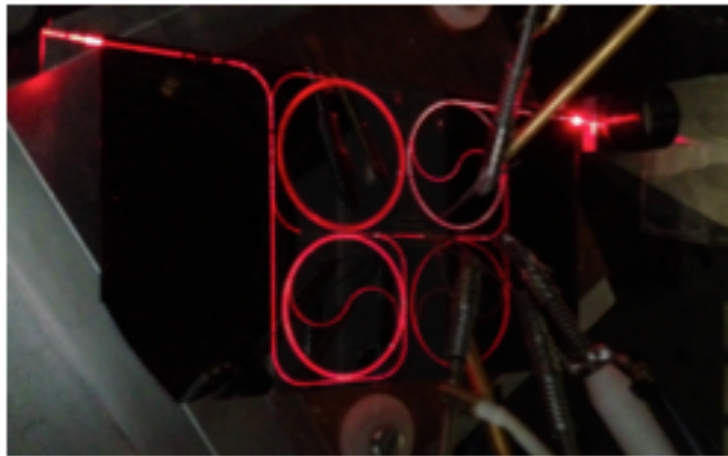
Figure 53: Fabricated 4-bit true time delay with red laser light coupled into the input waveguide.

Optical Switches

The switch characterization done followed the same procedures established in the previous sections. The new switch design showed improved performance over the first generation with the switch output as a function of bias presented below (Figure 54). The measured extinction ratio on the cross path was greater than 30 dB while on the through path was only 6 dB, while still an improvement over the previous generation the switch/coupler design is not yet optimal.
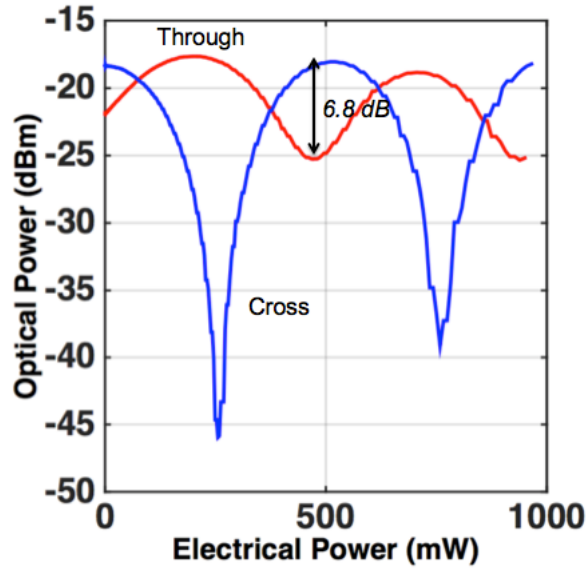
Figure 54: Switch output for the cross and through path as a function of applied bias operated at room temperature (25 °C).

One method to improve the performance of the switch is by heating the entire device as to change the coupling constant, and essentially the coupling length to a value that corresponds to the length on the chip, via the thermo-optic effect can compensate for these fabrication variances. In order to find the optimal operating temperature for the highest switch isolation, a thermo-optic cooler was used to maintain the entire chip at a desired temperature. The temperature was varied between 22 and 38 °C, while measuring the switch isolation at each point (Figure 55).
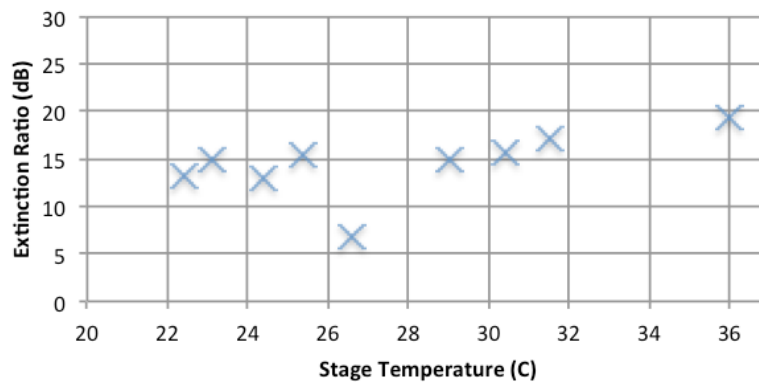
Figure 55: Extinction ratio as a function of operating temperature.

78

At room temperature, the switch had an isolation of 6.8 dB as previously mentioned, while the best result was achieved at an operating temperature of 36 °C with a switch isolation of 19.3 dB, as seen in Figure 56. The turn-on power was also measured to be 260 mW, which corresponds to an applied average voltage of 16.0 V.
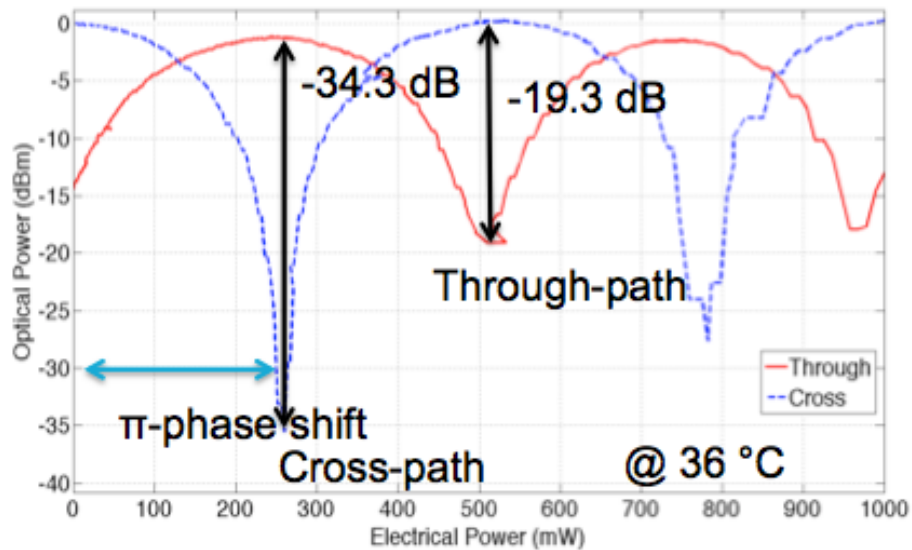
Figure 56: Optimal switch performance operating at a temperature of 36° C.

The device was then operated under a TEC with the temperature set to 36° C. The performance of all 5 switches was measure and showed identical performance to the one as shown in Figure 56. A slight decrease in ER is seen at higher operation power, which is indicative of thermal crosstalk since the MZI arms are only 100 um apart. Although thermal crosstalk is seen, the device only requires a π phase shift for proper operation and therefore at that region no thermal crosstalk can be seen. The power consumption of each switch is shown in Figure 57. The switches also showed similar speed measurements as the 1st generation with a speed of 1.5 kHz.

Switch #	I (mA)	P (mW)
1	15.20	260.1
2	15.72	260.0
3	18.16	260.8
4	16.32	260.1
5	16.84	260.0

Figure 57: Switch power consumption of all of the switches used on the second generation of OTTD operating at optimal temperature.

Delay Measurements

Because the switch shows an excellent extinction ration all of the 16 delay stages can be properly selected by biasing the switches accordingly. The total optical loss of the device was then measured at each of the 16 separate states. Each switch was biased accordingly and 0 dBm of optical power from a tunable laser at 1550 nm wavelength was coupled into the device via a cleaved single mode fiber. The optical output was then collected by another cleaved single mode fiber and detected using a broadband InGaAs detector. Figure 58 displays the measured optical loss from fiber to fiber for all 16-bit states, where State 1 represents the shortest delay in which the light travels through no delay element and State 16 is the longest delay state where the light travels through all 4 of the delay elements.
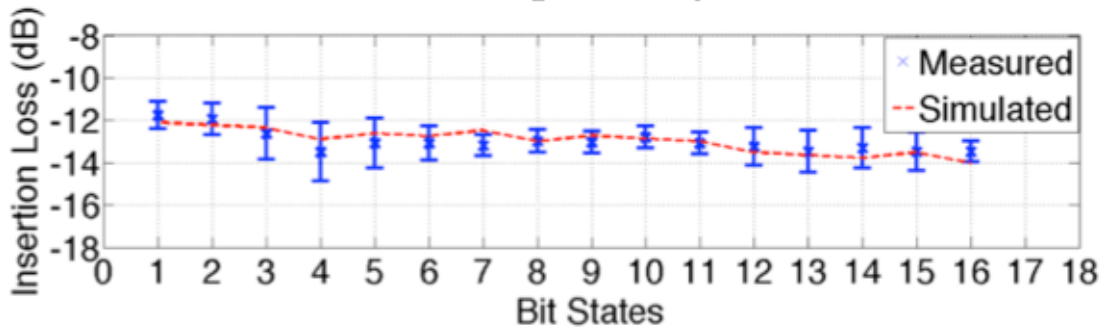
Figure 58: Total optical loss from fiber to fiber for all 16 bit states, where state 1 is the shortest delay and 16 the longest including simulated results.

All the data have been normalized to the back-to-back measurement where the chip is bypassed and the error bars are based on the standard deviation of ten measurements, where the variation between each measurement is caused by temperature variation as the temperature profile changes from state to state while the thermo-electric cooler (TEC) tries to maintain a constant temperature. As can be seen from Figure 5, the data display some deviation from a linear relationship from state to state, which is a result of the imbalanced switch causing the cross state to have higher loss, as shown in Fig. 3. State 4 is the only state where all the switches are set to the cross state; therefore, as can be seen in the plot, it is the state that deviates the most. The dashed line in Figure 5 is based on simulated results of 0.8 dB for loss, 1.5 dB per facet of coupling loss, and losses for the cross and through states of the switches of 1.9 and 1.7 dB, respectively.

The measurement displays a small deviation in power from state to state, which is indicative of the low-loss waveguide platform. An insertion loss (fiber-to-fiber) of 11.8 ± 0.6 dB was measured for the shortest delay and 13.5 ± 0.5 dB for the longest delay (12.35 ns). The difference between the shortest and longest delay is 1.7 dB, which is equivalent to propagation losses of 0.7 dB/m.

The next step was then to verify that the extinction ratio of each switch was indeed sufficient for the proper operation of the device. The same MLL as the previous section was then used and coupled into the device while no bias was applied. By performing a visual inspection of Figure 59, which shows the device output through a sampling scope, very little evidence to switch crosstalk is seen as only the 100 ps pulses can be seen on the plot.
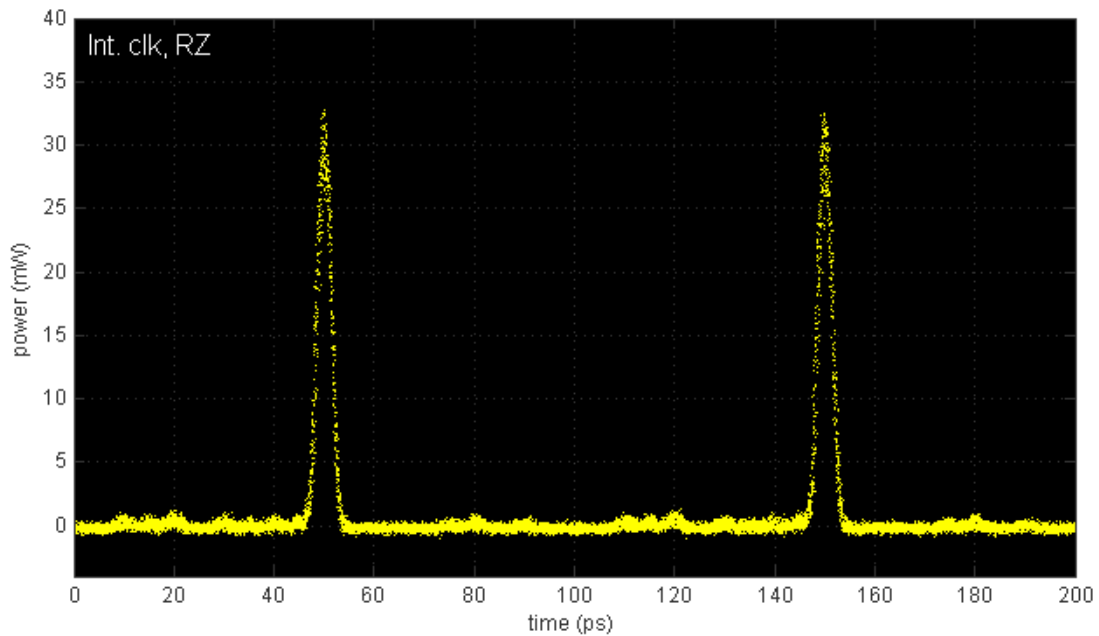
Figure 59: 100 ps pulses propagating through unbiased OTTD chip showing little sign of switch crosstalk.

Lastly, the delay measurements were collected using the experimental set-up shown in Figure 60. A mode-locked laser (MLL) centered at 1557 nm was utilized to generate a train of 2-picosecond pulses at a 10 GHz repetition rate. A pulse-carving Mach-Zehnder modulator (MZM) was used to reduce the repetition rate by a factor of 256, which was long enough to accommodate the longest delay of 12.00 ns. The polarization state was again controlled through a 3-paddle polarization controller and the light injected into the device in a transverse-electric (TE) state via a cleaved single-mode fiber. The device output signal was then collected through another cleaved single mode fiber, amplified with an Erbium-doped fiber amplifier (EDFA) at constant current, and finally sent to a sampling scope for characterization.
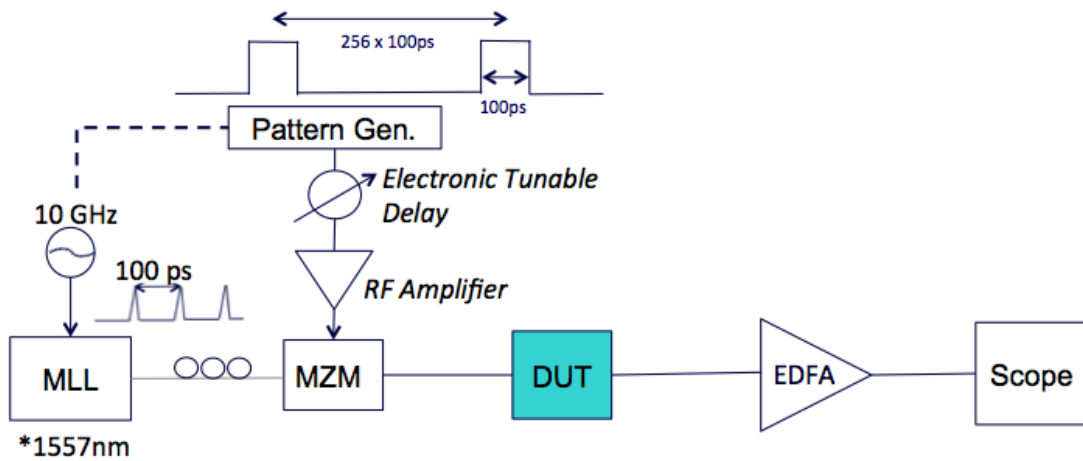
Figure 60: Experimental set-up used to characterize delay configurations.

Figure 61 shows the optical output for the tunable delay. The plot displays the delays acquired for all 16 states of the 4-bit tunable delay with respect to the first state. The total temporal delay was measured to be 12.35 ns with a 0.85ns resolution, corresponding to a small deviation from the simulated group index due to a miscalculated waveguide effective index. If the error is taken into consideration and the proper group index is used, the measured delay closely matches the simulated delay with very little deviation from design.
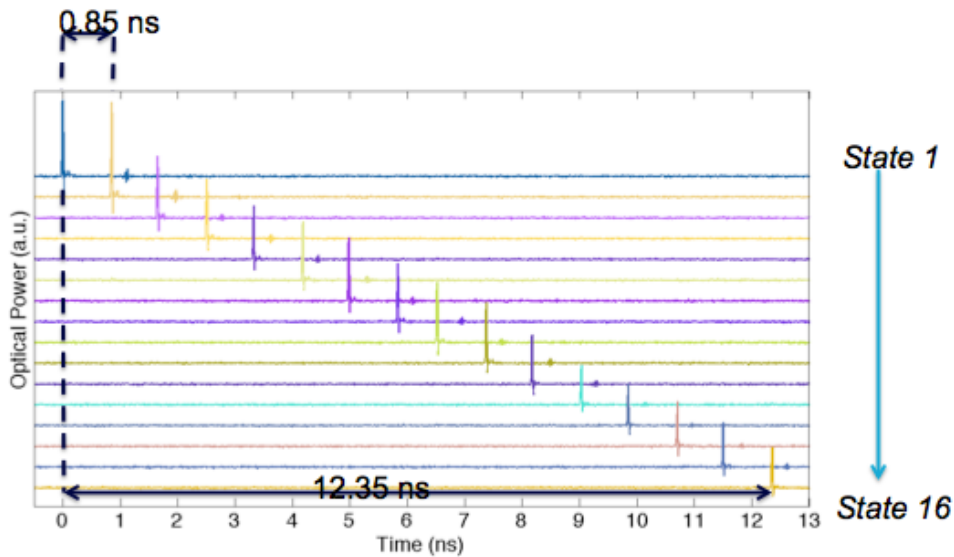
Figure 61: Optical output of the 4-bit tunable delay for all possible delay settings.

4.5 Conclusions

We demonstrated the realization of the longest fully integrated 4-bit tunable delay on an ultra-low-loss Si3N4 planar waveguide platform consisting of 4 delay elements and 5 thermo-optic switches. The thermo-optic switches were measured to have 19.3 dB of isolation and 260 mW of power consumption. Delays up to 12.35 ns (2.407 meters) with temporal resolution of 0.85 ns were demonstrated. Waveguide TE losses were measured to be 1.01 ± 0.06 dB/m at 1550 nm and 0.57 ± 0.08 dB/m at 1591 nm.

The device presented here is also easily scalable for even longer delay lines and higher bit count delays given the low propagation loss of the platform. For the same platform we have measured coupling losses of 0.91 dB and TE losses lower than 0.1 dB/m with 50 nm thick cores and 6.5 μm wide waveguides, while maintaining the critical bend radius below 5 mm [14]. In this work, a 60 nm core and a minimum bend radius of 5 mm was used; consequently, in the future, much longer delays may be fabricated at smaller footprints.

4.6 References

[1]   I. Frigyes, and A. J. Seeds, "Optically generated TTD in phase array antenna," IEEE Trans. Microwave Theory & Technology, vol. 43, 2378-2386, 1995.

[2]   E. Ackerman et al., "Integrated 6-bit photonic true-time-delay unit for lightweight 3-6 GHz radar beamformer," Microwave Symp. Digest, 1992.

[3]   J. J. Lee et al., "Photonic wideband array antennas," Antennas and Propagation, IEEE, vol.43, no.9, 966-982, 1995

[4]   X. Wang, B. Howley, M. Chen, P. Basile, and R. Chen, "Fully-integrated 4-bit true time delay module using polymer optical switches and waveguide delay lines," in Integrated Photonics Research and Applications/Nanophotonics, 2006

[5] D. S. Sumida et al., "Rapidly reconfigurable 8-bit chip-scale true-time-delay module for high-bandwidth-preserving, multi-aperture, free-space laser-communication transmitter," CLEO, 2005.

[6] L. Zhuang et al., "Single-chip ring resonator-based 1x8 optical beam forming network in CMOS-compatible waveguide technology," Photonics Technology Letters, IEEE, vol. 19, no. 15, 1130-1132, 2007.

[7] S. T. Chu et al., "High index contrast photonics platform," Proc. SPIE, vol 6014, 2005.

[8] Alan J. Fenn, Donald H. Temme, William P. Delaney, and William E. Courtney, "The Development of Phased-Array Radar Technology," Lincoln laboratory journal, vol.12, no.2, 2000

[9] "A brief history of the sea-based x-band radar-1," Department of defense, Missile Defense Agency, May 2008.

[10] Jared F. Bauters, Michael L. Davenport, Martijn J. R. Heck, J. K. Doylend, Arnold Chen, Alexander W. Fang, and John E. Bowers, "Silicon on ultra-low-loss waveguide photonic integration platform," Opt. Express 21, 544-555 (2013)

[11] David K. Cheng, "Antennas and radiating systems," in Field and wave electromagnetics, 2nd ed. Addison-Wesley Pub. Comp. 1989.

[12] J. Bauters et al., "Planar waveguides with less than 0.1 dB/m propagation loss fabricated with wafer bonding," Optics Express, vol. 19, no.24, 24090-24101, 2011.

[13] H. Takahashi, "Planar lightwave circuit devices for optical communication: present and future," in Proc. SPIE, vol. 5246, 2003.

[14] Bauters et al., "Ultra-low-loss high-aspect-ratio Si3N4 waveguides," Optics Express, vol. 19, no. 4, 3163-3174, 2011.

Chapter 5

Tunable Dispersion Compensating Filter

5.1 Introduction

Chromatic dispersion is an undesired fiber characteristic resulting directly from the fact that group delay changes with wavelength. Since a pure single tone signal does not exist, as a pulse propagates along a fiber different wavelength components will travel at different velocities thus resulting in pulse broadening and limiting the data rate and transmission distance. The dispersion tolerance of a transmission system is inversely proportional to the bit rate square; therefore, doubling the bit rate deteriorates the tolerance 4x making it a serious problem for high-speed communications. As an example, a 40 Gb/s system on a single mode fiber has a dispersion tolerance length of 4 km!

Numerous solutions have been found for dispersion compensation, where the two most common are dispersion-compensating fiber (DCF) and electronic dispersion compensator via DSP. Fiber and free space optic based compensators typically have high loss and are expensive. Today's strongest alternative is DSP-based coherent compensators, which can be power "hungry" and cannot operate under direct-detection. Solutions with lower prices and power dissipation for short and mid-distance communication where dispersion might not be as severe are necessary.

Optical tunable filters can be of great benefit to dispersion compensation by providing a low-loss and compact approach with low power consumption that is independent of bit rate.

Optical filters can also compensate phase and amplitude distortion making it an excellent competitor to the previous two technologies. If properly designed, optical filters will have a periodic frequency response that allows for simultaneous compensation of multiple WDM channels using a single device. The tunability of such devices provides a great way to dynamically compensate for residual chromatic dispersion which can fluctuate due to temperature changes, path changes in reconfigurable optical networks, as well as end of life device and system characteristics.

Integrated dispersion equalizers have been demonstrated in several platforms including silica planar lightwave circuits [1], [2], [3], and silicon photonics [4][5]. Although successfully demonstrated in those platforms, achieving high order filters with reasonable footprints and device loss becomes impractical. Silica waveguides have the required propagation losses to make low insertion loss devices but lack the necessary bend radius to make compact devices. Low loss silica devices typically have a minimum bend radius greater than 5 mm [6]. On the other hand, silicon photonics devices have small bend radius due to high index contrast, but waveguide propagation losses limit devices to shorter delays and low delay counts.

In this dissertation we present the integration of a dispersion-compensating filter on a platform capable of providing state-of-the-art waveguide losses at bend radius 10x smaller than silica waveguides. This platform allows for the integration of lattice filter with large stage number at a small footprint otherwise not feasible on any other integration platform simultaneously. Thus allowing for the mitigation of OSNR penalty of the link for a whole bank of WDM at once due to the filter design. Here we demonstrate a 10-stage optical lattice filter with periodic frequency response capable of compensating +/- 500 ps/nm of dispersion for multiple WDM channels simultaneously. The device is integrated on a high-aspect ratio

Si3N4 waveguide core, where the core geometry determines the overall loss and bending capabilities [7].

5.2 Filter Design

The tunable lattice filter for dispersion equalization is based on a generalized optical finite impulse response (FIR) filter, which is the same filter architecture also demonstrated by Doerr et al. and Geheler et. al. [8], [9]. The schematic depicting device architecture for the fabricated programmable 10-stage filter is shown in Figure 62 below. Although a conventional lattice filter provides a very low-loss passband, every coupler and phase must be tuned in order to achieve an arbitrary transfer function, which becomes impractical when dealing with high order filters. The generalized filter presented here allows for a "single-knob" dispersion control. Although this design does not allow for arbitrary transfer function realization, the filter is optimized for continuous dispersion tuning between its maximum and minimum setting while still maintaining the low-loss passband characteristic of a lattice filter.
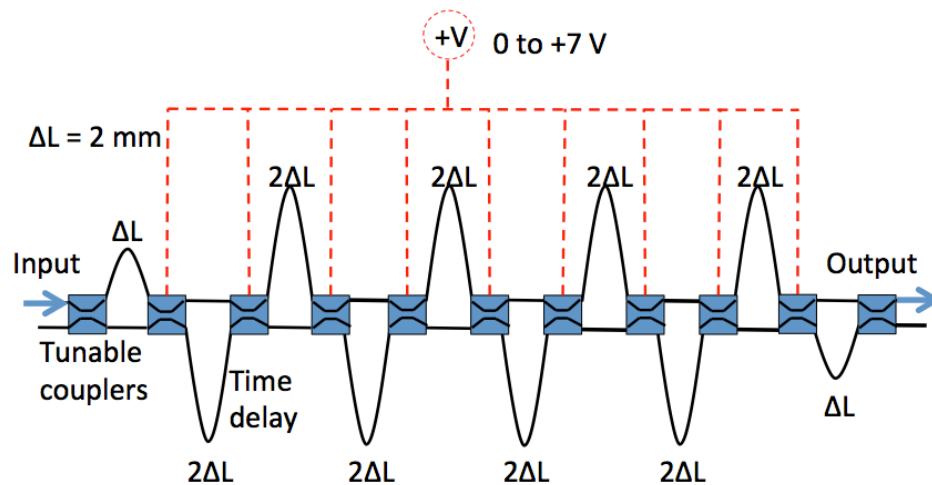
Figure 62. Schematic of the 10-stage dispersion compensating filter architecture with single knob dispersion control.

The filter is composed of cascaded alternating symmetric and asymmetric Mach-Zehnder interferometers (MZI). The symmetric MZIs are designed to function as tunable couplers for guiding the path on which the signal will take, while the asymmetric MZIs will mostly function as the dispersive element and set the filter order. When the couplers are set to 100/0 (bar state) the entire device will function as a large symmetric interferometer with flat transmission and zero dispersion. As the coupling ratio starts to deviate from 100/0, the outer delays act as a mux/demux and all the middle delays act as a long wavelength dependent delay due to the alternating pattern. The maximum delay is achieved when the couplers are at a 50/50 splitting ratio.

The time delays are chosen to be integer multiple of the unit delay, thus making the filter discrete in the time domain. By making the filter discrete in the time domain, this assures the filter has periodicity in the frequency domain, which can then be used to simultaneously compensate multiple WDM channels. The filter frequency response can then be simulated though the use of T-matrix formalism, where the main building block is the MZI. The transmission matrix relates the inputs/outputs at a given port to the inputs/outputs at the other, which will allow representation of the device network through a simple matrix multiplication. A single stage MZI consists of two directional couplers with power coupling κ and delay lines of length L1 and L2 can be represented as such below.

$$\begin{bmatrix} E_{1\,out} \\ E_{2\,out} \end{bmatrix} = \begin{bmatrix} T_{11} & T_{12} \\ T_{21} & T_{22} \end{bmatrix} \cdot \begin{bmatrix} E_{1\,in} \\ E_{2\,in} \end{bmatrix} = \boldsymbol{T} \cdot \begin{bmatrix} E_{1\,in} \\ E_{2\,in} \end{bmatrix}$$

Where T is the total transfer matrix for the MZI and can be found by the multiplication of the first coupler, delay, and second coupler individual transfer matrices [10].

$$\boldsymbol{T} = \boldsymbol{T}_{coupler} \cdot \boldsymbol{T}_{delay} \cdot \boldsymbol{T}_{coupler}$$

89

$$T = \begin{bmatrix} \sqrt{1-\kappa} & -j\sqrt{\kappa} \\ -j\sqrt{\kappa} & \sqrt{1-\kappa} \end{bmatrix} \cdot \begin{bmatrix} e^{-jKnL_1} & 0 \\ 0 & e^{-jKnL_2} \end{bmatrix} \cdot \begin{bmatrix} \sqrt{1-\kappa} & -j\sqrt{\kappa} \\ -j\sqrt{\kappa} & \sqrt{1-\kappa} \end{bmatrix}$$

The k term is the power coupling coefficient for the coupler, L1 and L2 correspond to the MZI delays on each arm, and K is the wave vector equivalent to $2\pi/\lambda$, where λ is the wavelength. With the building block defined cascading the equivalent blocks accordingly can then simulate the entire filter. From the definition in equation 1, the T11 matrix element corresponds to the filter transmission from port 1 to port 3 when there is no input in port 2 and so forth. Therefore, the transmission and phase for the filter can be directly extracted from the total T-matrix as described below, and the same can be done to all the matrix elements.

$$Transmission = Tr = \ |T_{11}|^2$$

$$Phase = \Theta = \ arg\{T_{11}\}$$

The group delay and dispersion can then be calculated as following:

$$\tau = -\frac{d\Theta}{d\nu}$$

$$D = \frac{d\tau}{d\nu}$$

Using the T-matrix approach described above, the filters response was simulated for different numbers of stages and unit delay length. Fig. 2 shows the calculated dispersion amount for the different filter designs. As shown, dispersion is proportional to ΔL2 for a set number of stages and therefore it is desirable to make ΔL as large as possible. However, the filter passband and FSR scale with 1/ ΔL and a tradeoff must be considered. Then for a given delay length, the only way to increase dispersion without compromising bandwidth and FSR is by increasing the number of filter stages, which requires a platform with low propagation

loss. By using the design curves below, a unit delay length of 2mm was chosen corresponding to an FSR of 100 GHz. As a result, in order to achieve 500 ps/nm of compensation a 10-stage filter is required.
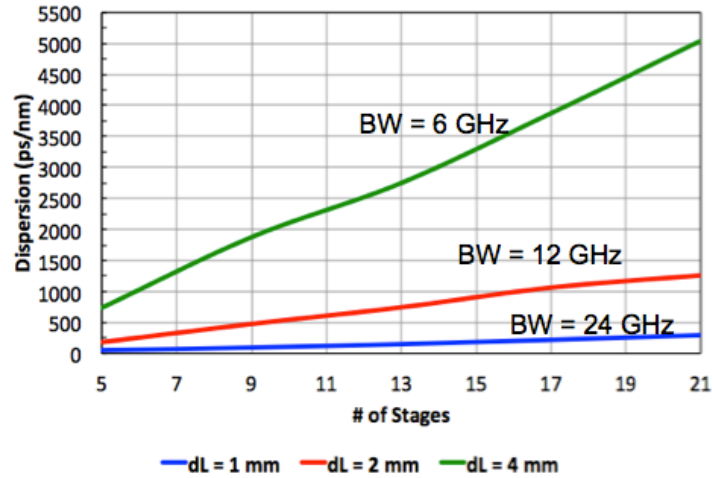
Figure 63. Simulated filter dispersion for the generalized lattice filter as a function of the number of stages for 3 different unit delay length. The associated bandwidth (BW) is shown above each curve.

5.3 Waveguide Design and Fabrication

The tunable dispersion equalizer was fabricated on a high-aspect ratio low-loss silicon nitride waveguide platform as described in [7]. Figure 64(Left) shows a schematic of the cross-section of the completed waveguide structure. The device was fabricated on a 4" silicon substrate where 15 μm of thermal oxide served as the waveguide lower cladding. Stoichiometric low-pressure chemical vapor deposition (LPCVD) Si3N4 was used as the waveguide core and an additional 3 μm of sputtered SiO2 was deposited as an upper cladding. The device was patterned via 248-nm stepper lithography and etched through reactive ion etching (RIE). The final waveguide structure was then annealed at 1050 °C for 7 hours under N2 ambient in order to drive out any residual hydrogen impurities from the

91

Si3N4 films and/or SiO2 deposition. The final fabrication step included depositing Nickel/Chrome and Titanium/Gold, which served as phase turners via thermo-optic effect and electrical contact, respectively. The metal layers were deposited via e-beam evaporation and patterned through a liftoff process.
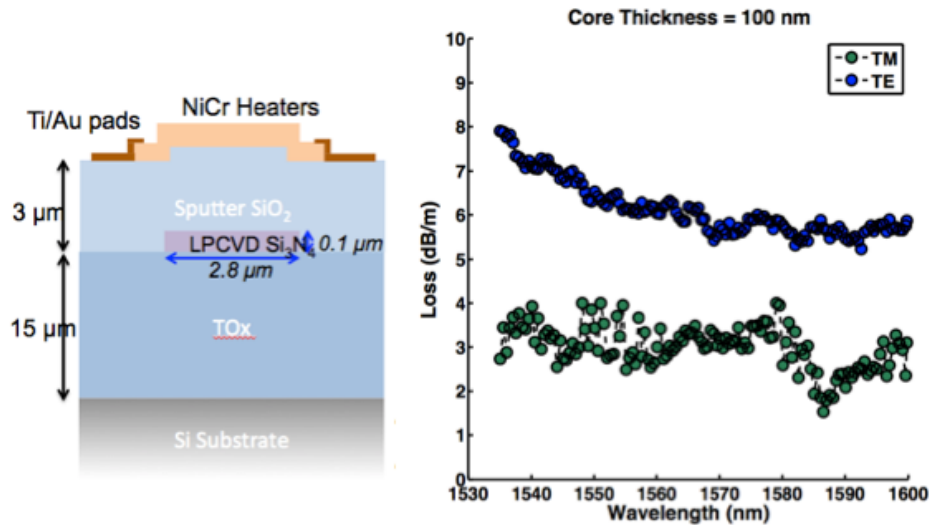
Figure 64. (Left) Schematic of the fabricated waveguide cross-section. (Right)

The waveguide core dimension was 2.8 μm in width by 100 nm in thickness. The core geometry was designed to be single mode at 1550 nm and to provide the aspect ratio required to minimize the optical mode overlap with the sidewall roughness, thus decreasing the propagation loss to the low-loss regime. The core thickness of 100 nm was chosen to allow for tight bend radius (500 μm), which is crucial for the smaller footprint, while still maintaining the necessary low propagation loss. Figure 64 (Right) shows the measured TE and TM propagation losses as a function of wavelength over the range from 1530 nm to 1600 nm. The measurement was performed via optical frequency domain reflectometry (OFDR) on a separate 1 meter spiraled waveguide test structure fabricated on the same wafer. The lowest measured waveguide losses were 0.058 dB/cm and 0.018 dB/cm for TE and TM,

respectively. Because of the high-aspect ratio of the waveguide geometry, the confinement of

the fundamental TM mode is much lower than that of the fundamental TE mode, which in

turn results in the measured lower losses. Although the measured TM losses are lower than

TE, the minimum bend radius required to keep the bend losses legible are much higher.

Therefore, in order to keep the entire structure footprint small, the device was designed for

TE excitation only. A simulated minimum bend radius of 500 μm was required in order to

keep the bend losses to < 0.001 dB/cm. With the measured propagation losses and the

simulated bend losses, the platform described here provides a vast advantage over its doped

SiO2 core PLC counterpart, which provides similar propagation losses but at a much higher

minimum bend radius of > 5 mm.

5.4 Fabrication and Measurement Results

Figure 65 shows the photo mask layout as well as the actual fabricated device. With the

minimum bend radius of 0.5 mm, the device dimensions were 9.89 mm x 22.5 mm, which is

equivalent to a footprint of only 2.23 cm2. The full characterization of the device is broken

down into geometry results where we verify the platform's performance (presented in the

section above) and then device results, where we look into the filter transmission, group

delay, and dispersion. The filter performance on a full transmission link is also evaluated.
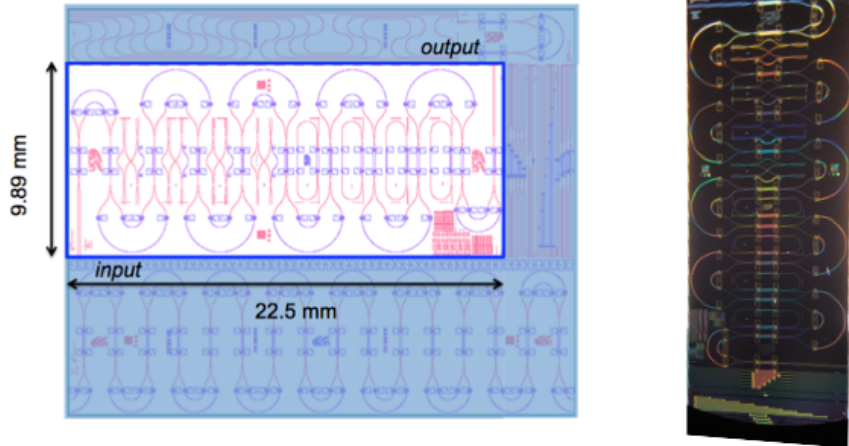
Figure 65. (Left) Mask layout showing the dimensions for the filter (9.89 mm x 22.5 mm) (Right) Optical microscope picture of the final fabricated device.

5.4.1 Filter Measurement Setup

To measure the filter's amplitude response, a CW output from a tunable laser source was sent through a 3-paddle polarization controller and subsequently coupled into the filter via a cleaved fiber. Index matching fluid was used to improve the coupling efficiency and minimize reflections between the fiber and the diced facet. Because the device can only support TE mode at the lower loss regime, the optical power was maximized at the output through the use of the polarization controller. The signal transmitted through the device was collected through another cleaved fiber and detected with a broadband photodetector. The laser output power was set to 0 dBm for all of the transmission measurements.

Group delay was measured through OFDR by using a commercially available reflectometer. Because the OFDR technique measures the backscatter signal, a circulator was placed between the device under test (DUT) and the reflectometer as to measure the S_{21} instead of the S_{11}. The amplitude information of the frequency domain data can provide a measure of the device's insertion loss as a function of wavelength, while the phase information of the frequency domain data is used to calculate group delay and chromatic dispersion. By

94

definition, group delay is defined as the rate of change of the phase as a function of wavelength ($\tau = d\phi/(d\lambda)$), while chromatic dispersion is the rate of change of group delay with respect to wavelength ($D = d\tau/(d\lambda)$). Both metrics can be calculated directly from the phase information of the OFDR measurements.

5.4.2 Filter Periodicity

The periodicity of the filter response is a critical, because it allows for the dispersion compensation of multiple WDM channels through the use of a single device. Therefore, the transmission and group delay response must be periodic throughout the operation of the device. Figure 66 shows the transmission and group delay measurement for a single bias setting. The filter periodicity can be verified in both results and was measured to be as designed at 100 GHz FSR, as set by the unit delay of 2mm. The figure also shows the filter response for a total of 8 channels, thus making it possible to compensate at least 8 channels simultaneously.
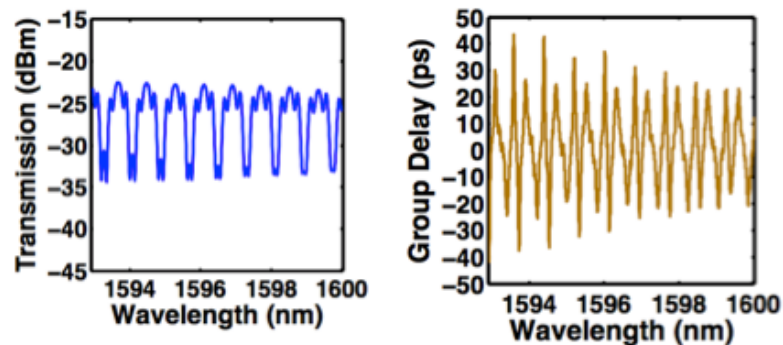
Figure 66. Measured transmission and group delay for a single bias setting.

The next step was to verify that the filter response could be tuned though the use of the thermo-optic effect without any major change to the periodicity and wavelength grid. Fig. 6 below shows the same type of measurements for 4 different biases for the tunable coupler

corresponding to an applied voltage of 0, 2, 3.4, and 5.6 V. As the bias setting changes, the coupling ratio at all the couplers varies simultaneously which in turn will change the filter group delay response. As can be seen from the figure, the filter FSR stayed the same for all the bias settings, but the filter transmission and group delay varied with each setting accordingly.
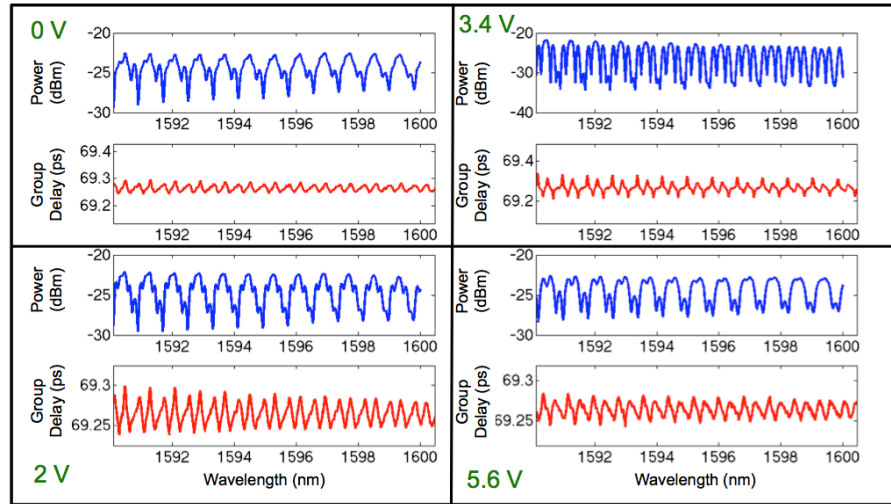
Figure 67. Filter response for various bias setting on the tunable coupler.

5.4.3 Insertion Loss

It is important to note that transmission data in the previous section was not normalized; and therefore, after we consider the measured setup system losses of 2.0 dB and an input power of 0 dBm, the filter was found to have a total insertion loss of 21.8 dB. The total insertion loss deviates from the optimal loss due to the fabrication process and not platform and filter design. The loss components are summarized below, but if properly addressed the filter total insertion loss from fiber to fiber should be < 4 dB. The device's insertion loss can then be broken down into 4 different components that are separately explained in this section: propagation loss, coupling loss, metal absorption loss, and bend loss.

The waveguide propagation loss, as previously stated, was measured to be 0.058 dB/cm. The total propagation length of the device is 20.8 cm; therefore, the waveguide loss contribution to the total insertion loss is only 1.2 dB. The coupling loss was characterized on multiple straight waveguides adjacent to the filter as to minimize the potential of any coupling variation. The coupling loss was measured to be 2.88 ± 0.15 dB/facet, which contributes a total of 5.8 dB to the total insertion loss. Coupling loss on this platform can be further improved through the use of spot-size converter to losses < 1 dB/facet [11]. The third part of the insertion loss corresponded to the metal absorption caused by the heating element being placed too close to the core, 3 μm above the core in this case. To measure the metal absorption, the filter transmission was measured with and without the heaters. Figure 68 shows the filter response with and without metal for a successful measurement of metal absorption of 5.5 dB.
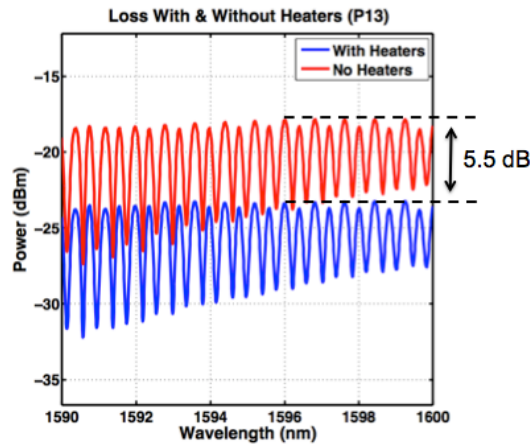
Figure 68. Filter transmission with heaters and no heater for the same filter, corresponding to a metal absorption loss of 5.5 dB.

The remaining 9.3 dB of insertion loss can then be attributed to bend loss and coupler loss. After further investigation, it was realized that no offsets were placed between the transitions of bent to straight waveguides and between the transitions of two bent waveguides of

different direction. The transition mismatch loss was simulated to be 0.04 dB/transition for straight-bend and twice for bend-bend. Although the simulated losses are small, there are a total of 80 straight-straight and 60 s-bends. Therefore, the overall transition bend loss from the simulated values corresponds to 8.6 dB, which almost completely accounts for the remaining insertion loss.

5.4.4 Lattice Filter Tuning and Dispersion Compensation

To analyze the device's ability to compensate dispersion, we then analyze the filter's full response at a single channel. The device is measured at a total of seven different bias points from 0 to 7 Volts with a maximum power dissipation of 723 mW. The filter's group delay response is controlled by adjusting the coupling ratio of the tunable coupler through the thermo-optic effect by applying current to a single arm of the MZI. The heaters were 10 μm wide and 1000 μm in length, and the response was measured and varied from 0/100 to 100/0, a complete switch characterization is shown in [12]. Figure 69 displays the transmission and group delay response for a single channel for all seven different voltage biases.
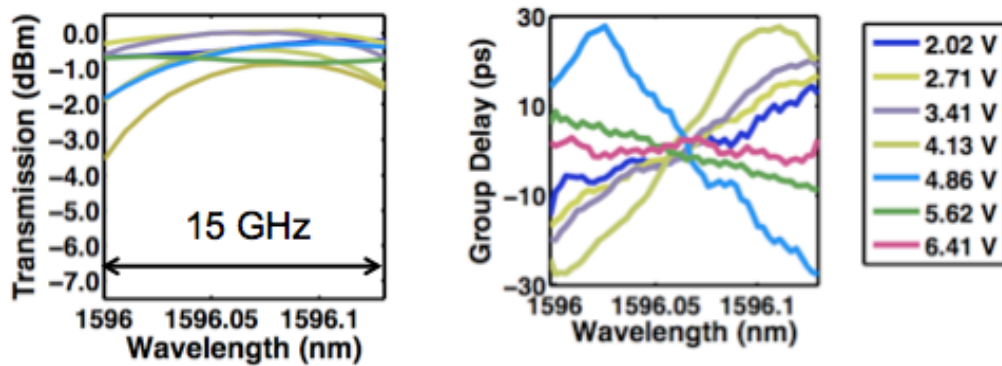
Figure 69. Complete filter characterization for a single passband, showing transmission and group delay results for seven different bias settings.

The transmission plot (left) data is normalized to the lowest loss transmission in order to highlight the difference in transmission between each bias setting. As can be seen from the

plot, the transmission remains above 3 dB for all of the bias settings with a measured "useful" bandwidth of 15 GHz. Figure 69 (right), shows a linear group delay across the transmission bandwidth for all the different biases. Because dispersion is defined as the rate of change of group delay over wavelength, a linear group delay response is equivalent to a constant dispersion. Therefore, dispersion can be determined by finding the slope of the group delay by fitting a straight line through the data. The plot also shows different slope signs for various settings, which correspond to the filter's ability in compensating positive and negative dispersion.

An example of the linear fit in order to extract dispersion is shown in Figure 70 (left). The figure shows a measured dispersion value of 170 ps/nm for that specific setting with a group delay ripple of ± 4 ps. A similar fit can be done for the remaining bias points in order to extract the dispersion value. A summary for all of the measured dispersion as a function of voltage setting is shown in Figure 70 (right). From the measured results, the filter displays the ability to compensate ± 550 ps/nm with settings between 0 and 7 V.
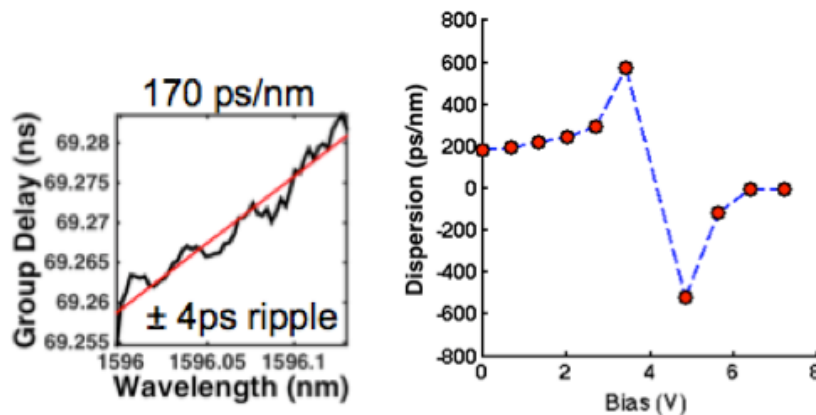
Figure 70. (Left) Example of a linear fit through a group delay data showing a measured dispersion of 170 ps/nm and a group delay ripple of +/- 4 ps. (Right) Filter measured dispersion as a function of voltage bias.

5.4.5 Link Testing

The final step to verify the filter's functionality is to the compensate dispersion of a full transmission link. Transmission measurements were performed on a 40 Gbits/sec NRZ-OOK signal according to the setup in Figure 71.
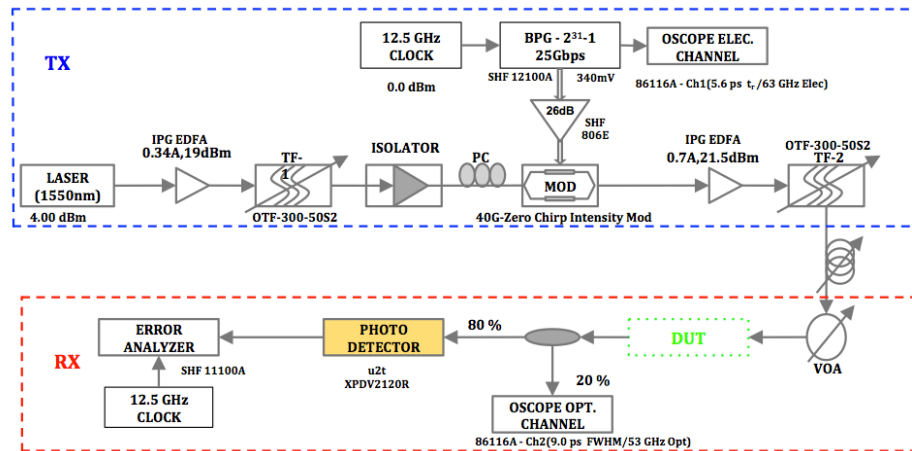
Figure 71. Dispersion equalizer transmission testbed.

A 10-kilometer single-mode fiber spool was used to introduce dispersion. For the given fiber length, the calculated dispersion expected is approximately 170 ps/nm. The received data for the uncompensated link shows a distorted and closed eye diagram as seen in Figure 72 (left). The dispersion equalizer is introduced and biased accordingly to fully compensate the dispersion. Figure 72 (right) shows the compensated detected eye diagram demonstrating the signal improvement over the uncompensated case. The result then assures the filter's proper functionally by compensating a 40 Gb/sec signal. It is important to recall that dispersion tolerance is inversely proportional to bit-rate square, and for a 40 Gb/sec signal that is equivalent to 4 Km of uncompensated propagation on single-mode fiber. Therefore, the filter presented here provides sufficient dispersion compensation for high-speed communications with data rates up to 40 Gb/sec.
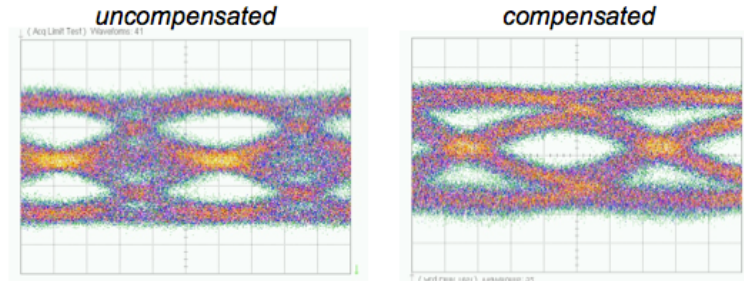
Figure 72. Eye diagrams for the uncompensated transmission link (left) and compensated link (right).

5.5 Conclusion

A programmable 10-stage monolithically integrated lattice filter dispersion compensator was demonstrated on an integrated Si3N4 waveguide platform that offers superior performance for system loss due to its low waveguide propagation loss. This single device can compensate for a bank of WDM channels on a grid of 100 GHz with a 0.6 dB maximum propagation loss. The platform also provides a tighter bend radius, which directly corresponds with a footprint reduction of more than twice of that of its silica counterparts. The device can compensate +/- 550 ps/nm and dispersion compensation was demonstrated on a 40 Gbits/sec NRZ-OOK signal.

5.6 References

[1] K. Takiguchi, K. Jinguji, K. Okamoto and Y. Ohmori, "Variable group-delay dispersion equalizer using lattice-form programmable optical filter on planar lightwave circuit," in IEEE Journal of Selected Topics in Quantum Electronics, vol. 2, no. 2, pp. 270-276, Jun 1996.

[2] H. Kawashima, N. Matsubara, and K. Nara, "Polarization Insensitive Wideband Tunable Dispersion Compensator with Integrated PLC Type Polarization Diversity Circuit," in Optical Fiber Communication Conference and Exposition and The National Fiber Optic Engineers Conference, Technical Digest (CD) (Optical Society of America, 2006), paper OThE6.

[3]   F. Horst, R. Germann, U. Bapst, D. Wiesmann, B. J. Offrein and G. L. Bona, "Compact tunable FIR dispersion compensator in SiON technology," in IEEE Photonics Technology Letters, vol. 15, no. 11, pp. 1570-1572, Nov. 2003.

[4]   Richard Jones, Jonathan Doylend, Paniz Ebrahimi, Simon Ayotte, Omri Raday, and Oded Cohen, "Silicon photonic tunable optical dispersion compensator," Opt. Express 15, 15836-15841 (2007).

[5]   S. S. Djordjevic et al., "Fully Reconfigurable Silicon Photonic Lattice Filters With Four Cascaded Unit Cells," in IEEE Photonics Technology Letters, vol. 23, no. 1, pp. 42-44, Jan.1, 2011.

[6]   Hiroshi Takahashi, "Planar lightwave circuit device for optical communication: present and future," Proc. SPIE 5246, Active and Passive Optical Components for WDM Communications III, (14 August 2003).

[7]   Jared F. Bauters, Martijn J. R. Heck, Demis John, Daoxin Dai, Ming-Chun Tien, Jonathon S. Barton, Arne Leinse, René G. Heideman, Daniel J. Blumenthal, and John E. Bowers, "Ultra-low-loss high-aspect-ratio Si3N4 waveguides," Opt. Express 19, 3163-3174 (2011).

[8]   C. R. Doerr, M. Cappuzzo, A. Wong-Foy, L. Gomez, E. Laskowski and E. Chen, "Potentially inexpensive 10-Gb/s tunable dispersion compensator with low polarization sensitivity," in IEEE Photonics Technology Letters, vol. 16, no. 5, pp. 1340-1342, May 2004.

[9]   J. Gehler, R. Wessel, F. Buchali, G. Thielecke, A. Heid, and H. Bülow, "Dynamic Adaptation of a PLC Residual Chromatic Dispersion Compensator at 40Gb/s," in Optical Fiber Communication Conference, Technical Digest (Optical Society of America, 2003), paper FN7.

[10]   Coldren, Larry A., Scott W. Corzine, and Milan L. Mashanovitch. Diode lasers and photonic integrated circuits. Vol. 218. Wiley. com, 2012.

Chapter 6

Integrated Waveguide Optical Gyroscope (IWOG)

6.1 Introduction

Gyroscopes are useful in a wide range of applications, from the less demanding commercial end to the more demanding military applications such as aircraft navigation. These highly sensitive gyroscopes, when paired with other sensors, can be used to precisely verify an object's orientation assisting in the determination of the object's position or flight path. Such sensors become of crucial need when uninterrupted data flow is required, as in GPS starved environments.

An optical gyroscope based on optical interference has a large advantage over a mechanical gyroscope because it does not rely on moving parts. This makes optical gyroscopes more stable and reliable, as they are not prone to degradation from vibrations, which is common in military applications such as tactical munitions [1]. Present day optical gyroscopes are large, consume a great amount of power, and are expensive to deploy with every soldier. Photonic integration provides the opportunity for improving the current state-of-the-art performance of optical gyroscopes while maintaining the SWAP+C of current MEMS based gyroscopes.

Photonics integration provides an overall better performance than fiber and laser gyros by having every gyro component integrated into a small single package, thus lowering the reflection sensitivity. Optical integration also solves the performance limitation of discrete components and leads to the integration of the electronic control for the optical gyro, further reducing SWAP+C.

6.2 Theory

The integrated waveguide optical gyroscope (IWOG) is a rotation sensor that relies primarily on optical interference effects in optical waveguides in order to provide a measurement. The device operates by using the Sagnac effect, where two counter-propagating waves experience a phase difference on a rotating platform. The most basic schematic for an IWOG is shown in Figure 73. One important aspect to note, is that unlike the delays on the previous chapter, the waveguide coil used on the optical gyro must not change direction in order to avoid the Sagnac effect and therefore no s-bend can be used.
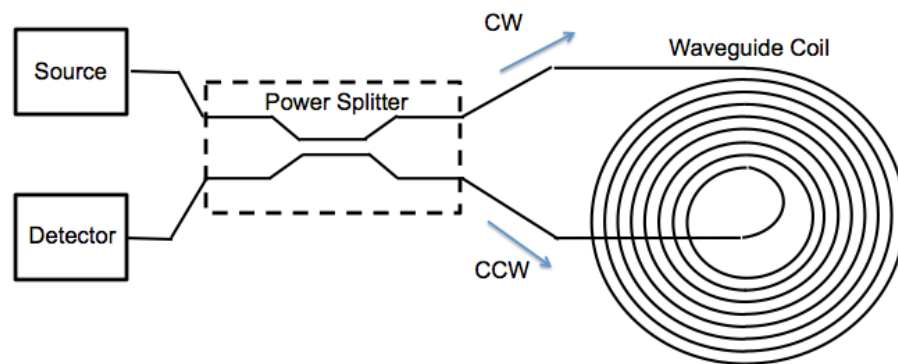
Figure 73: The simplest scheme of the integrated waveguide optical gyroscope.

In its simplest form, the IWOG is composed of a light source, a power splitter, a waveguide coil, and a photodetector. The power from the light source, usually an ASE source to avoid

backscatter reflection/noise, is split into two components by the optical splitter and is input into the waveguide coil as a clockwise and counter-clockwise signal. The counter-propagating signals travel through the waveguide coil accumulating a phase difference according to the Sagnac effect and are then recombined at the photodetector completing the passive interferometer. The signal from the optical gyroscope is directly proportional to the angular rotation velocity Ω according to the gyroscope Sagnac scale factor (K_{ssf}). In the case of an interferometric optical gyroscope presented herein, the change in phase due to the Sagnac effect can be written as [2]:

$$\Delta\phi = K_{ssf}\Omega$$

where $\Delta\phi$ corresponds to the change in phase between the clockwise and counter-clockwise signals, and for a fiber coil K_{ssf} is defines as [3]:

$$K_{ssf} = \frac{8\pi NA}{\lambda c}$$

where N is the number of turns in the coil, A is the area enclosed by the coil, λ is the operating wavelength, and c is the speed of light. Therefore, by calculating the phase change due to all sources of phase noise, a noise equivalent rotation rate can be calculated which will be equivalent to the minimum detection resolution of the optical gyroscope limited by the sources of noise. The noise equivalent rotation can then be evaluated as:

$$\Omega_{noise} = \frac{\Delta\phi_{noise}}{K_{ssf}}$$

As a result, by carefully defining all the possible sources of phase noise, a model can be established which could theoretically determine the optical gyroscope sensitivity providing the PLC and PIC designer with the appropriate parameters required for the integration of an optical gyroscope for a specific target performance.

Therefore, in this dissertation as in [4], we consider four sources of noise: shot noise, relative intensity noise (RIN) from the source, thermo-refractive noise, and thermal noise of the preamplifier. From [4], the total phase noise can be defined as:

$$\Delta\phi_{noise} = \Delta\phi_{shot} + \Delta\phi_{RIN} + \Delta\phi_{thermo-refactive} + \Delta\phi_{thermal}$$

where each of the individual noise sources is defined below.

$$\Delta\phi_{shot} = \sqrt{\frac{2hfB}{P_o\eta}} \text{ (rad/√Hz)}$$

where h is Planck's constant, f is the operating frequency (f = c/λ), B is the measurement bandwidth, η is the quantum efficiency of the photodetector, and Po is the equivalent detected power ($P_o = P_{source}*e^{-\alpha L}$).

$$\Delta\phi_{RIN} = \sqrt{10^{\frac{RIN}{10}}} \text{ (rad/√Hz)}$$

where RIN is the relative intensity noise of the source in dBc/Hz.

$$\Delta\phi_{thermo-refractive} = 4.3\times10^{-7}\sqrt{\frac{L}{40}} \text{ (rad/√Hz)}$$

where L is the coil length in meters. The thermo-refractive noise is obtained from [xx].

$$\Delta\phi_{thermal} = \frac{10^{-9}}{\eta P_o\sqrt{R}} \text{ (rad/√Hz)}$$

where R is the termination resistance for the detector and in this case it is assumed to be 1 kΩ.

With all of the noise sources defined, the minimum detected rotation as a function of coil length can be calculated. The following assumptions were used for this initial verification of the gyro model:

- RIN = -140 dBc/Hz

- B = 1 Hz

- $\eta = 0.9$

- $P_o = 100$ mW

- Waveguide loss (α) = 1 dB/m

- Crossing loss = 0.02 dB/crossing

- Minimum bend radius = 1 mm (helps determine the number of crossings)

The result of the model output is displayed in Figure 74. The plot shows that with the current assumptions a 20 meter spiral could potentially reach a detection limit of 13.78 °/hr/√Hz, sufficient for a rate grade gyro based on detection limit alone. Further investigation based on the model and waveguide design will be performed on the following section.
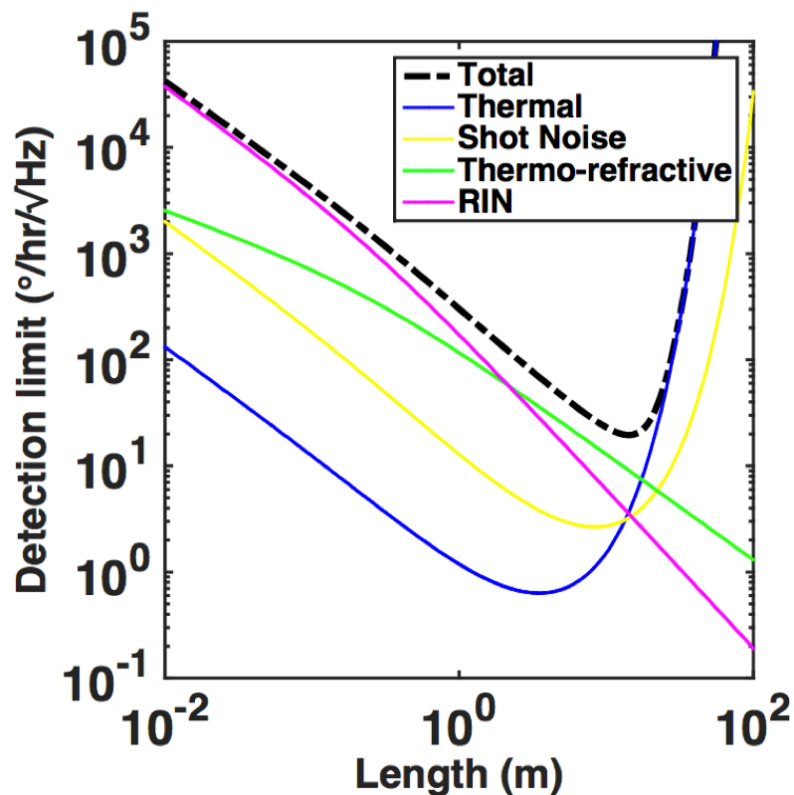
Figure 74: Optical gyroscope model output based on 4 major source of phase noise, showing theoretical minimum detectable rotation rate as a function of coil length based on calculations from [4].

6.3 Design

Figure 75 shows a typical schematic of a fully integrated (reciprocal) waveguide optical gyroscope (IWOG). It is important to note that the device is divided into two different sections: the coil and the active section, where the latter includes optical sources, photo detectors, and modulators. While it is possible to integrate the device in its entirety onto a single waveguide platform, i.e. Silicon hybrid or InP, this approached is not preferred due to a sensitivity limitation which is a direct result from the waveguide propagation loss limiting the maximum amount of delay to be integrated. Therefore, the ultra-low loss planar waveguide platform allows for meters of coil integration which would otherwise not be feasible; on the other hand, the lack of active devices on said platform requires a separate design of each section. Each section can then be further integrated either via an active/passive coupling approach [5], or through a co-packaging approach [6]. This dissertation will only cover the design, fabrication, and testing of the passive coil integration alone, although design decisions were made to allow for future integration of both platforms, which will be discussed in the next sections.
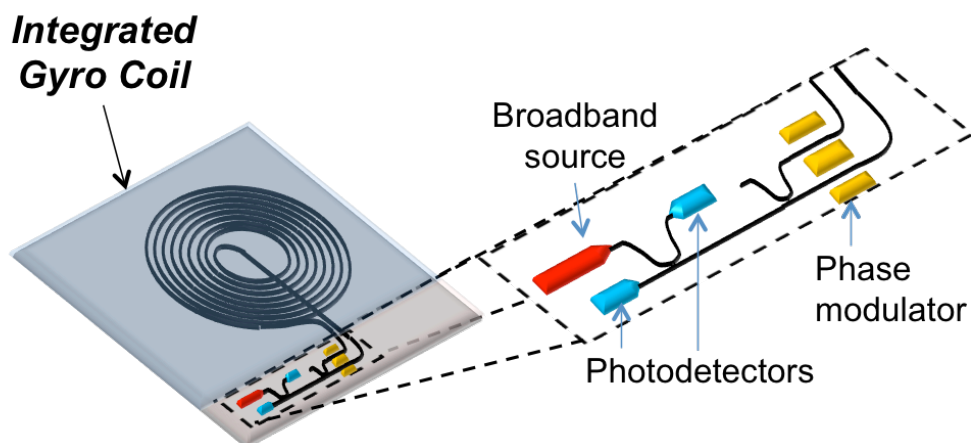
Figure 75: Integrated Waveguide Optical Gyroscope schematic [4].

In order to properly design the coil for the IWOG, the waveguide core geometry must be decided upon to meet the required specification of the desired application. Figure 76 broadly identifies the application space as a function of gyro sensitivity and dynamic range specifications. Gyroscope grades can also be defined as according to angle random walk (ARW) and bias drift; such definitions are shown in Table 6, where ARW describes the average deviation of the output signal as a result of random (white) noise, and the bias drift measures the peak-to-peak deviation of the output signal. As shown here, different applications will require different specifications, therefore in order to move forward with the IWOG design a range of specifications and applications must be chosen.

Parameter	Rate grade	Tactical grade	Inertial grade
Angle random walk	> 0.5 °/√hr	0.5 – 0.05 °/√hr	< 0.001 °/√hr
Bias drift	10 – 1000 °/hr	0.1 – 10 °/hr	< 0.01 °/hr

Table 6: Gyroscope grades based on ARW and bias stability [7].

Based on the waveguide platform described here, tactical gyro performances can be delivered in a compact footprint, not achievable with current fiber optic gyroscope technology. As a result, with the goal of designing a gyroscope which offers high-performance in a package that is significantly smaller than that of standard FOGs, the coil will have a reference target of gyro sensitivity 1°\hr (tactical grade) with a footprint of ≤ 5 cm^2. The two specifications just mentioned, are of course not the only specifications required to design a high-performance gyro but were instead chosen to highlight the performance of the planar waveguide platform, which can achieve very low propagation loss at a small bend radii not possible with its counterpart platform such as silica PLCs.
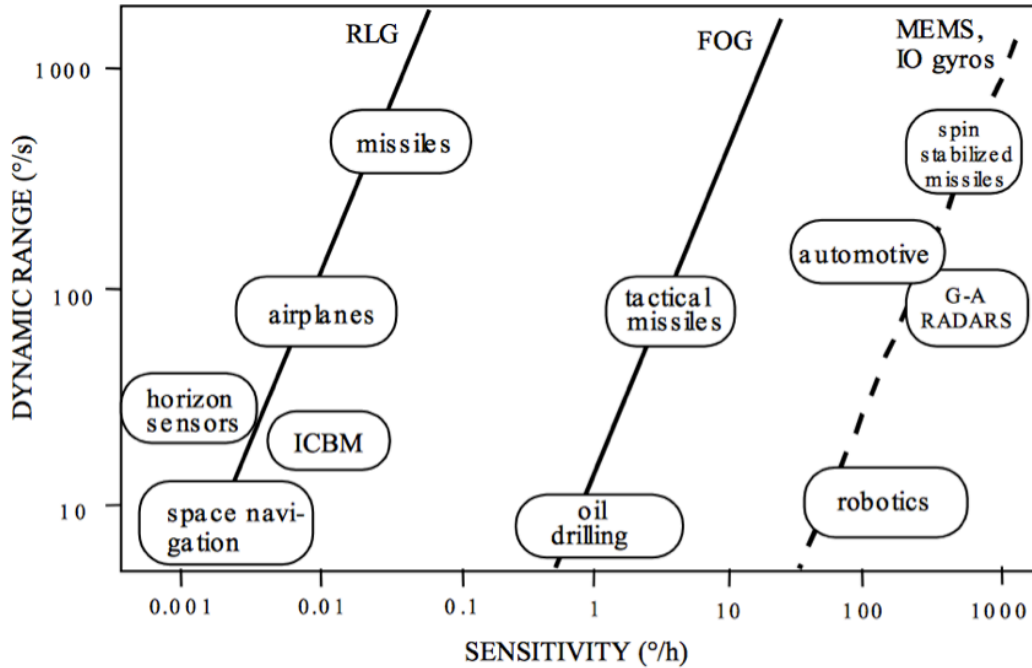
Figure 76: Application areas and performances of the RLG and FOG gyroscopes (full lines), and projected performance for MEMS and integrated waveguide optical gyro (IWOG). Figure from [8].

With the intention of achieving a gyro sensitivity of 1 ∘\hr, a family of curves can be generated following the steps in the theory section above displaying the sensitivity for multiple waveguide propagation loss as a function of coil length, as seen in Figure 77. From the figure it can be seen that a waveguide loss of $\leq$ 3 dB/meter with at least 5 meters of propagation length are required to push the waveguide coil into the desired tactical sensor regime.

110
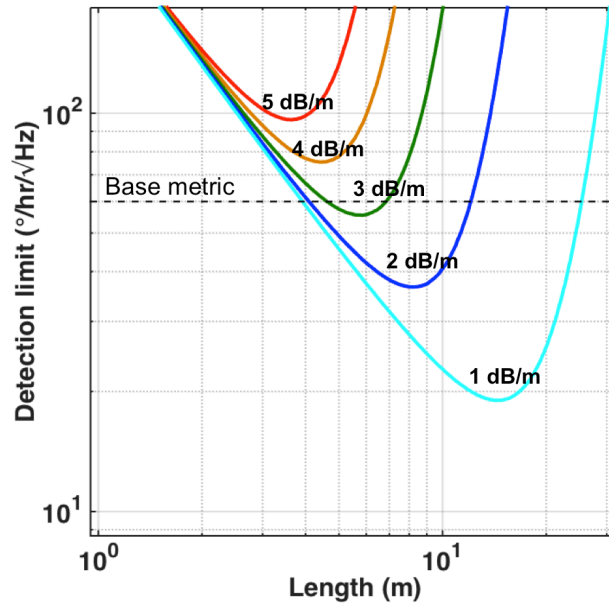
Figure 77: IWOG design curves for a specified gyro sensitivity of 1 ∘ \hr. Plot shows gyro sensitivity for multiple waveguide losses as a function of coil length.

6.4 Single Layer Gyro Coil

The integrated waveguide coil was laid out as a modified version of the Archimedean spiral. The gyroscope coil is very similar to the conventional spiral explained in the building blocks chapter with the exception that in order to avoid the nullification of the Sagnac effect, the light cannot change direction (clockwise to counter-clockwise or vice-versa) in the middle of the spiral. As a result, the spiral-in and spiral-out geometry, which is achieved through the use of the s-bend, cannot be used since a change in direction occurs. Thus, the spiral used for this application can only spiral in until it reaches a desired bend radius and then an output waveguide crosses through all the spiraled waveguides. A conventional Archimedean spiral and a gyroscope spiral are placed side by side on Figure 78 for reference.

111
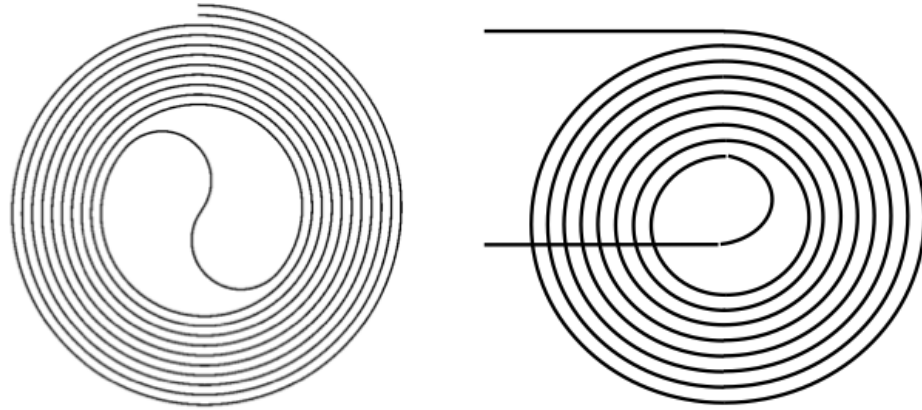
Figure 78: (Left) Archimedean spiral w/ s-bend. (Right) IWOG modified Archimedean spiral with output crossing multiple waveguides.

The waveguide core geometry was determined based on the requirements of the previous section. A core of thickness of 90 nm as seen in the platform chapter can meet the propagation loss and footprint required for the target gyro sensitivity. Although other core geometries (thickness/width) would also satisfy the condition with much lower loss and still meet the footprint requirement, a core of 2.8 μm width and 90 nm thickness was chosen in order to rely on the active/passive integration coupler work developed in [6] so that the low loss integrated coil could in the future be monolithically integrated with the gyro front-end. The fabrication process follows the steps laid out in the platform chapter.

6.4.1 Facet Reflection

The wave reciprocity, as previously stated, only applies to a transmitted wave; therefore, any source of reflection along the way degrades the gyro performance, and it is essentially seen as a source of noise. One major source of reflection on the IWOG is the Fresnel back-reflection at the chip-fiber interface or chip-chip interface. One way to avoid back-reflections is to add anti-reflection coatings to the waveguide output or to angle the output waveguide as

to degraded backwards coupling. The waveguide spiral gyro was designed around the angled facet approach.

If we assume a Gaussian approximation for the fundamental TE mode of the waveguide, we can show the reflectance can be approximated to be [9]:

$$R(\Theta) = R_f(\Theta)\exp\left[-\left(\frac{2\pi \cdot n_{cladding} \cdot w \cdot \theta}{\lambda}\right)^2\right]$$

where w is the beam width, which is a direct result of the waveguide geometry, and $R_f(\theta)$ is the Fresnel reflection coefficient of a plane wave defined by:

$$R_f(\Theta) = \left(\frac{n_1 \cdot \cos(\Theta) - \sqrt{n_2^2 - n_1^2 \cdot sin^2(\Theta)}}{n_1 \cdot \cos(\Theta) + \sqrt{n_2^2 - n_1^2 \cdot sin^2(\Theta)}}\right)^2$$

Although the Gaussian approximation greatly deviates for very large reflections, one can deduce from the reflectance equation that increasing waveguide angle and/or increasing beam width can decrease the reflectivity. Since our waveguide geometry has been determined by the application, the beam width will be held constant (waveguide geometry) while the reflectance is simulated and plotted as a function of angle in Figure 79 on a chip to air interface.

Based on the calculated reflectance plot, an output angle of 21° was chosen which corresponds to a reflectance of 10^{-4}. Although lower levels can be achieved with higher output angles, alignment becomes impractical and coupling efficiency degrades. As a result, in order to attain additional reflection suppression and better coupling efficiency, an anti-reflection coating at the output facet is recommended. By doing a simple calculation according to refraction laws, it was found that the single-mode fiber needed to be angled by approximately 31° in order to align with the tilted output waveguide.
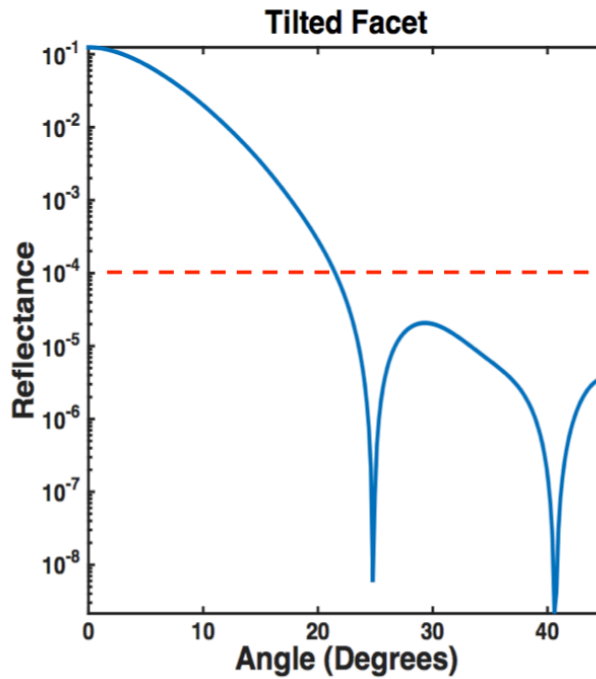
Figure 79: Simulated reflectance as a function of output waveguide angle for a 2.8 x 0.09 μm planar Si3N4waveguide. (Dashed line = chosen reflectance level)

6.4.2 Waveguide Crossings

Since the waveguide coil is to be fabricated on a single layer platform waveguide, crossings are unavoidable because as previously explained the s-bend reverses the direction of light propagation, thus nullifying the Sagnac effect. Consequently, the waveguide crossings must be optimized as to reduce any potential source of reflection and additional loss. Bauters et al. have demonstrated that on the same high-aspect ratio $Si_3N_4\backslash$ SiO_2waveguide platform, waveguide crossing loss can be as low as 0.02 dB per crossing at a 90° angle [10]. As described in [10], the waveguide crossing loss decreases as the angle between the waveguide increases. For crossing angles of 30°, losses can be greater than 1dB per crossing and less than 0.1dB per crossing at 60° crossings, reaching the lowest value of 0.02dB/crossing at 90°. It is important to note that the low crossing loss can be achieved mainly as a result of the weakly confined mode of the high-aspect ratio geometry which suffers very little index

114

perturbation from the intersecting waveguide. Therefore, as the geometry changes to a more confined fundamental TE mode, the losses per crossing increases for the same angle intersection. Figure 5.6 (a) shows that the loss per crossings goes from 0.02 dB/cross for a 40nm thick core, which is the geometry used in [10], to 0.1dB/cross for a 90 nm thick core which is the geometry used for the gyroscope coil. Since the waveguide geometry has been locked for this application, the waveguide crossing must be optimized accordingly.
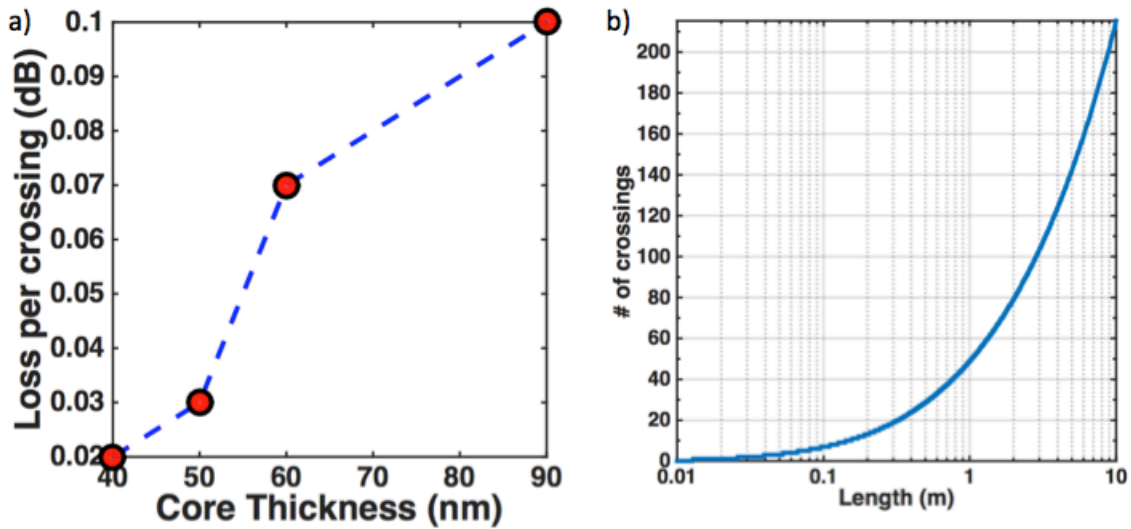
Figure 80: (a) Loss per 90 degree crossing for different core thickness. (Please note that the width changes for each thickness, but all geometries are single-mode) (b) Plot displaying the total number of crossings on a single layer gyro coil as a function of length for a minimum bend radius of 1mm and waveguide separation of 50μm.

In order to optimize the waveguide crossings for loss, we first need to determine the amount of crossings. Figure 80 (b) displays the total number of crossings as a function of length. As already resolved, the desired length required for a tactical grade gyroscope is a total of 5 meters which corresponds to approximately 140 crossings as seen in Figure 80 (b). Therefore, the total contribution of the crossings to the overall device is 14 dB for a single pass alone! Because the waveguide crossing is seen during spiral in and spiral out, the 140 waveguide crossings are equivalent to 280 crossings for the entire structure which

corresponds to a total loss of 28 dB for the crossings alone. As a result, a lower loss cross must be developed.

Multi Mode Interference (MMI) Crossings

It has been shown that the self-imaging property of a MMI structure can be used to attain low-loss waveguide structures [11][12]. The multi-mode interference is used to mitigate the diffraction through the waveguide crossing by focusing the beam to a width much smaller than the MMI width at the crossing center; this condition happens even though the lateral confinement is drastically reduced at the waveguide crossing [13]. A similar MMI-like crossing was designed for the ultra-low loss $Si_3N_4\backslash SiO_2$ waveguide platform, with the idea of replacing the conventional "normal" waveguide intersection in the gyro coil.

The schematic of the MMI crossing can be seen in Figure 81.
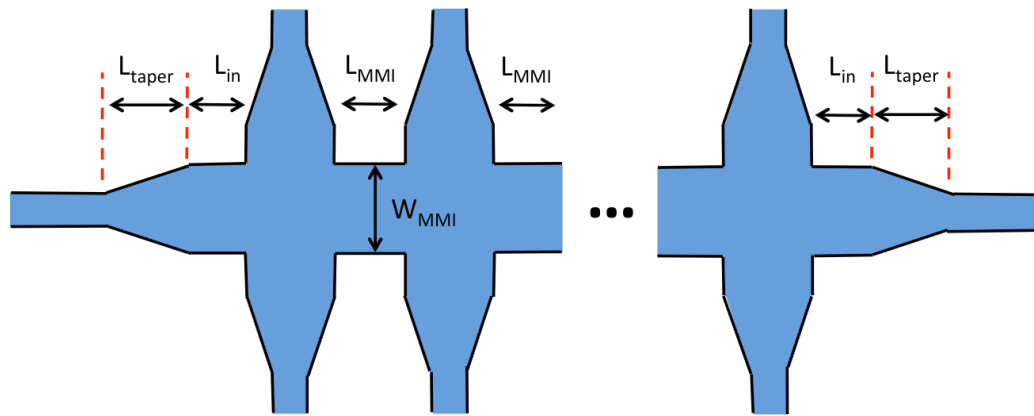
Figure 81: Schematic of the proposed MMI waveguide crossing structure

The MMI-like structures can be divided into 3 different sections: single-mode input, taper, and MMI section. In Figure 81 the important structure dimensions are labeled and will be properly designed to achieve the lowest loss per crossing. The waveguide crossings are placed periodically along the MMI length according to the self-imaging principle of multimode waveguides. In order for the crossings to be useful for the optical gyro coil, the

116

crossing spacing needs to closely match the waveguide spacing in the integrated coil, in this case 50 μm. Consequently, the multimode section of the waveguide was designed to support three higher order TE modes (TE$_{00}$, TE$_{01}$, TE$_{02}$), but because of the symmetry caused by the input excitation position only m = 0 and m = 2 TE modes are excited. As a result, the self-imaging condition is reduced to:

$$L_\pi = \frac{2\pi n}{\beta_0 - \beta_2}, n: integer$$

The MMI section of the device was designed with a width of 7μm, where Figure 5.8 shows the effective index for the first and third order mode is 1.475 and 1.451; therefore, giving a beating length of 64.5μm which closely corresponds to the waveguide spacing.
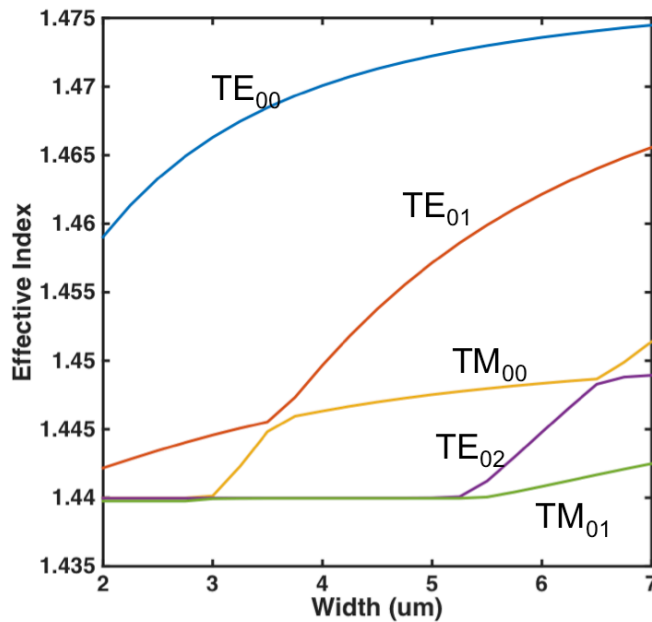
Figure 82: Neff scan for a 90 nm thick waveguide core as a function of waveguide width. (Cut-off for single mode condition is 3μm)

The taper section was designed as a short linear taper with a length of 1μm. The entire structure was then simulated using Photon Design's FIMMWAVE, an Eigen mode expansion (EME) tool. Figure 83 (a) shows the simulated field intensity for a 5-crossing device, while

Figure 83 (b) provides a summary of the final simulated dimensions to achieve low loss crossing. With the provided dimension values, the MMI crossing was simulated to achieve losses of 0.01 dB/crossing! Where a regular waveguide crossing on the same platform geometry would have 0.1 dB/crossing.

Parameter	Value
Single-mode waveguide geometry	2.8 um x 100 nm
Ltaper	1 μm
Lin	61 μm
LMMI	56 μm
WMMI	7 μm
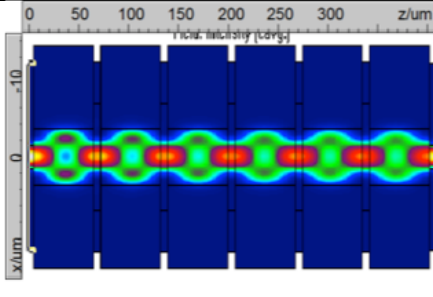
Figure 83: (a) Propagation simulation showing electrical field intensity for a MMI structure optimized for low crossing loss where the crossings are place on the fundamental mode self-imaging period. (b) MMI device's dimension for low loss crossing achieved through simulation optimization loops via Photon Design's FIMMPROP (EME solver).

By using the dimensions shown in Figure 83 (b) and the simulated values for the normal crossing, a comparison can be made between the normal and MMI-like crossing losses as a function of the total number of crossings, as seen in Figure 84. From the figure, given the amount of crossings required for the integrated single layer gyro, the MMI-like structures provide an immense improvement of approximately 27 dB over the normal crossings.
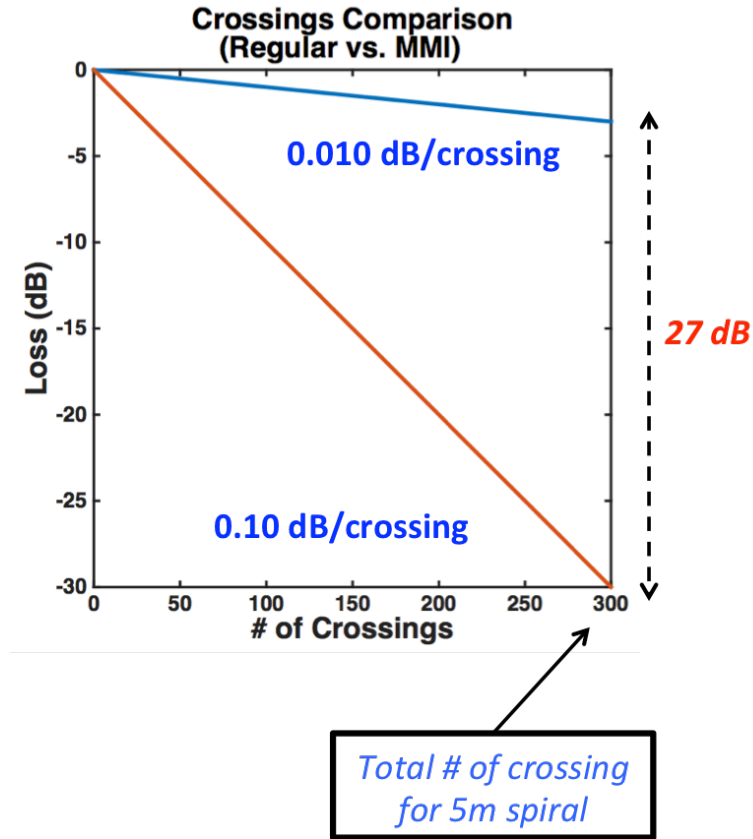
Figure 84: Simulated comparison between the losses of the normal 90-degree crossings against the proposed MMI crossings as a function of total crossing. (The total amount of crossings for a 5-meter gyro coil is highlighted on the figure)

6.5 Results

According to the requirements discussed in the previous section, a mask layout was designed to fully characterize the fabrication of a waveguide coil for use in the optical gyroscope application. Individual test structures for each important coil requirement were also fabricated to de-couple each individual response from the overall coil output. The complete mask layout is shown in Figure 85, where each functional block is highlighted and the results discussed below.
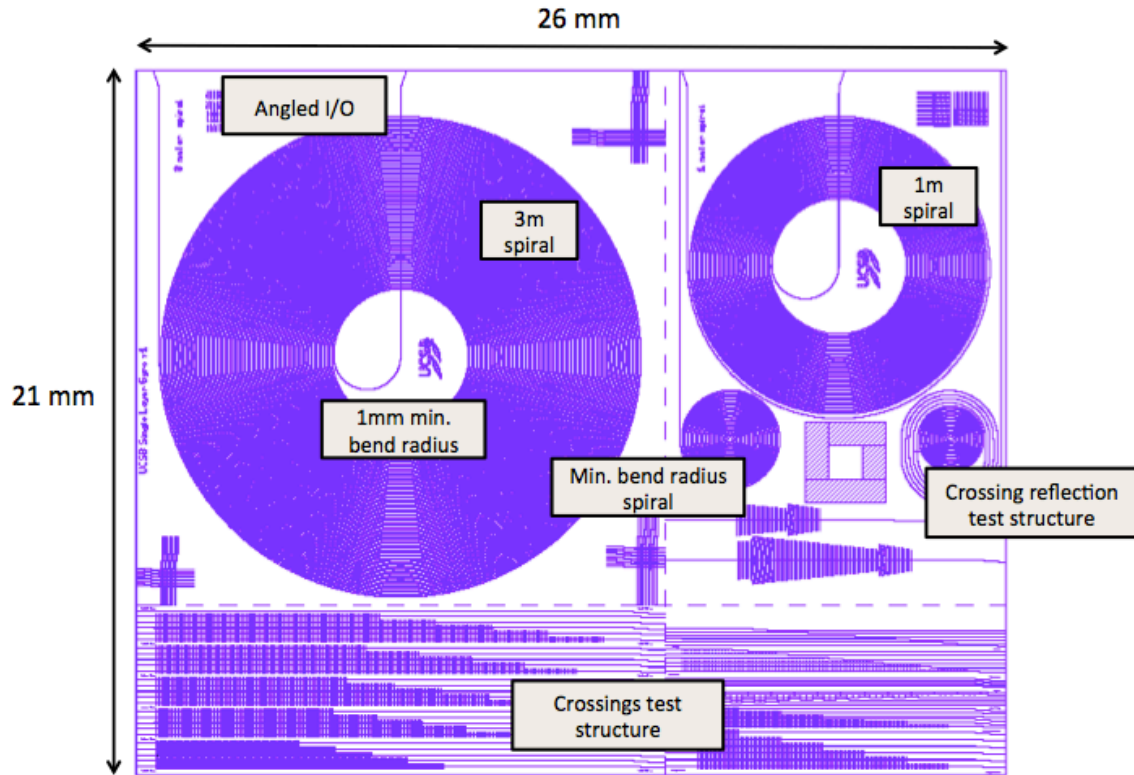
Figure 85: Optical gyro mask layout with each functional block identified.

6.5.1 Waveguide Crossing

As previously shown, waveguide crossings can be one of the major sources of loss and reflection in the optical gyroscope waveguide coil. Therefore, test structures to quantify the crossing loss for the "normal" 90-degree crossing and the suggested MMI crossings were fabricated and tested. The structure consisted of a "cutback-like" type measurement with multiple waveguides each having a different number of crossings. For the "normal" waveguide crossings, which had simulated losses of 0.13 dB per crossing, a total of six different waveguides were fabricated each having a different number of crossings corresponding to 25, 50, 75, 100, 125, and 150 crossings. By measuring the insertion loss of each waveguide individually and performing a linear fit to the measurements, the slope of the

fit can be determined thus representing the loss per waveguide cross. The cutback measurement can be independent of the coupling loss provided that the coupling condition is similar to all the waveguides, a good assumption if all of the waveguides are close together. In order to minimize the errors introduced by the coupling variation, which was measured to be +/- 0.87 dB for a diced unpolished facet, a large number of waveguide crossings were chosen so that the difference between insertion losses was much greater than the coupling uncertainty. In this case, the difference between 25 to 150 waveguide crossings was simulated to be 16.25 dB. A microscope image of the fabricated test structure can be seen in Figure 86, where a closer image is also shown for the waveguide crossing. The waveguide dimensions and crossing spacing were chosen to replicate the crossing on a gyroscope coil, which are in this case 2.8 um in width by 90 nm in thickness and each spaced by 50 μm from center-to-center of the waveguide; as previously mentioned, the waveguide spacings were chosen in order to minimize the crosstalk between adjacent waveguides.
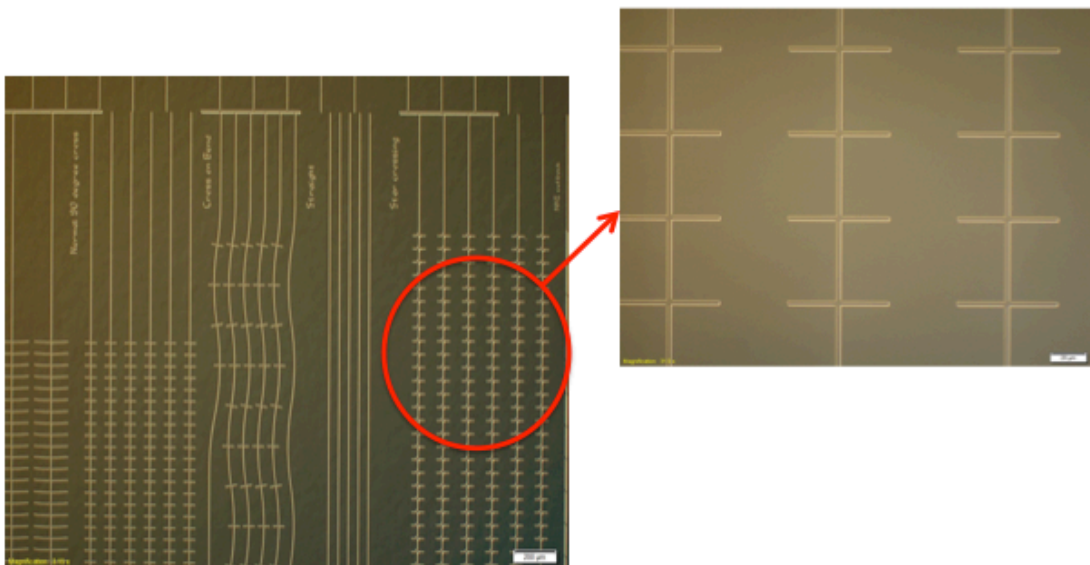
Figure 86: Microscope image of the fabricated cutback test structures for the normal 90-degree waveguide crossings

121

The crossing loss was measured at a wavelength of 1550nm and a polarization controller was used to excite TE polarization only, due to the high birefringence of the high-aspect ratio waveguide, which as discussed is a benefit to the optical gyro performance. In order to maintain similar coupling conditions between waveguides, a cleaved fiber with the addition of index matching gel was used to excite the fundamental TE mode of each waveguide. The cutback measurement results for the normal 90° crossings are shown in Figure 87. The blue diamonds are the insertion loss measurement for each individual waveguides with different numbers of crossings. A linear fit was performed, shown as the red dashed line, and the slope extracted with an R squared value of 0.993 verifying the quality of the fit. The slope, which corresponds to the waveguide crossing loss, was measured to be 0.1 dB/crossing. The measured loss is in notable agreement with the simulated value of 0.13 dB/crossing calculated via Finite Difference Time Domain (FDTD) simulation done through the Photon Design simulation software.
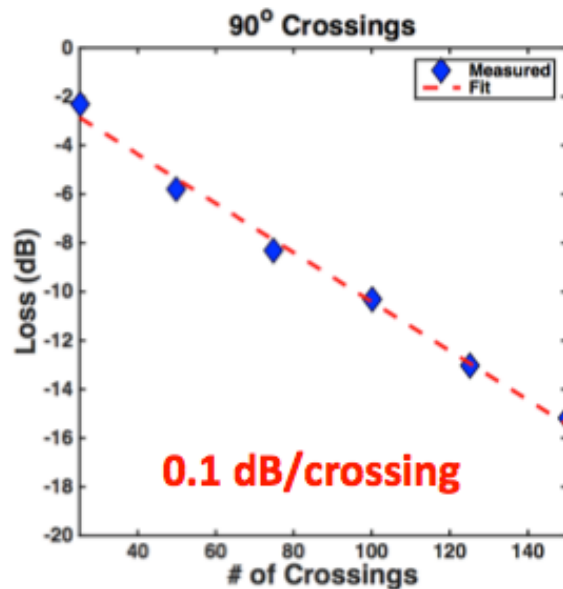
Figure 87: Normal 90-degree crossing cutback measurement result.

Because the waveguide crossings on a spiral are actually crossings of the bent waveguide with the straight waveguide while spiraling-in and the opposite (straight with bent crossings) while spiraling-out, cutback test structures with crossings on a bend as well as bending crossings were fabricated but no measurable difference from the regular test structures was seen since the bend radius is well above the minimum bend radius of 1 mm.

To compare the performance for the MMI-type crossing versus the traditional crossings, a similar cutback test structure was fabricated. Because the MMI lengths are much larger than the "normal" waveguide crossings, FDTD simulations become impractical due to the large computation area required; to simulate the performance of the MMI crossings, an EigenMode Expansion (EME) solver was then used. According to simulations, a crossing loss of 0.02 dB can be achieved if the MMI crossing is properly designed. As in the case of the normal crossings, the appropriate number of waveguide crossings must be selected to mitigate the uncertainties from the coupling; thus, because the MMI crossings were simulated to have a much lower crossing loss, a greater number of waveguide crossings will be required to make the insertion loss measurable. In this case, five waveguide were fabricated each having a total of 100, 125, 150, 175, and 200 crossings. Figure 88 shows a microscope picture of the fabricated MMI cutback test structure with a zoomed in image of multiple waveguide crossings on a single MMI waveguide.
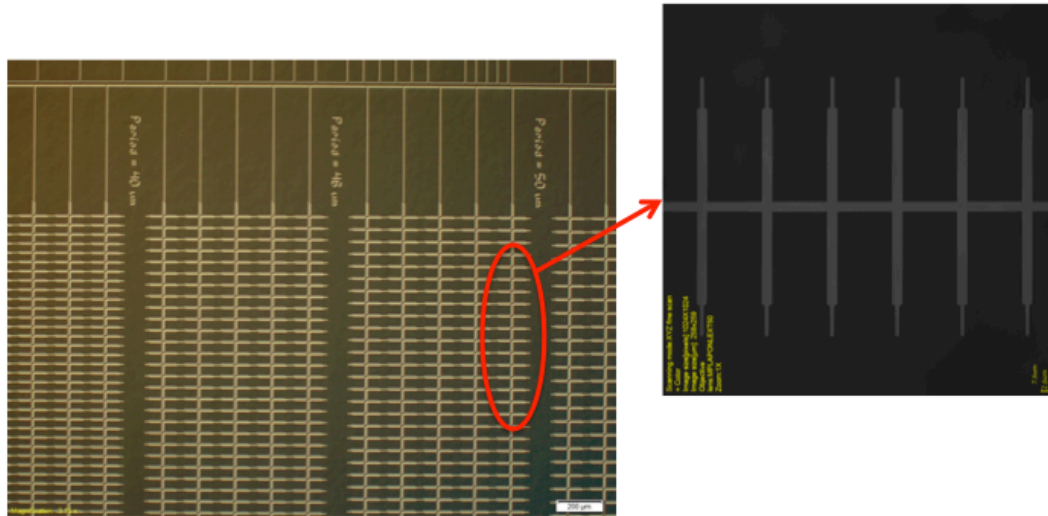
Figure 88: Optical microscope image of the cutback test structure for the MMI type waveguide crossings

The insertion loss of the MMI cutback test structure was then measured in a similar fashion as the normal waveguide crossings. The measured results are displayed in Figure 89 (Left) below. From the linear fit of the measurements, a crossing loss of 0.01 dB was extracted with an R squared value of 0.876. The measurement shows that the MMI crossings can provide a >10x improvement over the conventional normal waveguide crossings.
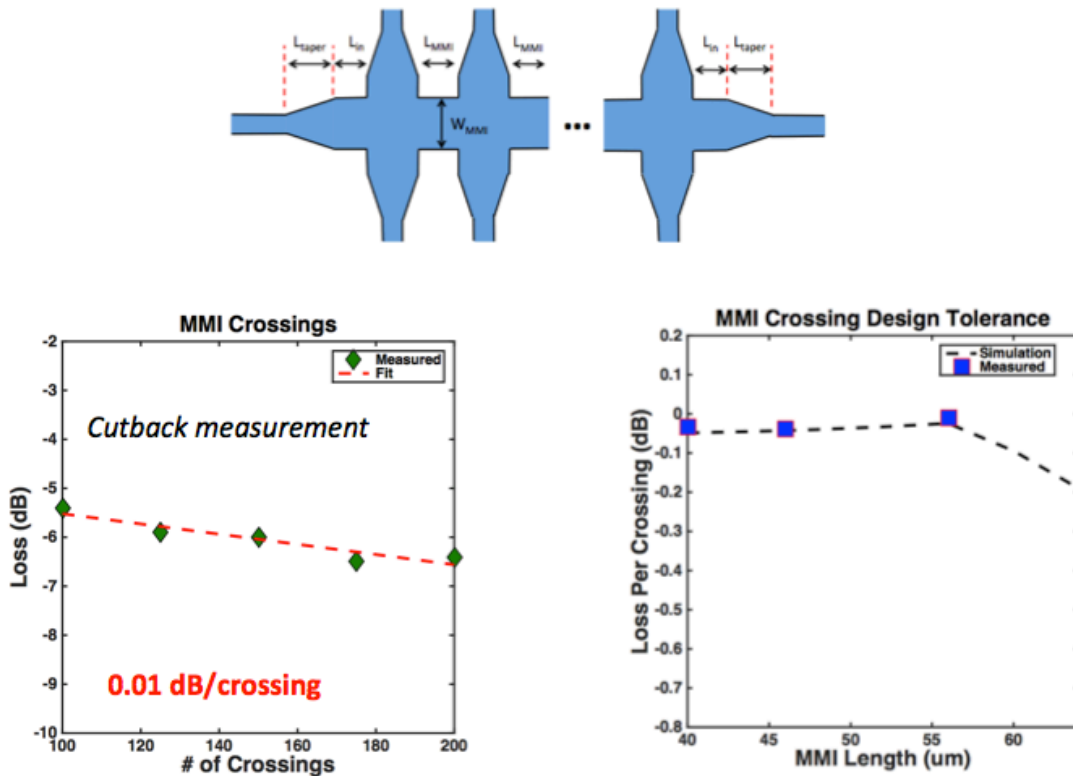
Figure 89: Measured results for the cutback measurements from the MMI based crossings. (Left) Loss as a function of the number of crossings. (Right) Crossing loss as a function of crossing (MMI) spacing.

The tolerance of waveguide crossing loss on the MMI beat length is also of great importance since a very tight tolerance might make this type of crossing impractical due to lithography and etch bias variations. To analyze the dependence of the MMI crossings on the MMI beat length, two additional test structures with different periods (46 um & 40 um) from the nominal 56 um were fabricated and the crossing loss extracted via the cutback method. Figure 89 (Right) shows the measured crossing loss for all three different MMI periods. As can be seen from the figure, the measurements are in agreement with simulation shown as the dashed line, and even for a slightly un-optimized MMI crossing losses much less than 0.1 dB are still achievable making the MMI crossing a suitable and tolerant design to replace the normal waveguide crossings. Table 7 below provides a brief summary of the measured and simulated value for each type of crossing, including the type of simulation used for each.

Type	Loss [dBm] (simulated)	Loss [dBm] (measured)	Simulation
Normal	-0.13	-0.10	FDTD
Normal	-0.38		EME
MMI	-0.02	0.01	EME

Table 7: Summary of simulated and measure values for each type of waveguide crossing.

6.5.2 Waveguide crossing reflection

Because optical reflection can be a major source of noise on the IWOG performance, we designed a waveguide test structure to quantify the amount of power reflected by a single waveguide crossing through the use of the optical backscatter reflectometer (OBR), which provides high sensitivity and dynamic range for the measurement. The test structure consists of a spiral that has a bend radius above the minimum bend (R_{min}) radius and spirals all the way in to radii below R_{min}. Therefore, before the spiral reaches the minimum bend radius, a single 90° crossing is placed along the way. Since the spiral terminates at a radius much smaller than R_{min}, then test structures assure that the only reflection point is from the crossing alone. Also, because large reflectors tend to show broad reflection peaks, the single crossing must be placed away from facet reflection so that the reflection peak from the single crossing is not overtaken by the facet reflection, here a chosen distance of at least 3cm from the facet reflection. The schematic of the aforementioned test structure is shown in Figure 90 below.
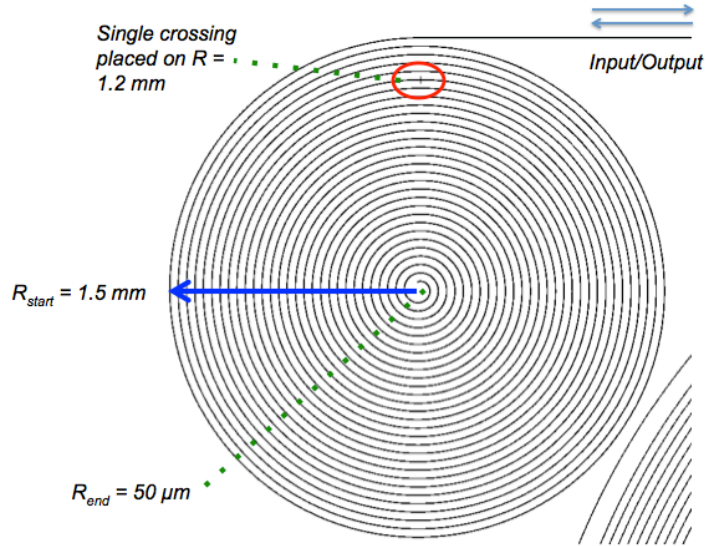
Figure 90: Spiral-in test structure for measuring crossing reflection using the Luna OBR (OFDR). The minimum bend radius of this specific geometry is 1.0 mm.

Because the measurement is to be performed via optical backscattered reflectometry, then only a single input and output is required. To avoid any additional reflection, the spirals terminate at a bend radius of 50 um, which is much smaller than the minimum bend radius of 1 mm. The waveguide crossing was also carefully placed away from the input facet but at a bend radius of 1.2 mm, which is still greater than R_{min}. The OBR backscatter signal of the measurement is shown in Figure 91.
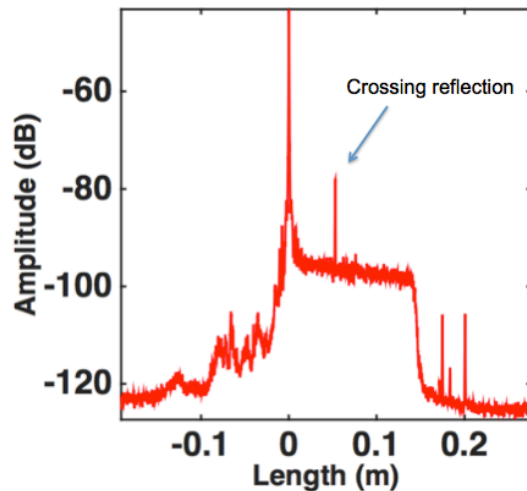
Figure 91: Crossing reflection measurement using a Luna OBR (OFDR).

127

From the backscatter signal, return loss can be calculated which represents the total fractional power returned from the reflection event. From the OBR signal, the return loss (RL) can then be calculated by integrating the scatter level over a width of interest, and this operation can be described by the following equation:

$$RL = 10 \cdot Log10 \left(\sum_{j=data\ start\ index}^{data\ stop\ index} |h_j| \right)$$

Where h_j is the element of the amplitude of the scatter array at the index j. Although this method provides a measured return loss, it does not provide an absolute return loss. That is, if any insertion loss event has occurred before the return loss event the power reflected from the RL event is reduced. Therefore, to find the absolute return loss, any insertion loss event before the measured point must be taken into consideration, which in this case is the coupling loss into the device (the only reflection/loss before the crossing in this test structure). The coupling loss on this geometry with unpolished facets was measured to be 2 ± 1 dB/facet, where the large uncertainty arises from the non-uniform dicing. As a result, to calculate the absolute RL two times the coupling loss power must be added to the RL loss measurement, where the factor of two is needed to account for the nature of measuring reflected power. The measured RL from the test structure was calculated to be -77 dB, and if we consider the worst-case scenario (2*3dB) for the absolute RL calculation, then the absolute RL is -71 dB. Then the total amount of power reflected back is approximately 8E-6 %. Due to the low amount of power reflected back from a single crossing, the reflection points were not included in the gyro performance calculations although further investigation is required.

6.5.3 Gyroscope Spiral

A 3-meter spiral was fabricated, measured, and its values were used to find an approximate gyro performance based on the values measured. Although a 5-meter spiral, as mentioned in the introduction of this chapter, is required to achieve a tactical grade gyroscope angle random walk (ARW), here we fabricated 2 spirals per single die in order to increase yield. The coil lengths were 1 and 3 meters, and here we present the values of the best 3-meter coil fabricated. Figure 92 shows the fabricated 3-meter coil, where an American quarter is placed for size comparison. The 3-meter integrated spiral is smaller than the quarter and occupies a 2.56 cm^2 area. The second photonic chip shown in the figure is the first generation of an optical gyroscope frontend, which includes lasers, detectors and modulators, integrated on a Si-Hybrid platform fabricated by the lab of Dr. John Bowers at UCSB.
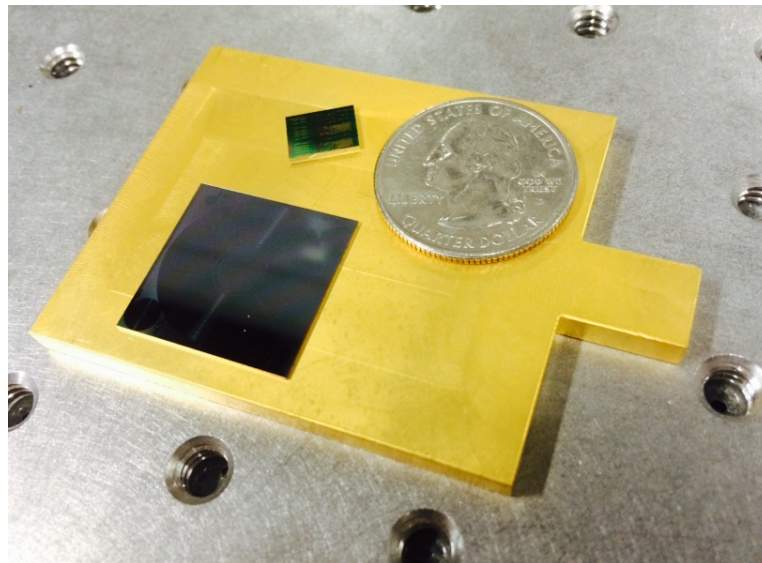
Figure 92: Fabricated Si$_3$N$_4$ 3-meter gyroscope coil together with a Si-Hybrid gyroscope frontend with an American quarter for size comparison.

The coil OBR spectrum is shown in Figure 93 together with the measured insertion loss from fiber in to fiber out measurement. The OBR spectrum to the left of the figure shows a full 3 meters of waveguide propagation with uniformly spaced reflection peaks

corresponding to the waveguide crossings and additional reflection peaks corresponding to scattering points due to fabrication imperfections. The OBR plot is mainly used for assuring the quality of the coil and measuring the waveguide loss. The waveguide propagation loss becomes a difficult measurement due to all of the reflection peaks which must be taken into consideration when performing a linear fit on the data. The waveguide loss was approximated to be around 3 dB/m from the OBR data, which agrees with previous measurement on the same waveguide geometry.

Parameter	value
Length	3 meters
IL (Measured)	28 dB
Coupling loss	*2-3 dB/facet x 2 facet = 4 dB*
Propagation loss	*3 dB/m x 3 m = 9 dB*
crossing loss	*0.07 dB/cross x 204 cross = 14.3 dB*
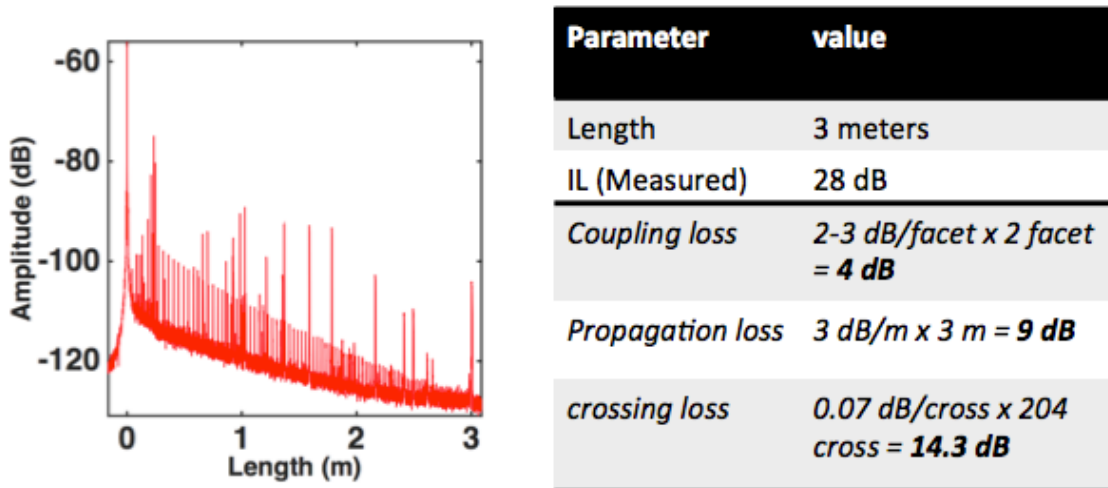
Figure 93: (Left) Coil OBR signal. (Right) Coil measured insertion loss in dB from fiber to fiber and a breakdown of possible sources of loss adding to the measured value.

An insertion loss measurement was performed on the coil, and a total of 28 dB loss was measured from fiber to fiber. Since the major sources of losses were previously quantified (coupling loss, propagation loss, and waveguide crossing loss), a possible breakdown of losses is shown in Figure 93 (Right) which closely matches the insertion loss measurement. If we use this measured waveguide coil with the measured insertion loss of 28dB, then using the model developed earlier in this chapter, this specific coil would have a gyro sensitivity of ~ 3°/√hr, where the assumptions are a 100 mW ASE source power with a RIN of -140

dBc/Hz. The calculated sensitivity includes the un-optimized measured coupling loss where in reality a more monolithic approach is desired via active/passive integration as shown in [5] where the transition loss was around 0.8 dB per transition.

6.6 Conclusion

In conclusion, in this chapter we developed a model for simulating the possible detection limit of a specific optical gyroscope design. The model calculates the minimum detectable rate based on 4 possible sources of phase noise including shot noise, RIN, thermo-refractive, and thermal noise. The model shows that with the state of the art ultra-low loss waveguide platform gyro angle random walk (ARW) of 0.2 °/√hr is achievable classifying it as a rate grade gyro. For a proof of principle an integrated gyro coil was designed on the ULLW platform for possible tactical grade applications. Each individual waveguide coil component was discussed and had its performance measured via test structures. A new waveguide crossing based on an MMI was presented and measured to provide 100x (loss = 0.01 dB/crossing) improvement over a conventional 90° crossing. A 3-meter coil was then measured with waveguide loss of 3 dB/m. With the measured parameters from the coil, the model was used and suggested that a coil ARW of 3°/√hr could be achieved if the coil were to be used as a gyroscope coil. Although the ARW fabricated was not sufficient for a tactical grade gyroscope, the model showed that the optimal gyro length had not yet been reached; thus, making the coil longer (>5 meters) would be sufficient in making a tactical grade optical gyroscope.

6.7 References

[1]   Collinson, R.P.G., "Navigation systems," in Introduction to Avionics Systems, 2003, Springer, New York, pp281-354.

[2]   G. Sagnac, 'L'éther lumineux démontré par l'effet du vent relatif d'éther dans un interféromètre en rotation uniforme', Compte-renduz à l'Académie des Sciences, vol. 95, 1913, pp. 708-10.

[3]   H. C. Lefevre, The Fiber Optic Gyroscope, Artech House, 1993

[4]   Sudharsanan Srinivasan, Renan Moreira, Daniel Blumenthal, and John E. Bowers, "Design of integrated hybrid silicon waveguide optical gyroscope," Opt. Express 22, 24988-24993 (2014)

[5]   Jared F. Bauters, Michael L. Davenport, Martijn J. R. Heck, J. K. Doylend, Arnold Chen, Alexander W. Fang, and John E. Bowers, "Silicon on ultra-low-loss waveguide photonic integration platform," Opt. Express 21, 544-555 (2013)

[6]   L. Zimmermann, G. B. Preve, T. Tekin, T. Rosin and K. Landles, "Packaging and Assembly for Integrated Photonics—A Review of the ePIXpack Photonics Packaging Platform," in IEEE Journal of Selected Topics in Quantum Electronics, vol. 17, no. 3, pp. 645-651, May-June 2011.

[7]   Angus Andrew, "How Good is Your Gyro?," in IEEE Control Systems Magazine, February 2010.

[8]   Lpez-Higuera, Jos Miguel, ed. Handbook of optical fibre sensing technology. Chichester: Wiley, 2002.

[9]   D. Marcuse, "Reflection loss of laser mode from tilted end mirror," in Journal of Lightwave Technology, vol. 7, no. 2, pp. 336-339, Feb 1989.

[10]   Jared Bauters, "Ultra-Low Loss Waveguides with Application to Photonic Integrated Circuits," Ph.D. dissertation, ECE Dept., UCSB, Santa Barbara, CA, 2013.

[11]   Howard R. Stuart, "Waveguide lenses with multimode interference for low-loss slab propagation," Opt. Letters, Vo. 28 No. 22 (2003).

[12]   Heliang Liu, Hwayaw Tam, P.K.A. Wai, Edwin Pun, "Low-loss waveguide crossing using a multimode interference structure," Optics Communications, Volume 241, Issues 1–3, 1 November 2004.

[13]   Hui Chen; Poon, A.W., "Low-Loss Multimode-Interference-Based Crossings for Silicon Wire Waveguides," in Photonics Technology Letters, IEEE , vol.18, no.21, pp.2260-2262, Nov.1, 2006.

Chapter 7

Multilayer Platform for Integrated

Waveguide Optical Gyroscope (IWOG)

Applications

7.1 Introduction

As seen in the previous chapter, for a given waveguide propagation loss the Sagnac phase difference of an IWOG increases directly proportional to the spiral length, while the optical power decreases simultaneously as a function of length reducing the SNR of phase detection. Therefore, an optimal length (L_{opt}) can be defined for a given device in order to achieve the highest possible sensitivity. Provided L_{opt} has not been reached, it is always possible to increase the waveguide gyro sensitivity by increasing the spiral length. With waveguide propagation losses reaching values < 1 dB/m [1] made feasible with the planar waveguide ultra-low loss platform, the gyro optimal length then becomes 10's of meters and therefore the overall size constraints of planar lightwave circuits (PLCs) start to be affected. As a result, a solution must be presented in order to increase waveguide spiral length to keep up with the demanding high sensitivity requirements of gyroscope applications while still maintaining a compact footprint that can be easily integrated into a compact overall package.

The integration approach taken in the previous chapter of a single layer spiral coil is essentially limited by the output bend required to cross all the spiral waveguides at a 90° angle. In order to meet that constraint, the output bend radius must always be ½ of the spiral inner bend radius; consequently, the minimum size a single layer spiral can ever achieve is twice the minimum bend radius, which for the platform previously described would be 2 mm. Therefore, one method of increasing the gyro coil length while still maintaining a small footprint is through the 3D integration (vertical stacking) of waveguides. By incorporating multiple layers, not only is the output bend limitation of the single layer coil removed, but also now we can implement twice the length on a two-layer gyro while maintaining the same footprint as a single layer gyro. Figure 94 shows the total footprint occupied by a single layer gyro (not including the inner bend limitation), and a 2-layer and 3-layer gyro are shown for comparison which essentially provide twice and three times the coil lengths on the same footprint, respectively.
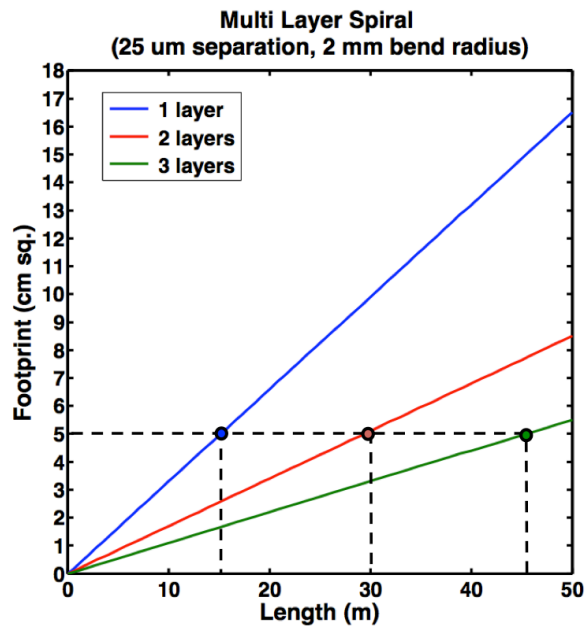
Figure 94: Multilayer gyro coil footprint as a function of coil length. A waveguide separation of 25 μm (to avoid waveguide crosstalk) and a minimum bend radius of 2 mm (to avoid bend loss) are assumed.

It is important to note once more, that although the multilayer spiral coil can provide great footprint enhancement for long delay lines, the gyroscope sensitivity is only improved until the optimal length is reached at which point no additional benefit for gyro sensitivity is achieved until the waveguide propagation loss is further reduced.

In order to vertically stack multiple waveguide layers, two important properties must be considered. First, each layer must be optically connected through a low-loss, and preferably broadband, optical interconnect. Second, each layer must be optically isolated as to avoid crosstalk and crossing loss. In this work, we report on the fabrication and design of optical interconnects for the 3D integration of photonic circuits on the low loss planar waveguide platform for optical gyroscope application.

7.2 Broadband Vertical Coupler

We have previously reported on a multilayer waveguide platform based on vertical directional couplers (DCs) to transfer light from one layer to the other [2]. These vertical directional couplers are equivalent to their counterpart in-plane directional couplers with the exception that the overlapping waveguides in the vertical direction defines the coupling region. The main drawback in using DCs to fully transfer light from one layer to another is that the coupling efficiency is critically dependent on waveguide parameters; as a result, any slight deviation from the nominal design will cause a less than desired amount of power to be coupled between layers and in the end, the uncoupled power will essentially be regarded as power loss and thus degrade the gyro sensitivity. In [2] a beta-mismatch between layers caused by the stress-optic effect changing the effective index of one layer with respect to the other caused the power coupling efficiency to drop by more than 50%! To put the vertical

directional coupler tolerance into perspective, Figure 5.12 shows the required variation to change the coupling efficiency by 10% for a vertical directional coupler if ONLY one critical design parameter was to deviate from the optimal value, where in reality it becomes even more difficult since ALL of the parameters are varying simultaneously.
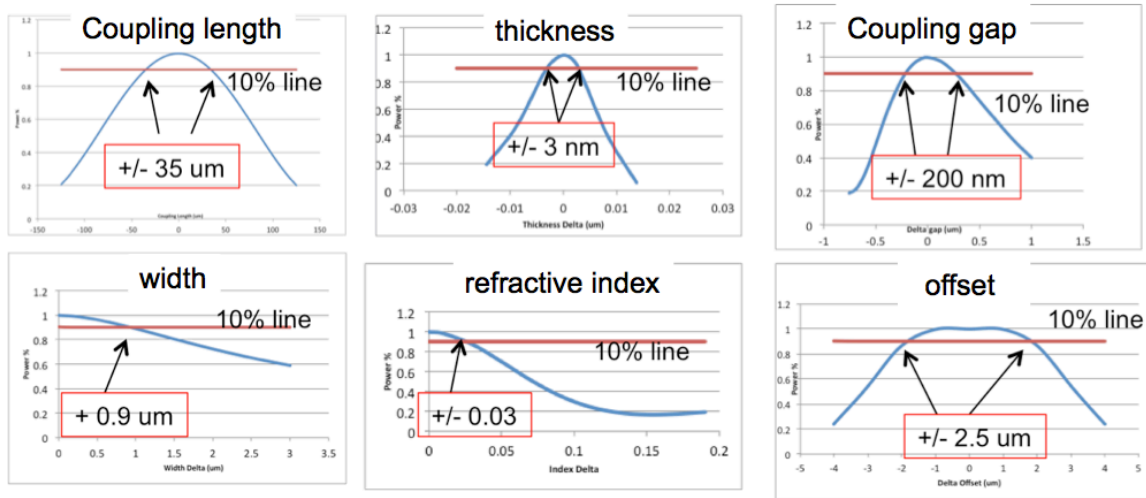
Figure 95: Directional coupler tolerance of several design parameters required to maintain coupling efficiency > 10%. The scans were done by varying a single parameter at a time while maintaining all other constant.

From the figure one can see that a small 0.03 index and a 3 nm core thickness deviation is enough to cause the coupling efficiency to drop by 10%, which in turn are relatively tight tolerances given that the stress-optic coefficient and the high temperature anneal step are enough to cause the index and core thickness to fall outside tolerance simultaneously [2]; since it becomes difficult to properly compensate and continuously predict such effects, an improved vertical coupler with better tolerances must be designed.

Therefore, in order to increase the fabrication tolerance of the vertical directional coupler, an adiabatic laterally tapered vertical coupler was simulated and fabricated as shown in Figure 96. As seen in the coupler diagram, the tapered vertical coupler consists of two overlapping tapers which are tapering in the opposite direction from one another. Important parameters to

consider when designing the tapering coupling region are the taper length, taper tip, and the coupling gap, where all are discussed below.
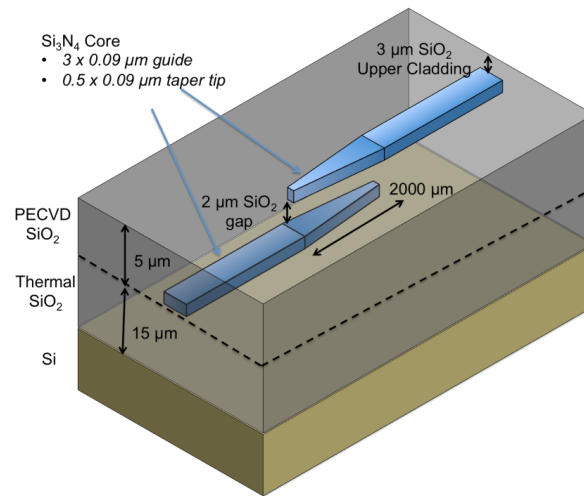
Figure 96: Schematic of adiabatic tapered vertical coupler.

The inverse tapers are linearly varied at a small angle in order to maintain the adiabatic condition, which is primarily a function of taper length and taper tip. By using a finite taper tip we can ensure an adiabatic mode evolution at short taper lengths. In this case, a large taper tip can only be used because the index of refraction difference between each waveguide is small, since the changes are mainly due to process variation. Because using a large taper tip can also introduce reflection due to an index discontinuity, a taper tip of 500 nm was chosen. By introducing the taper along the coupling region, one assures a beta-matching condition along the coupling region even if both layers are velocity mismatched provided that the coupling region is long enough. To demonstrate the index-matching capabilities of the tapered coupler, Figure 97 shows the index of refraction for the top and bottom waveguide for the widths along the taper, where mode coupling occurs at crossover between curves at the index matched condition. In order to show the tolerance of such approach, multiple indices of refraction are used for the top waveguide to simulate velocity-mismatched

waveguides caused by stress-optic variations as previously seen. An index of 1.99 at a wavelength of 1550 nm was assumed for the bottom core and the index of the top waveguide was 1.99, 1.89, and 1.79. As shown in the plot, even with an index variation of 0.2 between waveguides, a beta-matching condition can be still be found providing an indication of a tolerant coupler design.
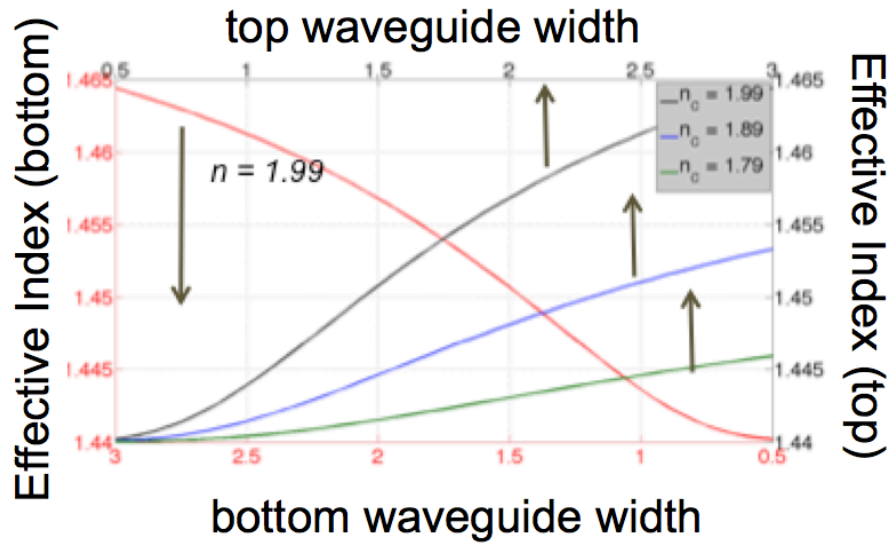
Figure 97: Simulated index of refraction for both coupler waveguides along the taper. The crossing point between curves indicates beta-matching condition and thus coupling. Three different indices are used for to the top waveguide in order to simulate velocity-mismatched waveguides.

Although a beta-matching condition can always be found in such approach, the coupling efficiency is dependent on the taper length as shown in Figure 98a, where a taper of 3 μm oxide gap and 500 nm taper tip was simulated via Photon Design's Eigen mode expansion (EME) algorithm. From the plot it can be seen that a coupling efficiency > 90% can be achieved with a taper length of 250 μm for this specific oxide gap, with efficiencies reaching greater than 98% for 500 μm taper length. It is also important to note that as the beta-matching condition happens only once along the taper, there is no power transfer along the

waveguide after coupling, which is unlike a directional coupler where the power resonates

back and forth between waveguides as a function of length.
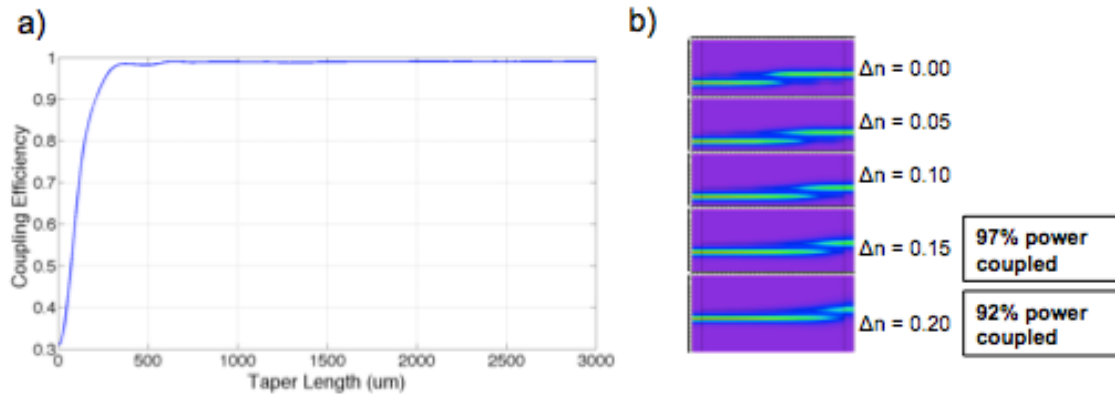
Figure 98: a) Taper coupling efficiency as a function of taper length. b) Simulated field intensity for a 500 um long taper with simulated velocity-mismatch waveguides by changing the index of refraction of one waveguide with respect to the other.

In order to verify the taper tolerance, a similar approach to the effective index scan was taken

where an index difference between both coupler waveguides was introduced to simulate

variations caused by the stress-optic effect. Figure 98b shows the simulated field intensity of

the mismatched waveguides. For the case when the waveguides are perfectly matched, the

coupling happens exactly at the center of the coupling region, but as the index for the top

waveguide changes, it can be seen that the power transfer happens at a different location

supporting the evidence of the index of refraction scan. Because a beta-matching condition

can still be found even when the waveguides are unmatched, this tapered coupler provides a

much greater tolerance than a standard directional coupler as previously mentioned. Figure

99 shows a comparison between the total amount of power that can be coupled between

waveguides as a delta n is introduced between the waveguide cores. As described, the

resonant directional coupler coupling efficiency quickly decays as result of its critical

140

dependence on the waveguide parameters, while the adiabatic tapered coupler decays slowly in comparison to the directional coupler.
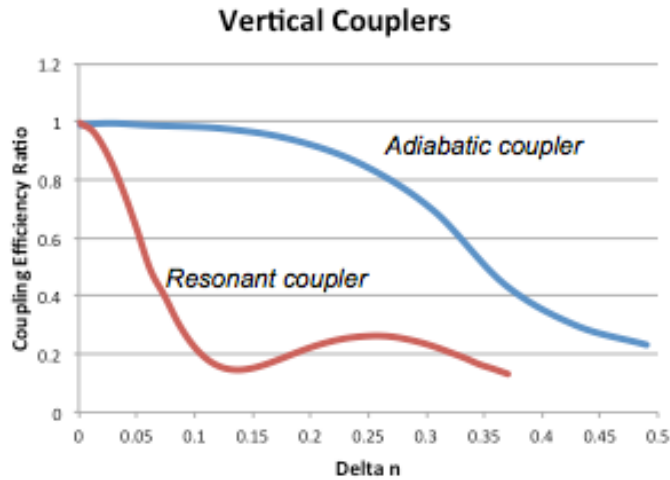
Figure 99: Coupling efficiency of a resonant directional coupler vs. an adiabatic taper coupler as a function of core index of refraction mismatch.

7.3 Multi-layer interaction

In order to lay out a dual layer optical gyroscope coil as shown in Figure 100, where the bottom layer (black) spirals and the top layer (red) spirals out without reversing the rotation orientation, one can see that if footprint is to be conserved the coils in both layers must overlap. Since one layer is spiraling in while the other is spiraling out, it can be shown that the spiral will overlap at a minimum of 2 times during a single loop, and as a result a dual layer gyro will have at least twice the number of crossings as a single layer gyroscope coil. It should also be mentioned that although for a single layer gyroscope coil the crossings can be designed to occur at a 90° angle, that cannot be achieved for a dual layer coil - on the contrary, the crossings are realized with shallow angles.
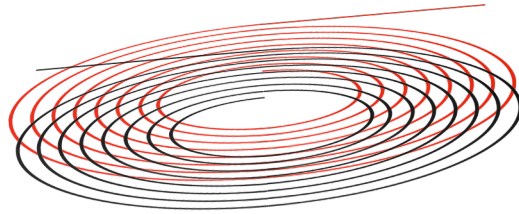
Figure 100: 3D schematic of a dual layer gyro.

Consequently, a multi-layer waveguide platform must then be optically isolated to avoid any unwanted crosstalk between layers during long overlaps, and therefore the optical crossing/overlap on multiple layers was investigated.

The waveguide crossings on two layers vertically stacked were then simulated as a function of angle for multiple waveguide separations; the simulation results are shown in Figure 101, where the inset show the simulated structure. The crossing angles of 30, 15, and 5 degrees were chosen to closely resemble the angle of a dual layer gyro coil. According to the plot, the crossing loss increases as the crossing angle decreases at a fixed waveguide separation, but as the waveguides are placed further apart the crossing loss decreases. As a result, for an angle of approximately 15° the oxide gap (waveguide separation) must be > 4 μm so that the loss per crossing can start to be considered negligible by approaching losses of 0.01 dB/crossing.
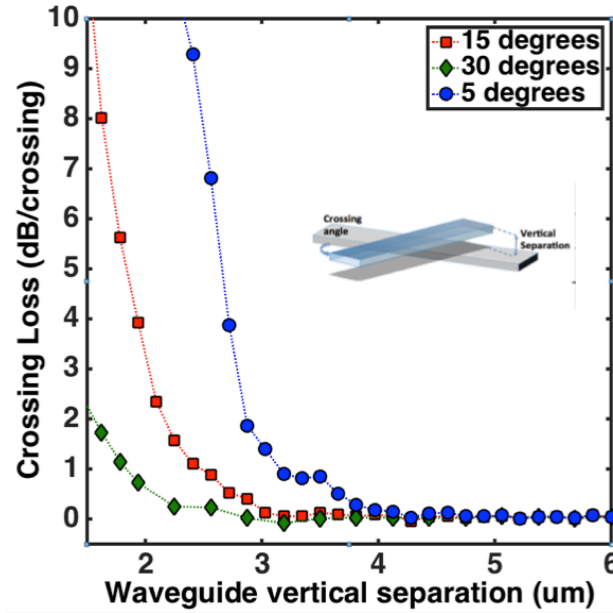
Figure 101: Waveguide crossing loss simulation for a dual waveguide core layer platform.

The next multi-layer interaction to consider is the crosstalk between the bottom and top layer. Once the waveguides cross at a shallow angle, both waveguides overlap for a finite distance before they cross out again, which can essentially cause unwanted coupling evanescently. One way to intentionally avoid such unwanted coupling is by purposely beta-mismatching the waveguides, essentially making a delta beta coupler [3].
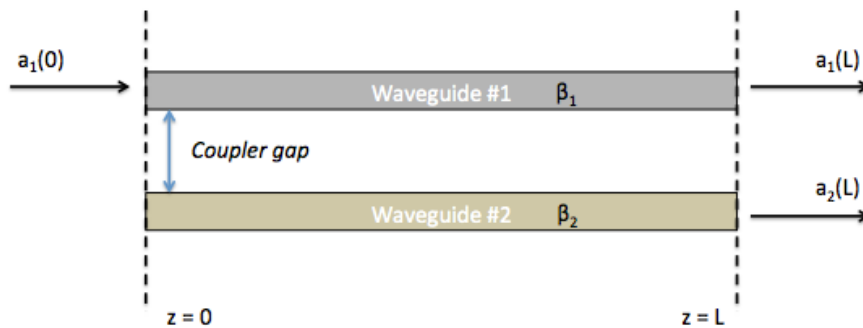
Figure 102: Four port directional coupler.

If we consider a four-port directional coupler as seen in Figure 102 and a single excitation from port 1, then from coupled mode theory [4] we can show that the amount of power coupled from waveguide #1 to waveguide #2 will be:

$$|a_2|^2 = \frac{\kappa^2}{s^2} sin^2(s\,z)$$

where κ is the coupling coefficient, z is the propagation length, and s is defined as

$$s = \sqrt{\left(\frac{\beta_1 - \beta_2}{2}\right)^2 + \kappa^2}$$

where β_1 and β_2 are the propagation constants for waveguide 1 and waveguide 2, respectively. Therefore, when the coupler length is equal to $z = \pi/2s$, usually referred to as the coupling length, the full power from waveguide #1 can be coupled to waveguide #2 provided s equals to the coupling coefficient ($\kappa^2/s^2 = 1$) which can only happen if and only if $\beta_1 = \beta_2$. Since in this case full power transfer is actually considered parasitic coupling, we can vastly decrease the unwanted coupling by assuring that

$$\beta_1 - \beta_2 \gg 2\kappa$$

Because the coupling coefficient is directly proportional to the waveguide separation, as the coupling gap increases the amount of beta mismatch required to guarantee that little to no power is transferred decreases. Since for the dual layer gyro application the waveguides must be placed far away from one another because of the crossing loss, then only a small amount of core mismatch will be required to diminish crosstalk. In order to introduce a difference in propagation constant between waveguides one can change many of the waveguide properties which vary the mode effective index such as: core width, core thickness, core index, and so forth. In the case of the dual layer gyro, a variation in core width was the chosen method to introduce a beta mismatch. In order to verify the feasibility of such approach, the worst-case

144

scenario where the length is set to the coupling length was simulated and plotted in Figure 103. The figure shows the crosstalk as the width of waveguide #2 changes while waveguide #1 width is held constant at 2.8 um. From the plot, when both cores are matched there is 0 dB crosstalk corresponding to a full power transfer, but as the waveguide #2 width increases the crosstalk gets lower. Also, for the same beta mismatch as the gap (waveguide separation) increases, the crosstalk decreases as expected since the coupling coefficient is smaller for a larger separation. To summarize, the optimal waveguide separation to operate a dual layer gyro coil is a 4 um gap, which is sufficient to make crosstalk negligible at -40dB for a 3.2 um waveguide core width difference and at the same time provides low crossing loss of ~ 0.01 dB/crossing.
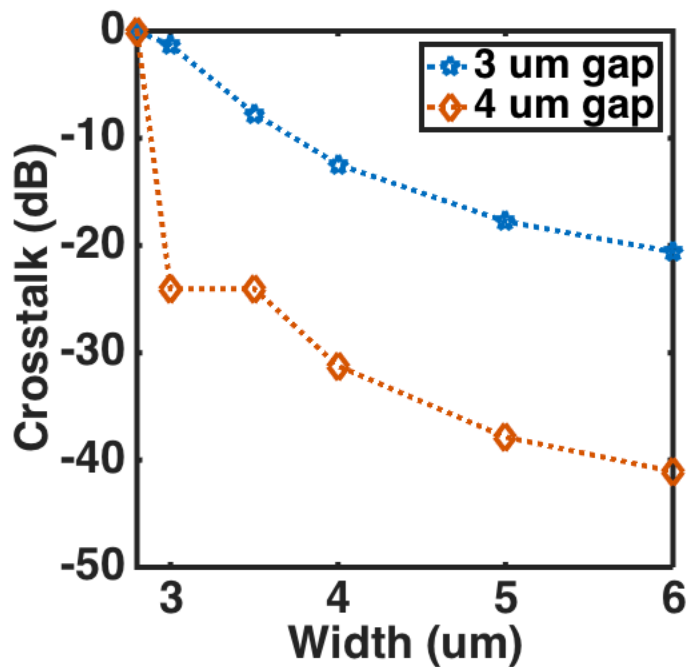
Figure 103: Worst case scenario crosstalk (L= L$_c$) as a beta-mismatch is introduced by varying waveguide width for two different waveguide separation gap (2 and 3 μm). The x-axis corresponds to waveguide #2 width while waveguide #1 width is held constant at 2.8 um and the thickness of both waveguides are equal to 100 nm.

7.4 Fabrication

The dual layer gyro coil together with the dual layer test structures were fabricated in a similar manner as described in the platform fabrication section. To quickly summarize, the devices were fabricated using 248nm stepper lithography on a 4 inch Silicon wafer. The lower cladding is made up of 15 um of thermal SiO_2 (n = 1.45 at 1550 nm), where the thickness was chosen to make substrate leakage negligible. The first waveguide core is then formed via LPCVD deposition of stoichiometric Si_3N_4 (n = 1.99 at 1550 nm) and covered with high-density PECVD (HD-PECVD), which serves as the coupling gap between waveguide layers where the thickness is varied accordingly. The next core is then deposited identically to the first core and covered with an additional upper cladding of HD-PECVD SiO_2 of typically 3 um thickness for the final device completion. Each film is annealed separately to remove hydrogen impurities right after deposition at 1050 °C for 7 hours. Figure 104 shows the cross-section SEM of a typical finished 2-layer platform device.
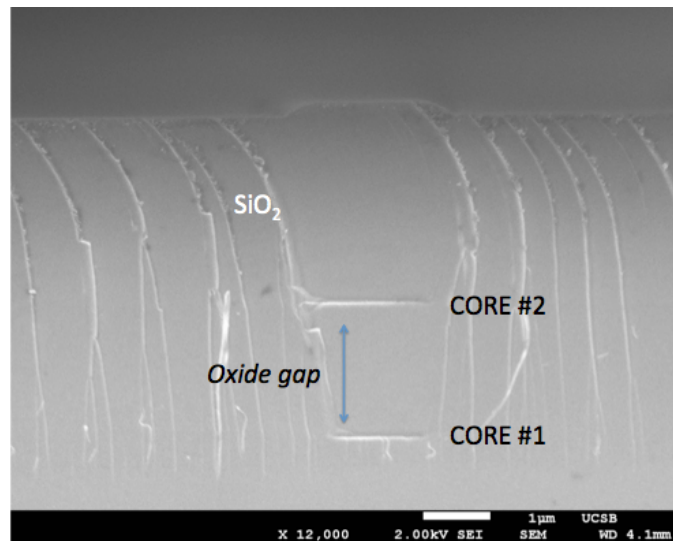
Figure 104: An SEM image showing the fabricated two layer platform highlighting both waveguide cores separated by an oxide gap. Striations on the cladding are due to cleaving.

One of the many challenges when it comes to fabricating a multi-layer platform is dealing with the residual stress from the multiple layers. The residual stress not only affects the device level performance via the stress-optic effect, but it also affects fabrication level performance through film cracking, delamination, and substrate bow, which can all be linked to film stress [5]. Stress in thin-film can be separated into intrinsic stresses which are growth stresses and extrinsic stress which is a result of unintended external force. Since the effect of the residual stress on the device level performance has been addressed via the design of a tolerant tapered vertical coupler in the previous section, here we mainly address the influence of residual stress in the fabrication process. One of the most common types of extrinsic stress is the thermal stress caused by the mismatch of the thermal expansion coefficient of the films when exposed to temperature changes. The thermal expansion coefficients for the materials used on this platform are shown in Table 8, and from the table we can see that the largest mismatch comes from the oxide compared to the remaining materials which have an order of magnitude less mismatch.

Material	Thermal Expansion coefficient - Linear ($°C^{-1}$)
Silicon (Si)	2.6×10^{-6}
Silicon Dioxide (SiO$_2$)	5.5×10^{-7}
Silicon Nitride (Si$_3$N$_4$)	3.3×10^{-6}

Table 8: Thermal expansion coefficient for all materials used on the multi-layer platform.

Given the high temperature anneal required to drive out the hydrogen impurities in each film, which as previously shown is a major source of absorption loss, this large amount of mismatch can cause a large amount of wafer bow and film cracking. For the typical thicknesses required for fabricating the multi-layer gyro coil presented here, film cracking

and delamination were not seen, but instead the main source of detrimental effect was aroused from the wafer bow. Substrate bowing is a serious issue which impacts wafer handling, etch and photolithography uniformity, where many cleanroom tools have a maximum wafer bow requirement. For a more in-depth discussion on thin-film stress, please refer to the stress section in the platform chapter; here we are mainly concerned in compensating for film stress in order to reduce wafer curvature. It is important to mention, that even in the absence of structure failure, the mechanical response of the thin films are still affected by the residual stress.

Wafer bow is measured as the deviation from a flat wafer, usually calculated from the center to the edge as shown in Figure 105. For convention, a negative bow will be considered as a tensile stress while a positive bow is compressive.
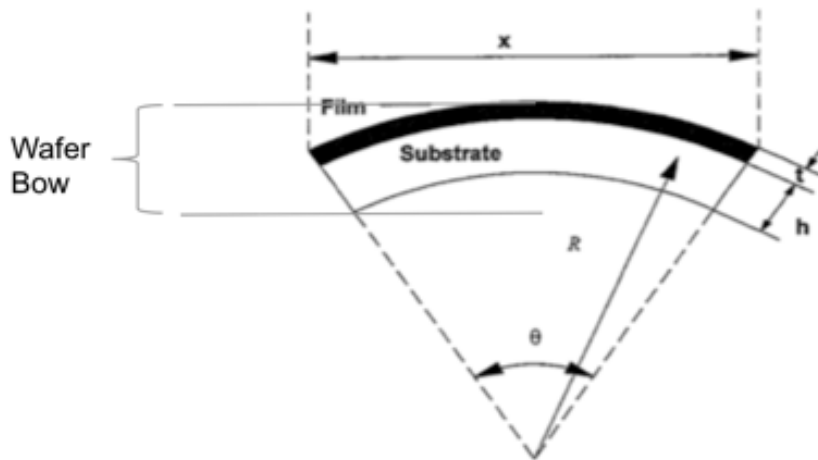
Figure 105: Wafer bow definition. R is radius of curvature, x is wafer diameter, t is thin-film thickness, and h is substrate thickness.

Therefore, film stress can be related to wafer curvature through Stoney's equation as seen below [6].

$$\sigma = \frac{Eh^2}{(1-v)6Rt}$$

where σ is the wafer stress, E is the Young's Modulus of the substrate, ν is the Poisson's Ratio of the substrate, h is the substrate thickness, and R is the radius of curvature. The quantity $E/(1-\nu)$ is often referred as the biaxial modulus, which comes from a special case of plane stress where the x and y stresses along the principal axis are equal. One way to compensate for wafer bow is through the application of a high stress film to the back of the substrate with equivalent type of stress. The purpose of using a high stress film is to reduce the amount of film required to fully compensate the substrate bow, as film stress is inversely proportional to film thickness. The film applied to the back of the substrate will apply a force in the opposite direction of the top film and if the forces are fully matched the substrate bow will be essentially compensated, where this approach was successfully performed in [7]. The main drawback of the compensation by depositing on the wafer backside is that it requires placing the final device upside on a deposition tool therefore increasing the chances of impurities and scratches to be introduced onto the device. Therefore, in order to avoid substrate bow altogether a thicker substrate can be used since from Stoney's equation the radius of curvature is directly proportional to substrate thickness h. The main drawback for such approach then becomes the fact that since the substrate cannot bow as a result of the thermal expansion, this will essentially lead to mechanical failure depending on the overall film thickness/stress. For the dual layer gyro coil presented here where the overall bow caused by all the layers is typically < 100um, a 1 mm 4" Si substrate can be used without any film delamination or cracking. If more than 2 layers are required, further investigation must be done in order to reduce the film stress to avoid mechanical failure.

7.5 Results

All the devices discussed here such as the dual layer and the broadband vertical coupler were fabricated and tested together with other test structures to analyze waveguide crossing and crosstalk. All of the device results are presented below.

7.5.1 Broadband vertical coupler

In order to measure the coupling efficiency of the taper coupler from waveguide #1 on the bottom layer to waveguide #2 on the second layer, a cutback test structure as shown in Figure 106 was fabricated. The test structure consisted of waveguides with 0 (straight waveguides), 2, 4, and 6 transitions between layers. By plotting the insertion loss as a function of the number of taper transitions, the taper loss can be extracted from the slope of a linear fit through each measured point at a specific wavelength.
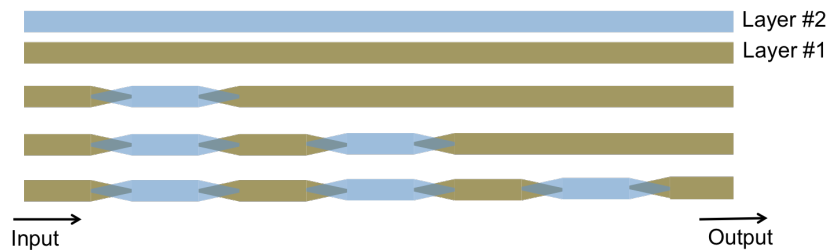
Figure 106: Cutback test structure used to measure taper vertical coupler coupling efficiency. Blue waveguide represent the top core layer, and brown waveguide represents bottom waveguide layer.

An oxide gap of 3 um was used as the vertical separation between the waveguides. A taper of 500 nm was used, and 3 test structures were made corresponding to taper lengths of 250, 500, and 1500 um. The overall waveguide geometry was single mode and had a width of 2.8 um and a 90 nm thickness. The top view of the fabricated coupler (250 um) can be seen on the optical microscope image in Figure 107 together with the measurement setup.
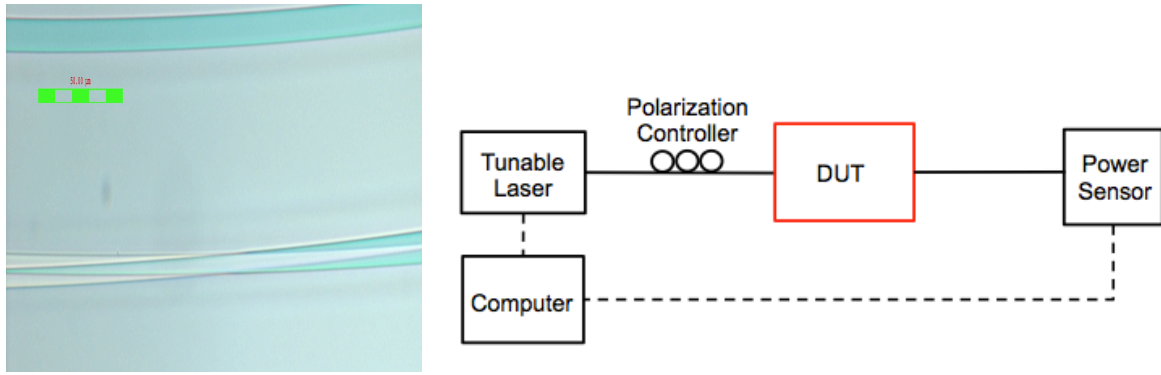
Figure 107: Microscope image of a fabricated dual layer taper coupler with taper length of 250 um. (Bottom) Measurement setup.

In order to test the devices, light was coupled in and out of the test structures using a pair of lensed fibers with a 5 um spot size where the input polarization was controlled to be transverse electric (TE) via a 3-paddle polarization controller. A tunable laser source was used as the input signal, where the wavelength was swept from 1520 to 1600 nm, and a broadband InGaAs detector was used for power measurement. The wavelength scan measurements for a 1,500 um long taper are shown below in Figure 108.
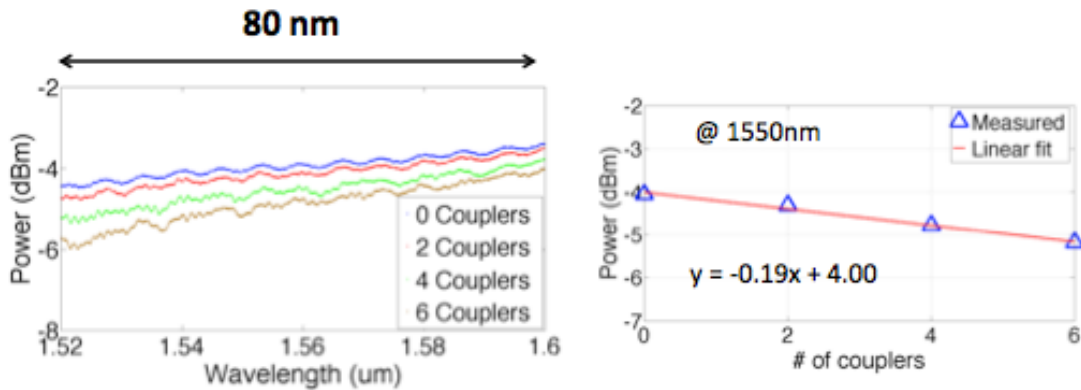
Figure 108: (Left) Adiabatic taper coupler test structure wavelength scans. (Right) Linear fit to extract single coupler loss at a single wavelength (1550 nm).

The wavelength scan from the adiabatic taper test structure is nominally flat from 1520 nm to 1600 nm corresponding to at least an 80 nm bandwidth. The large bandwidth is a direct result

of the beta-matching ability of the coupler, especially for a long taper as shown here of 1500 um in length. In order to calculate the coupler loss for a single wavelength, the data point at the desired wavelength must be extracted and plotted for the multiple number of couplers as shown in Figure 108 (Right) for the case of 1550 nm. By performing a linear fit through all the data points, the slope of the line gives the total loss per coupler while the y-intercept provides all the system losses including coupling loss and waveguide loss. The plots in Figure 108 have already been normalized to have the system losses removed, and as a result the y-intercept in this case corresponds to the coupling loss for 2 facets only (assuming propagation losses are negligible due to the short waveguide length for the test structures). Therefore, by extracting the parameters from the fit provided, which has a coefficient of determination (R^2) value of 0.987, the adiabatic taper coupler has a **coupling loss at 1550 nm of 0.19 ± 0.10 dB**, where the error bars are a direct result of the coupling uncertainty. For this platform the coupling losses of the diced facet also corresponds to 2 dB per facet without polishing.

The same analysis can be done for multiple wavelengths, and by looking at the wavelength scan a wavelength dependence is definitely clear, where longer wavelengths will have lower coupling loss. By fitting the data at both ends of the scan, the coupler is shown to have a **coupling loss of 0.21 dB at 1520 nm and 0.11 dB at 1600 nm**. In order to verify that the taper design was indeed low loss and not simply 'blasting' through the cladding without coupling through the second layer, a test structure was fabricated where no second cladding was placed and the transmission measured. For the case without the top core the transmission was measured to be below -25dBm, thus affirming the low coupling loss of the adiabatic taper couplers presented here. The remainder of the test structures containing multiple taper

lengths were measured and the results displayed in Figure 109. The results are shown to closely match the simulation values.
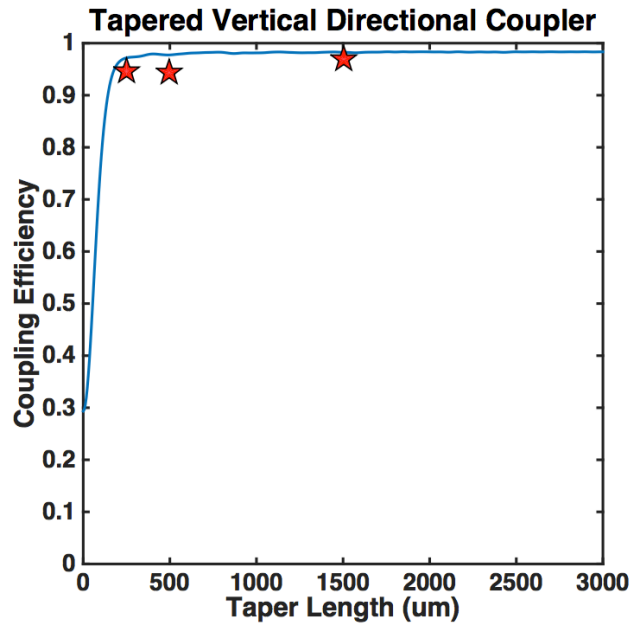
Figure 109: Adiabatic taper vertical coupler measured coupling efficiency for three different lengths measured at 1550nm. Red starts represent measured data, while the solid line shows simulation based of the values of the fabricated tapers.

7.5.2 Waveguide crossing

The waveguide crossing loss on multiple layers was determined in a similar fashion to the adiabatic taper coupler loss. A cutback crossing test structure, as seen in Figure 110, was fabricated. The test structures consisted of three different angles of 5, 10, and 15 degrees, which closely resemble the crossing angle on a dual layer gyroscope coil. For each crossing angle there were a total of 0 (straight waveguide), 5, 10, and 15 crossings. The waveguide geometry for the input waveguide and the crossings were both 2.8 um (width) x 90 nm (thickness), and no beta mismatch was considered at this time. To determine the crossing loss dependence on the waveguide separation, two nominal thicknesses for the oxide gap were deposited: 2 and 3 μm.

153
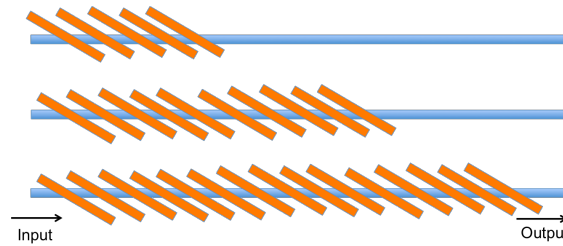
Figure 110: Cutback multi-layer crossing test structures. Blue represents the bottom waveguide while oranges represents the top waveguide on a different layer.

An identical setup used for the coupler measurements was used for the crossing loss measurements, and an example of the wavelength scan with the cutbacks data points for a wavelength of 1550nm are shown in Figure 111. From the wavelength scan measurements, the waveguide crossings show no wavelength dependence in the 80 nm bandwidth swept making the crossing loss wavelength-independent. The scan shown here corresponds to a crossing angle of 30° at a nominal oxide gap of 3um, and therefore from the data points extracted at 1550 nm, the crossing loss for that specific angle and separation corresponds to 0.40 dB per crossing. One thing to note on the cutback measurement provided is that the data was not normalized, and therefore the power level and y-intercept includes system loss, coupling loss, and waveguide loss.
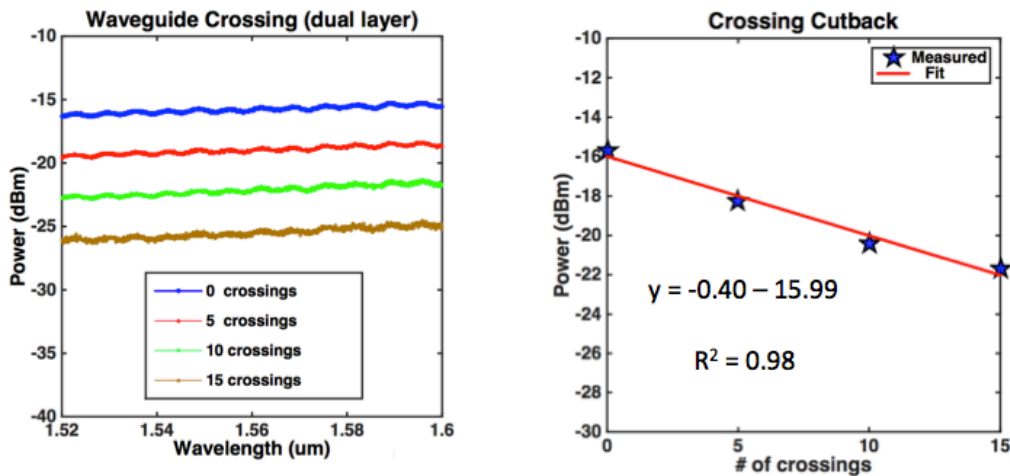
Figure 111: (Left) Example of wavelength scans for crossing loss cutback test structure corresponding to a 30-degree crossing. (Right) Crossing loss cutback points at 1550nm, showing linear fit and R square value.

154

Similar data was taken for all the crossing angles and since the wavelength scan shows no wavelength dependence, all of the linear fits were done for the data points at a wavelength of 1550 nm only. All of the measurements performed provided data of similar characteristics to Figure 111 above and all had an R squared value > 0.9. All the measured waveguide crossing losses for the 2-layers platform are compared to the simulation results and the comparison is displayed in Figure 112.
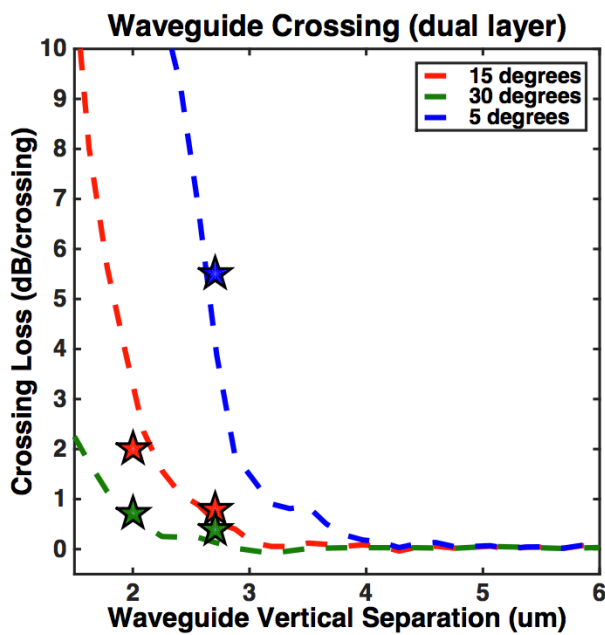
Figure 112: Simulated (dashed lines) and measured (stars) crossing loss for multiple crossing angles and waveguide separation.

Although the nominal thicknesses chosen for the waveguide separation were 2 um and 3 um, a deposition calibration error caused the 3 um oxide thickness to be 2.7 um; therefore, all data was adjusted accordingly. The measured data closely matched the simulation results, and the measured values are summarized in Table 9 below. The value for the 5° crossing was too high to measure making the transmission signal for 5 crossings or more fall below the photodetector noise floor. As it was shown with the simulations and confirmed with the

measurements, in order for the dual layer optical gyroscope to be able to maintain low crossing loss, an oxide gap of 4 μm would be required to make the crossing loss < 0.01 dB per crossing.

Gap	30°	15°	5°
2.0 μm	0.7 dB	2.0 dB	-
2.7 μm	0.4 dB	0.8 dB	5.5 dB

Table 9: Summary table of measured crossing loss values.

7.5.3 Dual Layer Waveguide Spiral

In order to verify the use of the broadband coupler for the dual layer optical gyroscope application, two photolithography masks were laid out which contained three different types of 2-layer spirals as well as many test structures presented here. The mask's GDS layout can be seen in Figure 113 below.
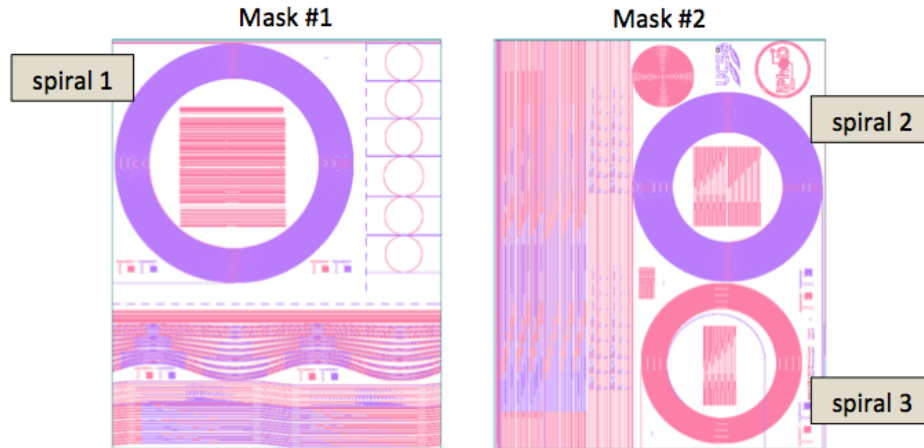
Figure 113: GDS layout for dual-layer gyro coil and test structures. Mask #1 is a set of masks for both layers, and the same applies for Mask #2.

Mask #1 and Mask #2 were each a set of 2 masks corresponding to layer 1 and layer 2 for a total of 4 photo masks. In the figure above, layer 1 (bottom layer) is represented by the pink color structures while the purple structures represent layer 2 (top layer). Each mask was 21 x

26 mm in dimension and was designed for the 4x ASML 248nm DUV stepper. Spiral 1 highlighted in mask set #1 corresponds to a 4-meter dual layer spiral where each layer has a 2-meter overlapping spiral. A large beta-mismatch to reduce waveguide crosstalk was introduced by varying the waveguide width of the bottom layer with respect to the top. Spiral 1 had a waveguide width of 7 μm for the bottom layer while the top was 5 μm in width. Spiral 2 on mask set #2 was 3 meters in total length corresponding to 1.5 meters of propagation on each layer of overlapping spiral as well. Spiral 2, contrary to spiral 1, had only a small beta mismatch between waveguides. The bottom layer of spiral 2 was 7.0 μm in width and 7.5 μm for the top layer. Spiral #3 on the other hand is 1 meter in length and only has a spiral for the bottom layer while the top layer is used for the output waveguide only, which crosses through the spiral at a 30° angle in a similar fashion to the single-layer gyro coil from the previous chapter; a larger beta-mismatch is used for spiral #3. All layers were nominally 100 nm in thickness and although some waveguide geometries correspond to a multi-mode waveguide, only the fundamental mode was excited via an adiabatic taper at the input.

	Spiral #1	Spiral #2	Spiral #3
Mask	1	2	2
Length (total)	4 m	3 m	1.0 m
Layer 1 length	2 m	1.5 m	1.0 m
Layer 2 length	2 m	1.5 m	Output only
WG width layer 1	7.0 um	7.0 um	7.0 um
WG width layer 2	5.0 um	7.5 um	4.0 um
Core thickness (layer1/ layer2)	100 nm/100nm	100 nm/100nm	100nm/100nm
Taper length	2000 um	2000 um	2000 um

Table 10: Summary of dual layer spiral test structures with important design parameters listed.

A summary of each spiral design can be found in Table 10 above. All the spirals listed here can be used for optical gyroscope applications since no change in direction is done through

an s-bend; instead, the bottom spiral is used for spiraling in while the top spirals out, or vice and versa depending on the input direction. The coupler used to transfer the power from the bottom layer to the top layer was the adiabatic taper coupler, which as simulations show is tolerant enough to overcome the large beta-mismatch introduced to avoid crosstalk. The coupler design had a 500 nm taper tip and a 2000 μm taper length. The longer taper length was chosen to give the flexibility of using a large waveguide separation between layers through a thick oxide gap. As previously stated, a thicker oxide gap will provide lower crosstalk as well as lower crossing loss with the trade-off of a smaller coupling coefficient, thus requiring the coupler to be much longer in order to achieve the high coupling efficiency desired of > 90%. All the samples fabricated for the purpose of testing the dual layer core spiral had an identical process as described in the fabrication section and a 3 μm separation gap was used for the entire spiral coil fabrication. Figure 114 shows the end result of a fabricated dual-layer chip (mask #2) under test with input fiber on the right.

Figure 114: Picture of fabricate 2-layer core. Spiral 2 and Spiral 3 are shown here.

In order to characterize each individual fabricated 2-layer spiral, an optical frequency domain reflectometry (OFDR) approach was used as described previously. In summary, the OFDR

158

technique is the frequency-domain equivalent of an optical time domain reflectometry measurement but instead of using light pulses which would limit the measurement resolution to the pulse width, OFDR uses a swept-laser source and resolutions of 10 μm can instead be achieved (Derickson). An OFDR measures the backscatter and backreflected light from the device under test (DUT). The backscatter light can therefore provide information about reflections, attenuation, and losses along the fiber and DUT. An OFDR measurement will usually consist of a sloped line representing the backscatter signal with some propagation loss, spikes which are due to reflections, and steps corresponding to insertion loss. Because OFDR measures backscatter light, by fitting a line to a backscatter signal of an OFDR measurement we can extract the round-trip loss of the DUT by finding the slope. If the slope of the line is divided by half to compensate the round-trip aspect of the measurement, then the device's propagation loss can be found. In order to properly calibrate the measurements to know the distance between two reflections and to properly calculate the propagation loss, the group index must be known. Therefore, in order to calibrate the measurements, a test structure of a known distance was measured using the OFDR technique and the group index calculated from the measured time data. To measure the backscatter signal of the dual layer spirals, a commercially available OFDR tool was used from Luna technologies called the Optical Backscatter Reflectometer (OBR). The OBR is able to perform the OFDR measurements with a sensitivity of -130 dB and a spatial resolution of 10 μm between two points, which is enough for measuring the waveguide backscatter level together with any reflections caused by the waveguide crossings.

Spiral #1 which consisted of a large beta mismatch and a 3µm oxide gap, was measured via OFDR and the backscattered data results shown in Figure 115 below on the top-left and bottom-left corner each correspond to an input at the two different layers.
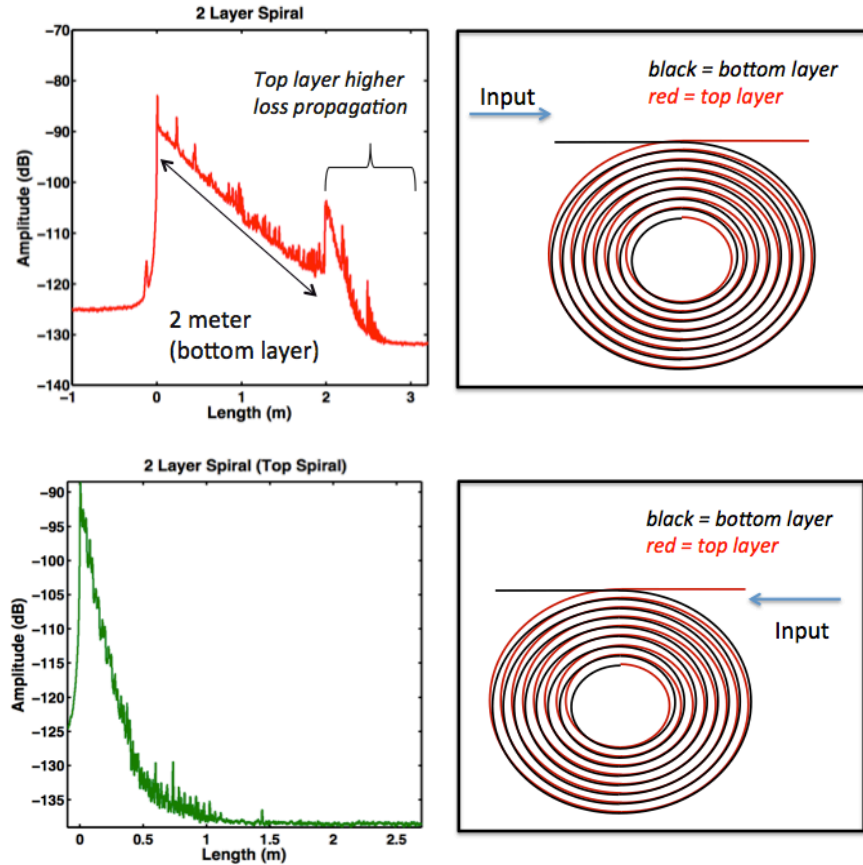
Figure 115: (Top-left) OFDR measurement of a dual layer 4-meter spiral. The backscatter signal has two sections of different slopes representing the loss in layer1 and layer2. The measurement is done by coupling light through the bottom layer first as shown in the schematic on (top-right). (Bottom-left) OFDR measurement by coupling light through the top layer first as indication by the schematic on (bottom-right).

The top-left red backscatter plot shows the measurement when the bottom layer is used as the input waveguide layer. From the figure a few spikes are seen randomly throughout the spiral length which is indicative of fabrication imperfections corresponding to a single scatter point but because of the large beta-mismatch used, no large reflection/loss corresponding to waveguide crosstalk was seen. The data can also observed to have two distinct slopes, one from 0 to 2 meters and the other from 2 meters on. Since the 2-layer spiral was designed to

160

have a total of 2 meters propagation on each layer, the two different slope sections correspond to the two different waveguide layers. As a result, from the data measured the top layer is shown to have a higher propagation loss when compared to layer 1, and the light only propagates approximately 0.5 meters on the second layer before falling into the noise floor of the equipment. Consequently, in order to extract the information from the second layer alone, the same measurement was done but with the input layer being the second layer, as indicated by Figure 115 (bottom-right). From the second measurement, data shown as the green backscatter plot in Figure 115 (bottom-left), the top layer is confirmed to have a higher loss than the bottom layer, and measurement 1 and measurement 2 are in perfect agreement providing identical slopes for layer 2. The slopes can then be measured and the propagation loss extracted. Since the OBR provides the frequency domain data, a narrow-frequency window can be applied to the entire data in stepped frequency so that the slope can be found for each narrow band and the loss found as a function of wavelength. The results of propagation loss for the coil given from such measurements are shown in Figure 116 (left). The backscatter plots indicated the top layer has a much greater loss when compared to the bottom layer; the lowest losses for the top and bottom layer are 40 dB/m and 7 dB/m, respectively. Although the losses on the second layer are much higher for this device, the OFDR measurements show definite coupling between layers and some propagation of the second layer, confirming the functionality of the adiabatic taper coupler for a large beta-mismatch otherwise not feasible with a conventional directional coupler. Spiral 1 therefore confirms the feasibility of the platform for the applications of a dual layer IWOG coil, provided that the losses of layer 2 can be explained and lowered.
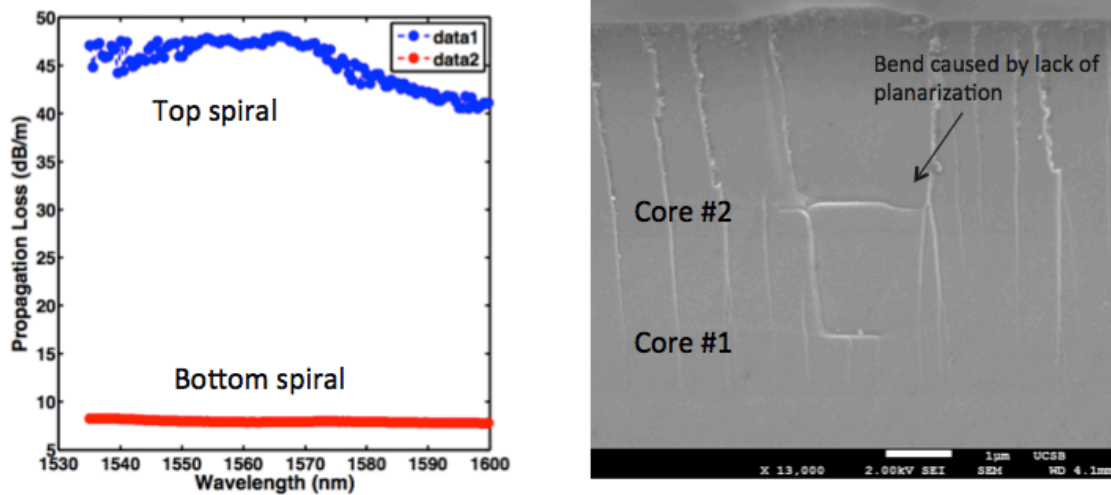
Figure 116: (Left) Wavelength dependent loss for the top and bottom layer of the dual layer spiral 1 extracted from the OFDR measurements. (Right) Cross-section of two overlapping cores of the dual layer spiral showing a waveguide bend due to a lack of planarization.

In order to attempt to determine the cause of high propagation loss for the top layer, the 2-layer coil spiral 1 was cleaved through the waveguides and the waveguides were inspected under a scanning electron microscope (SEM). Upon investigation of the SEM image, the cause of the higher propagation loss was clear. During the fabrication procedure a lack of planarization between core #1 and core #2 caused the top spiral to go through a series of undulations every time it overlapped with the bottom layer. This effect can be clearly seen from the SEM image in Figure 116 (right), where the top wider core shows two bends on each side of the narrower bottom core during the overlap. Because the optical mode of the low-loss planar waveguide platform is weakly guided, such bending causes a major source of propagation loss for the second layer. Therefore, the lack of planarization can be easily solved by the addition of a chemical mechanical polishing (CMP) step after the oxide gap deposition.

Spiral 2 was fabricated in order to determine the effect of the amount of beta-mismatch on the waveguide reflection/loss resulting from the crossing loss and crosstalk. Spiral 2 was

fabricated identically to spiral 1 with the same amount of oxide gap providing 3 μm of separation between waveguides and no planarization step between core depositions. Spiral 1 and Spiral 2 were only different in length and beta-mismatch between layers, which was introduced as a change in waveguide width. Spiral 1 had Δwidth between layers of 2 μm while spiral 2 had a Δwidth of 0.5 μm, where according to the simulations shown in Figure 103 such differences in Δwidth correspond to a difference of -10 dB in crosstalk. Since spiral 2 had no planarization between cores, the OBR measurement was performed with the input on the first layer and the OBR data screenshot is shown in Figure 117 below.
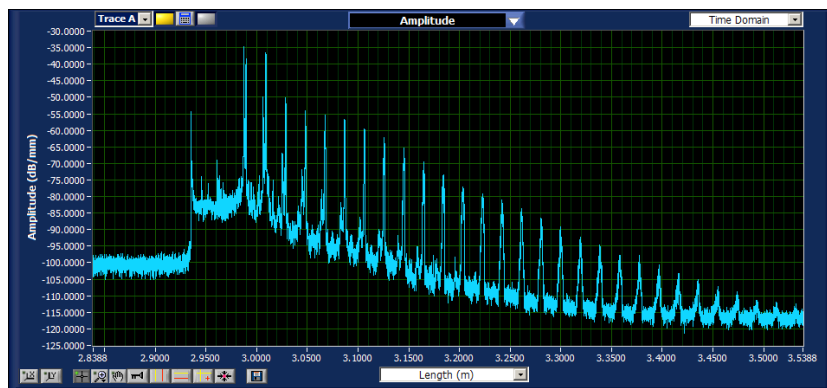
Figure 117: OBR data screenshot of spiral 2 displaying the effect of a small beta-mismatch between waveguides.

By analyzing the OBR plot, a great amount of layer interaction is visible especially when compared to the spiral 1 data. As the light propagates through the bottom spiral, every time it comes through a crossing a small amount of power is coupled into the top waveguide which is seen as a spike on the OBR plot. The spikes on the OBR plots are actually very small amounts of higher backscatter signal due to core undulation on the top layer and not from reflections which have a very sharp distinct signature. The spiral propagation loss for spiral #2 was not extracted due to its sharp decline into the OBR noise level. Although the crosstalk and propagation loss was not quantified for spiral 2, by comparing the data of spiral 1 and

spiral 2 one can see the drastic improvement in waveguide propagation as a direct result of beta mismatch.

To conclude the dual layer spiral coil experiments, spiral #3 was fabricated according to the schematic shown in Figure 118. As with the previous 2 spirals, this 2-layer coil was fabricated similarly with a 3 μm waveguide separation. The second layer was used only to provide the waveguide output, and the waveguide crossings were done at an angle of around 30°. By placing the waveguide crossings on the second layer, as opposed to the single layer spiral presented on the previous chapter, the reflections from the waveguide crossings can be mitigated to improve the gyro performance in comparison to the single gyro approach.
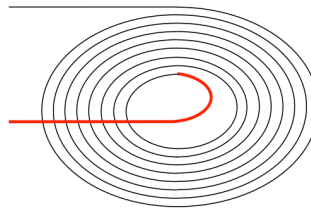
Figure 118: Schematic of spiral #3. Black line represents bottom layer, Red line represents top layer.

The spiral was measured with the OBR and the resulting data is shown in Figure 119. As expected and shown in the plot, each waveguide crossing reflection is still seen in the backscatter data but instead the peaks are at a much lower amplitude level when compared to the single layer gyro. The reflections can thus be reduced diminishing the optical gyro noise and improving sensitivity by using a multi-layer waveguide platform. Although the crossings still have some loss, because the index discontinuity (waveguide crossing) is on the second layer most of the loss is to random scattering and not reflected power. The improvement becomes clear when the figure below is compared to the single layer gyro coil in the previous chapter. Although no footprint enhancement was gained, with this approach the return loss of each crossing can be drastically reduced.

Figure 119: OBR backscatter data for spiral #3 which has a spiral on the first layer and only the output on the second layer. The data shows the decrease of reflections when compared to a similar single-layer spiral coil.
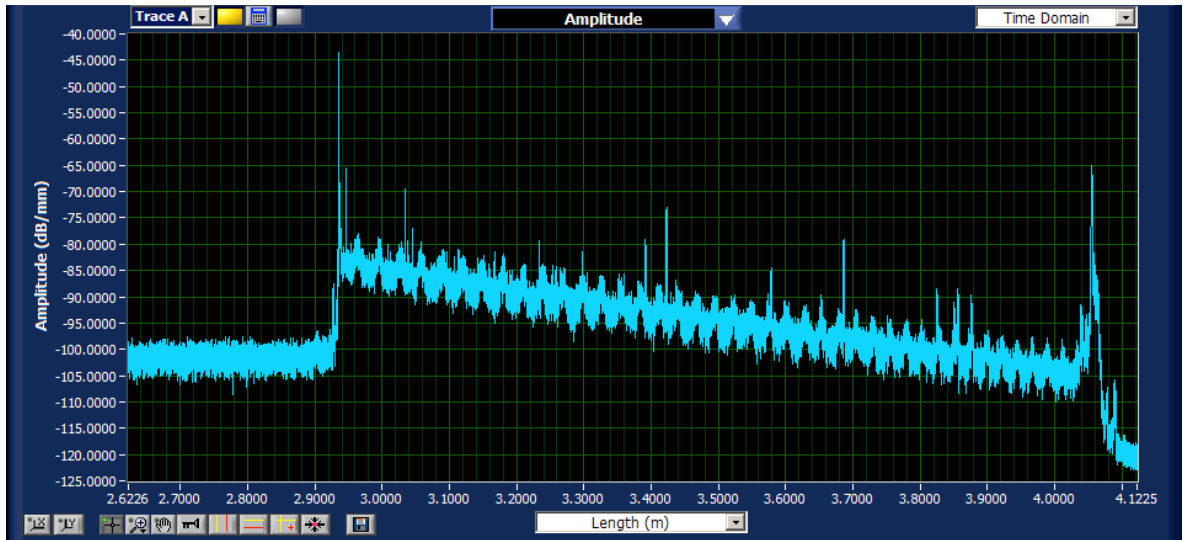
7.6 Summary and Conclusions

In this chapter, we discussed a novel multi-layer waveguide platform on the low-loss high aspect ratio Si_3N_4 core for use in integrated waveguide optical gyroscope (IWOG) applications. A broadband and tolerant adiabatic vertical coupler was designed, fabricated and measured to have very high coupling efficiency with losses of < 0.2 dB per transition measured over 80 nm. The layer interaction was then simulated and tested for waveguide crossing loss and waveguide crosstalk. Measurements of waveguide crossing loss closely matched the simulation results which predict crossing loss of < 0.01 dB per crossing for a 4 μm vertical waveguide separation. We also investigated purposely introducing a beta-mismatch between both layers in order to decrease the amount of parasitic coupling (crosstalk) and only coupling through the tolerant tapered vertical coupler. Multiple 2-layer spirals were fabricated and tested. Backscatter measurement results show full coupling between layers verifying the functionality of the adiabatic taper coupler for velocity-

mismatched layers. Therefore, a dual layer waveguide platform has been demonstrated with spiral structures that can be used for IWOG applications. Although coupling was demonstrated between two vertical layer, the top layer was shown to have higher propagation losses due to a lack of planarization between waveguide layer, which can be solved through the addition of a chemical mechanical polishing step (CMP) between waveguide core depositions.

7.7 References

[1] Jared F. Bauters, Martijn J. R. Heck, Demis D. John, Jonathon S. Barton, Christiaan M. Bruinink, Arne Leinse, René G. Heideman, Daniel J. Blumenthal, and John E. Bowers, "Planar waveguides with less than 0.1 dB/m propagation loss fabricated with wafer bonding," Opt. Express 19, 24090-24101 (2011)

[2] D. D. John et al., "Multilayer Platform for Ultra-Low-Loss Waveguide Applications," in IEEE Photonics Technology Letters, vol. 24, no. 11, pp. 876-878, June1, 2012.

[3] J. P. Donnelly, L. A. Molter and H. A. Haus, "The extinction ratio in optical two-guide coupler Delta beta switches," in IEEE Journal of Quantum Electronics, vol. 25, no. 5, pp. 924-932, May 1989.

[4] Coldren, Larry A., Scott W. Corzine, and Milan L. Mashanovitch. Diode lasers and photonic integrated circuits. Vol. 218. Wiley. com, 2012.

[5] Stephen Campbell, "The Science and Engineering of Microelectronic Fabrication," 2nd ed. Oxford Univ. Press, Oxford, 2001.

[6] Maria Rosa Ardigo, Maher AHMED, Aurélien Besnard. Stoney formula: Investigation of curvature measurements by optical profilometer. Advanced in Material research., 2014, 996 (IX), pp.361-366.

[7] D. T. Spencer, M. Heck, R. Moreira, J. T. Bovington, J. E. Bowers, A. Leinse, H. H. v. d. Vlekkert, R. G. Heideman, M. Hoekman, and T. T. Veenstra, "Integrated single and multi-layer Si3N4 platform for ultra-low loss propagation and small bending radii," in Optical Fiber Communication Conference, OSA Technical Digest (online) (Optical Society of America, 2014), paper Th1A.2.

Chapter 8

Summary & Future Directions

8.1 Summary

In this dissertation, we built upon the ultra low loss world record waveguide platform developed at UCSB and first presented in [1]. Since the platform's first demonstration, multiple building blocks have been developed. Figure 120 shows the platform evolution from its development to the demonstration of the following components: spirals [2], polarizers [3], ring resonators [4], AWG [5], active/passive tapered couplers [6], and Er doped lasers [7]. This dissertation then adds another layer to the platform evolution by establishing the necessary building block and demonstrating three different complex PLCs with different design constraints: an optical true time delay, dispersion compensating filter, and a single layer and multi layer spiral for use as an optical gyroscope coil.
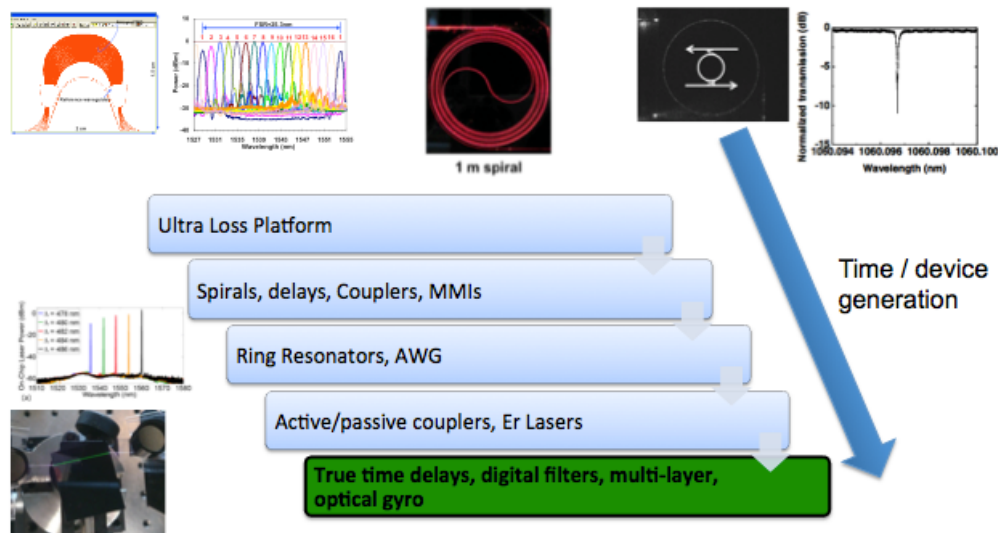

Figure 120: Evolution of ULLW platform showing the contribution of this dissertation highlighted in green.

In Chapter 1, the designs constraints for all three PLCs presented herein are introduced, while in Chapter 2 the platform is presented and the fabrication process flow explained. In the third chapter of this dissertation, each building block required to design the circuits presented here are defined. Chapters 4, 5, 6, and 7 present the fabrication and measurements of all of the devices. In Chapter 4, we present the integration of the longest integrated binary optical switched delay line for use in broadband phased array antennas, demonstrating delays longer than 12 ns in time (> 2 meters) on a single chip. Chapter 5, highlights the platform's ability to provide relatively low loss at tight bend radii by integrating a state of the art dispersion compensating filter with low loss at a record footprint able to compensate +/- 500 ps/nm at a footprint of only 222.5 mm^2. To conclude, Chapter 6 presents the integration of long delay lines (3-meter spiral) for use as optical gyroscope sensing coils, while chapter 7 shows how to integrate even longer delays with a footprint enhancement via a multi-layer platform, where a broadband vertical coupler is designed and presented with losses < 0.5 dB per transition. Finally, in this chapter we close with future direction for related work.

8.2 Future Directions

In this section the future direction for improvement on the work presented here is suggested and broken down into different sections for platform and each individual devices.

8.2.1 Platform

Chapter 2 presents the typical waveguide losses as a function of wavelength for different waveguide geometries on the ULLW platform. The loss spectrum showed large wavelength dependence with the shorter wavelength having higher propagation losses in the range

measured (1530nm to 1600 nm). The main reason for such phenomenon is the absorption due to the hydrogen impurities incorporated in films due to the precursors used during depositions. Although increasing annealing time and temperature can theoretically improve hydrogen removal, the tool's highest temperature and a process that can be achievable in a reasonable timeline set practical limits. Therefore, one way to improve the material loss is by using Deuterated precursors which will replace all the hydrogen bonds with deuterium, and since D_2 has a heavier mass than H_2, all of the absorption peaks would be shifted to outside operation regime [8]. Another possible solution is performing a dehydration using chemical reactive reagents in order to reduce the –OH group, for example, chlorine. The chlorine breaks the Si-OH absorption according to the reaction shown below, which becomes active at temperatures greater than 800 °C at which point the byproducts are driven through diffusion [9].

$$2\,H_2O + 2\,Cl_2 \;\rightarrow\; 4\,HCl + O_2$$
$$2\,Si - OH + 2\,Cl_2 \;\rightarrow\; 2\,Si - Cl + 2\,HCl + O_2$$
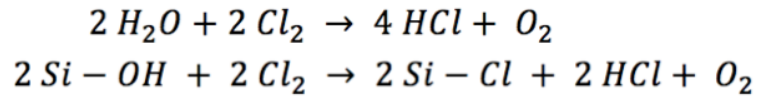
8.2.2 Optical True Time Delay

The work presented here for the OTTD used a conservative minimum bend radius of 5 mm for a 60 nm thick core and 7 μm wide. While this bend radius is well above the critical bend radius, the simulation shown in Figure 121 suggests that a 1.5 mm bend radius would still provide negligible bend loss at a drastic footprint reduction. Therefore, a more compact design can be laid out for fabrication.
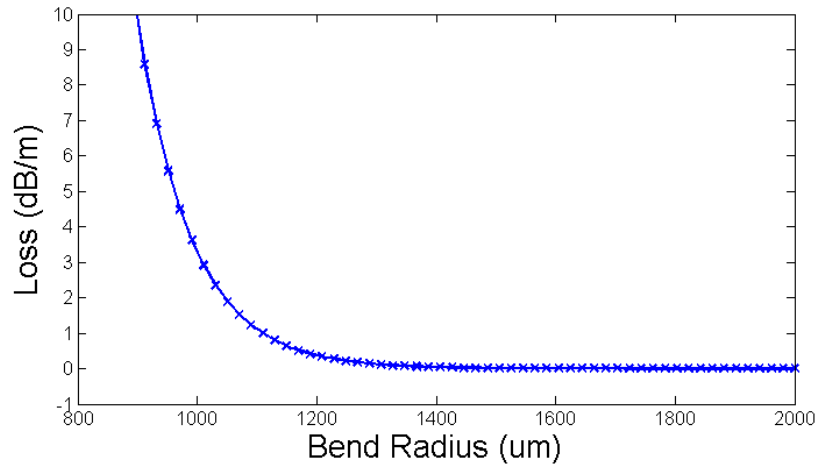
Figure 121: Simulated bend loss for waveguide core with dimensions of: 0.06 x 7 um.

A higher bit count would also allow for a finer scanning resolution, where an 8-bit delay is suggested for a next generation. Another possible direction for future implementation would be to incorporate the multi-layer work developed in chapter 7 to increase the bit count and delay range while still maintaining a conservative footprint. Figure 122 shows an illustration of an OTTD laid out as generation 1 but using the multi-layer technology [10] to double the bit-count while maintaining the same footprint.
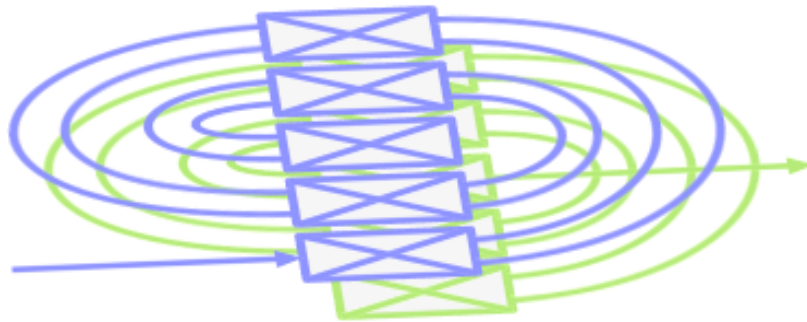

Figure 122: Illustration of a multi-layer OTTD.

The full beamforming network can then be fully integrated onto a single chip, and work shown in [6] can be used in combining the work presented here with the remainder of the

170

optical network, which would include lasers, modulators, 1xN power splitter, and a photodetector.

8.2.3 Dispersion compensating filter

In Chapter 5 we present the optical finite impulse response filter, which was able to compensate +/- 500 ps/nm of dispersion at a record footprint of 2.23 cm^2 with a minimum bend radius of 0.5 mm. Even though the overall losses were comparable to the state of the art devices, much improvement remains to minimize the insertion loss to < 3 dB. The metal absorption loss was measured to be 5 dB for the entire device; therefore, a 5 dB improvement can be accomplished simply by adding more upper cladding between the waveguide core and the phase tuners. Another major source of loss that was simulated was the offset between the bend modes and straight modes, which corresponded to approximately 10 dB as suggested in Chapter 5. As a result, the next generation can be further improved in insertion loss by adding bend offsets at each waveguide transition.

Another potential and very promising area of research would be the integration of electronic feedback to dynamically control the adjustment of dispersion, especially at high bit rates as tolerances are tighter and any small dispersion fluctuation falls outside the tolerance window. Finally, the integration of a whole differential receiver with the addition of the filter presented here is particularly promising since differential receivers do not require local oscillators, but they lack the ability to compensate CD electronics. An illustration of a possible device where the whole dispersion compensation receiver is integrated onto a single chip with the use of the multi-layer technology is shown in Figure 123.
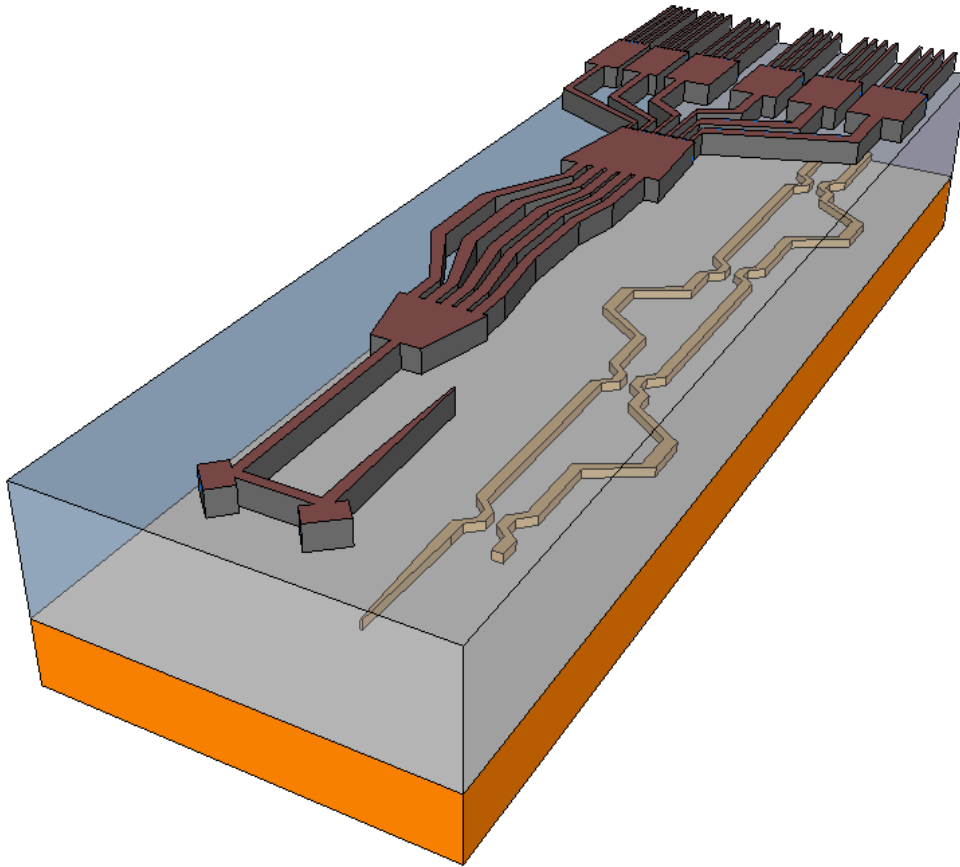
Figure 123: The schematic of a potential multilayer dispersion compensating receiver using the multi-layer technology presented in Chapter 7.

8.2.4 Optical Gyroscope

The most obvious and simple improvement for the next generation of optical gyroscope coil is the introduction of chemical mechanical polishing (CMP) between core layers so as to planarize the upper cladding before the deposition of the second core, thus allowing for low loss propagation on both layers. The next generation of gyroscope coil should also be a longer length with a new and improved waveguide crossing for low loss integration. And finally, the full integration of a low loss gyroscope coil with the gyro frontend integrated monolithically is the future direction for the development of the next generation IWOG as shown in Figure 124.
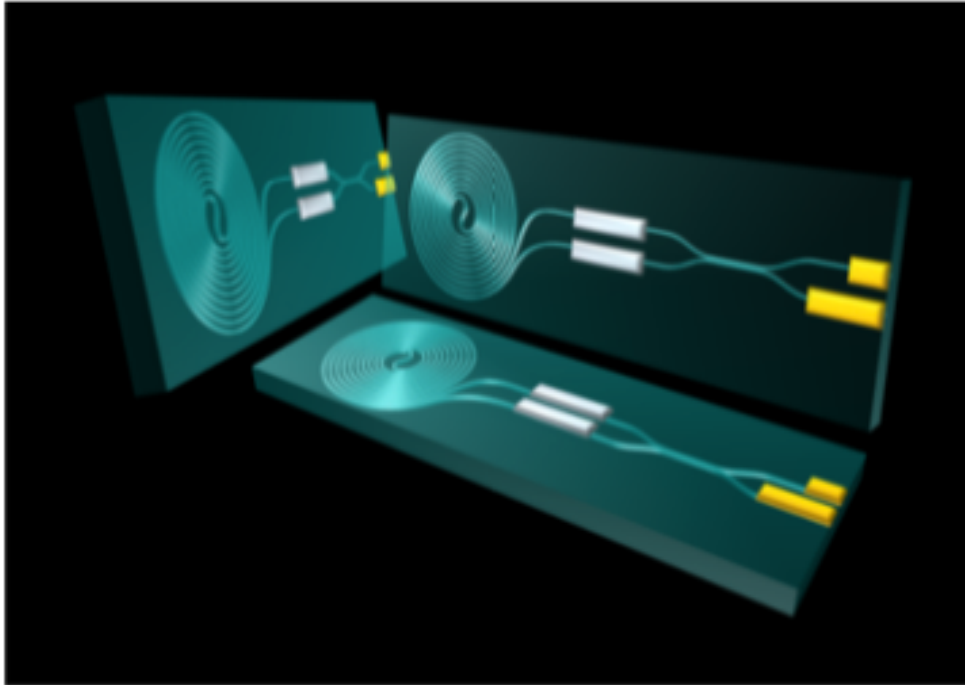
172

Figure 124: Illustrative example of a 3-axis fully integrated IWOG-PIC with active/passive integration.

8.2.5 Thermal optic switch

Lastly, decreasing the thermal crosstalk, power consumption, and increasing the switch speed could improve the thermo-optic switch building block, which is used for the integrated optical delay and the dispersion compensation filter. One of the simplest known methods for improving the next generation of TO-switches is to reduce the thermal crosstalk and power consumption by introduction of a heat insulating groove between waveguide cores [11]. Figure 125 shows the beginnings of the deep oxide etch procedure required for such technique.
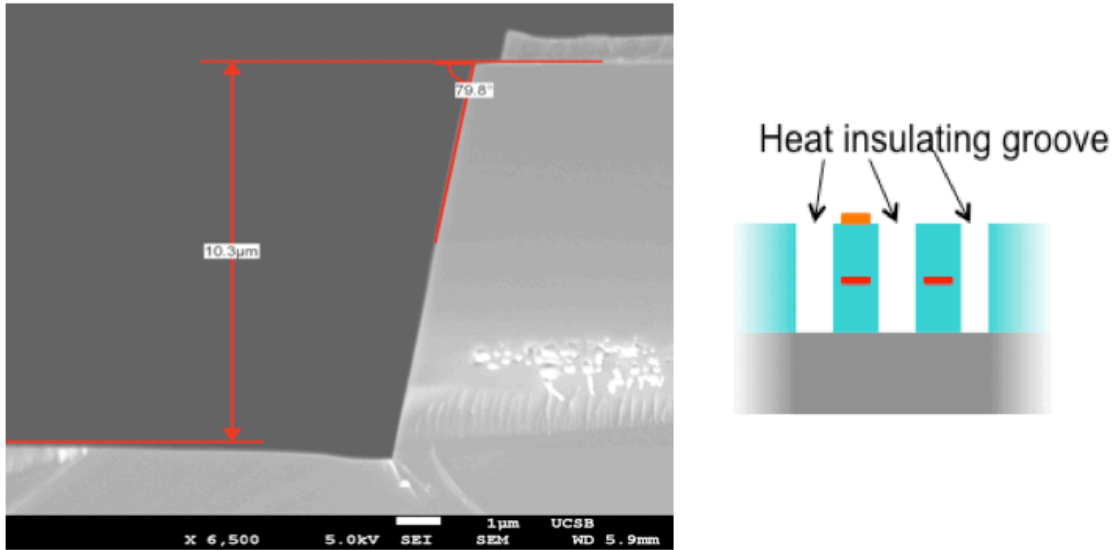
Figure 125: Etch required for creating a heat insulating groove to improve power consumption of TO-switches.

8.3 Conclusion

This dissertation presents the photonic integration of optical delay line circuits on an ultra low loss waveguide (ULLW) platform developed at UCSB. Although successful integration has been achieved, many possible directions for future improvement and research have been presented here starting with a path to lower propagation loss, to improving a single building block, as well as building upon the circuits presented here to create even more complex PLCs.

8.4 References

[1]   Jared F. Bauters, Martijn J. R. Heck, Demis John, Daoxin Dai, Ming-Chun Tien, Jonathon S. Barton, Arne Leinse, René G. Heideman, Daniel J. Blumenthal, and John E. Bowers, "Ultra-low-loss high-aspect-ratio Si3N4 waveguides," Opt. Express 19, 3163-3174 (2011)

[2]   J. Bauters, M. Heck, D. D. John, M. Tien, W. Li, J. S. Barton, D. J. Blumenthal, J. Bowers, A. Leinse, and R. G. Heideman, "Ultra-low-loss Single-mode Silicon Nitride Waveguides with 0.7 dB/m Propagation Loss," in 37th European Conference and Exposition on Optical Communications, OSA Technical Digest (CD) (Optical Society of America, 2011), paper Th.12.LeSaleve.3.

[3]   J. F. Bauters, M. Heck, D. Dai, D. D. John, J. Barton, D. Blumenthal, and J. E. Bowers, "High Extinction, Broadband, and Low Loss Planar Waveguide Polarizers," in Advanced Photonics Congress, OSA Technical Digest (online) (Optical Society of America, 2012), paper ITu2B.2.

[4]   Ming-Chun Tien, Jared F. Bauters, Martijn J. R. Heck, Daryl T. Spencer, Daniel J. Blumenthal, and John E. Bowers, "Ultra-high quality factor planar Si3N4 ring resonators on Si substrates," Opt. Express 19, 13551-13556 (2011)

[5]   Daoxin Dai, Zhi Wang, Jared F. Bauters, M.-C. Tien, Martijn J. R. Heck, Daniel J. Blumenthal, and John E Bowers, "Low-loss Si3N4 arrayed-waveguide grating (de)multiplexer using nano-core optical waveguides," Opt. Express 19, 14130-14136 (2011)

[6]   Jared F. Bauters, Michael L. Davenport, Martijn J. R. Heck, J. K. Doylend, Arnold Chen, Alexander W. Fang, and John E. Bowers, "Silicon on ultra-low-loss waveguide photonic integration platform," Opt. Express 21, 544-555 (2013)

[7]   Michael Belt and Daniel J. Blumenthal, "Erbium-doped waveguide DBR and DFB laser arrays integrated within an ultra-low-loss Si3N4 platform," Opt. Express 22, 10655-10660 (2014)

[8]   R. Yoshimura, M. Hikita, S. Tomaru and S. Imamura, "Low-loss polymeric optical waveguides fabricated with deuterated polyfluoromethacrylate," in Journal of Lightwave Technology, vol. 16, no. 6, pp. 1030-1037, Jun 1998.

[9]   Chida, K., Hanawa, F., & Nakahara, M. (1982). Fabrication of OH-free multimode fiber by vapor phase axial deposition. IEEE Journal of Quantum Electronics, 18(11), 1883–1889.

[10]   R. Moreira, J. Barton, M. Belt, T. Huffman, and D. Blumenthal, "Optical Interconnect for 3D Integration of Ultra-Low Loss Planar Lightwave Circuits," in Advanced Photonics 2013, H. Chang, V. Tolstikhin, T. Krauss, and M. Watts, eds., OSA Technical Digest (online) (Optical Society of America, 2013), paper IT2A.4.

[11]   M. P. Earnshaw, M. A. Cappuzzo, E. Chen, L. Gomez and A. Wong-Foy, "Ultra-low power thermo-optic silica-on-silicon waveguide membrane switch," in Electronics Letters, vol. 43, no. 7, pp. 393-394, March 29 2007.